Seismic Performance of Stone Masonry and Unreinforced Concrete Railroad Bridge Piers

A Dissertation Presented for the

Doctor of Philosophy

Degree

The University of Tennessee, Knoxville

Qiang Gui

December 2019

DEDICATION

I dedicate this dissertation to my wife Miankun Wang and my parents Baosheng Gui and Shufen Zhang for their love, patience and support. Without their support, this study and dissertation would not have been possible.

ACKNOWLEDGEMENTS

I express my gratitude to Dr. Zhongguo John Ma. He provides me the precious opportunity to have research training in his group. He corrected my stubborn altitude on the classic textbooks and previous research and fostered me to start to view the literature in a critical way. He gave me freedom in my research while providing sufficient support at the right times. He transfers every discussion into a teaching moment. I am blessed to be one of his students.

I thank Dr. Richard M. Bennett for his constant spiritual and technical support, cares and helpful suggestions not just on this study, but also on my life and future career development.

I thank Dr. David B. Clarke for providing funding to support me in finishing this project and for his valuable comments on this study.

I thank Dr. Xiaopeng Zhao for serving on my committee and helping to make this dissertation better from a theoretical point of view.

I thank the late Dr. Edwin G. Burdette for his mentoring and care. He helped me feel comfortable in the U.S. education system and bolstered my confidence in both coursework and research.

I am grateful to Mr. Larry Roberts, Mr. Andy Baker and Mr. Michael Allen for their support on the preparation of the shaking table test with their professional and precise works.

I thank my group colleagues for their spiritual support and technical comments during my PhD study. They are Mr. Usama Al Saffar, Mr. Nolan Hayes, Mr. Ammar Elhassan, Ms. Debalina Ghosh and Mr. Mohammed Abdelrahman.

Finally, I wish to express my appreciation to the following organizations that provided the financial support to make this research possible. They are the National University Rail (NURail) Center, the Center for Transportation Research, and the Department of Civil and Environmental Engineering at the University of Tennessee-Knoxville.

ABSTRACT

Railroads in the United States have numerous bridges that are at least 100 years old. With upgrading aged bridges, there is a push to reuse existing substructures while replacing entire superstructures. Often these substructures are unreinforced masonry (URM) or unreinforced concrete (URC). In order for the URM or URC elements to be incorporated into modernized bridges, they must be evaluated for their ability to withstand seismic loading.

The U.S. railroad design code hypothesizes that the restraining effect of rail track reduces bridge damage during earthquakes. A structural modeling scheme for the ballast deck bridge and the open-deck girder bridge are proposed in SAP2000 using nonlinear link element to simulate the behavior of bearings and ballast structure under the lateral push. The experimental data from previous studies are used to calibrate and verify the proposed modelling scheme. The equivalent spring stiffness of the rail track system obtained by the modelling analysis is intended to be used in the subsequent small-scale shaking table experimental study which investigates the dynamic response of column shape rigid body specimens with spring restraint on top. Several parameters are considered in the test matrix such as stiffness of restraint spring, height/breadth ratio, ground excitations and single-body or multi-body configuration. The testing data prove the restraining effect of rail track applied on the top of the bridge piers.

Coefficient of restitution is an important index to evaluate the kinetic energy loss during the impact for a rocking block. The models and expressions proposed by Housner and other researchers are reviewed comprehensively. A hypothetical model that includes three coordinates and consider the possible bouncing up scenario of the rigid block is proposed. A unified expression is developed in study.

Keywords: Stone masonry, unreinforced concrete, rail track, restraining effect, shaking table, rigid body, rocking, sliding, coefficient of restitution, kinetic energy loss.

TABLE OF CONTENTS

Chapter 1: Introduction 1

1.1 Motivation 1

1.2 Goals and Methodology 1

1.3 Structure of the Dissertation 2

Chapter 2: Seismic Performance of Unreinforced Masonry (URM) and Unreinforced Concrete (URC) Railroad Bridge Piers: State-of-the-Art 3

2.1 Introduction 3

2.2 Previous Seismic Research on Railroad Bridges 4

2.3 Seismic Performance of URM and URC Railroad Bridges Piers in Past Earthquakes 9

2.4 Seismic Design 16

2.4.1 AREMA MRE 2018 17

2.4.2 AASHTO LRFD Bridge Design Specifications 2017 18

2.4.3 AREMA MRE 1907 22

2.4.4 Code for Seismic Design of Railway Engineering (GB50111-2006 (2009 Edition)) in China 23

2.5 Seismic Assessment 26

2.6 Seismic Retrofit 29

2.7 Conclusions and Recommendations 33

Chapter 3: Restraining Effect of Rail Track Structure on the Performance of Railroad Bridge under Lateral Load 35

3.1 Introduction 35

3.2 Modelling Based on Previous Experimental Studies 37

3.2.1 Modelling for Uppal et al. (2000) testing 37

3.2.2 Modelling for Maragakis et al. (2001) testing 42

3.3 Results and model verification 45

3.3.1 Natural frequencies and modal analysis 45

3.3.2 Load-displacement curve 46

3.4 Discussion 50

3.4.1 Influence of Lateral Stiffness of Substructure 51

3.4.2 Influence of Rotational Stiffness of Substructure 59
3.5 Conclusions 65
Chapter 4: Shaking Table Experiment Results and Discussion 67
4.1 Introduction 67
4.2 Testing Program 67
4.3 Testing Result and Discussion 74
4.3.1 Coefficient of Friction 74
4.3.2 Failure mode under Sinusoidal Input 74
4.3.3 Restraining effect 76
4.4 Conclusions 76
Chapter 5: Unified Expression for Coefficient of Restitution in Rocking Problem 78
5.1 Introduction 78
5.2 Improved CoR Expressions in Previous Research 80
5.2.1 Kalliontzis et al. (2017) 80
5.2.2 Chatzis et al. (2017) 81
5.2.3 Ther and Kollár (2017) 81
5.2.4 Lipscombe and Pellegrino (1993) 82
5.3 Unified CoR Expression 83
5.4 Discussion on the Unified CoR Expression 85
5.4.1 Special cases of the Unified CoR Expression 85
5.4.2 Parametric study on the e_X, e_Y and α 88
5.5 Application Example 89
5.6 Conclusions 92
Chapter 6: Contributions of this Study 95
References 97
Appendix 104
Summary of Recorded Damages of URM and URC Railroad Bridge Piers in Past Earthquakes 105
Vita 121

LIST OF TABLES

Table 2.1 Summary of the Dynamic Experimental Results by UNR (Sandirasegaram 1997) 7

Table 2.2 Minimum Analysis Requirements for Seismic Effects (AASHTO 2017)..... 19

Table 2.3 Response Modification Factors for Substructures (AASHTO 2017) 21

Table 2.4 Response Modification Factors for Connections (AASHTO 2017) 21

Table 2.5 Seismic Design Checking Requirements (NRA China 2009) 25

Table 3.1 Frequencies and Mode Types of First Three Vibration Modals 46

Table 3.2 Influence of Substructure Lateral Stiffness on System Secant Stiffness for Open-deck Bridge Models 53

Table 3.3 Influence of Substructure Lateral Stiffness on System Secant Stiffness for Ballast Bridge Models..... 57

Table 3.4 Influence of Substructure Rotational Stiffness on System Secant Stiffness for Open-deck Bridge Models 61

Table 3.5 Influence of Substructure Rotational Stiffness on System Secant Stiffness for Ballast Bridge Models..... 64

Table 4.1 Instrumentation List 69

Table 4.2 Geometries of Blocks..... 71

Table 4.3 Test Matrix..... 72

Table 4.4 Failure Mode Results of Single-body Specimens without Restraint under Sinusoidal Waves..... 75

Table 5.1 Governing Equation and Space-state Equations in a Rocking Cycle 93

LIST OF FIGURES

Figure 2.1 Rail Track Mileage and Number of Class I Rail Carriers, United States, 1830-2012 (Rodrigue 2015) 3

Figure 2.2 Damaged Railroad Bridge and the Crack at the Pier (Abé and Shimamura 2014) 6

Figure 2.3 Locations of damaged URM and URC railroad bridge piers in fault line map 11

Figure 2.4 Displacement of Piers of the Pajaro River Bridge after 1906 San Francisco Earthquake (Duryea and ASCE 1907) 13

Figure 2.5 Cracking Damage at the Base of a URC Pier of Pajaro Bridge after 1906 San Francisco Earthquake (Duryea and ASCE 1907) 13

Figure 2.6 Cracking Damage of a URM Pier of Dos Pueblos Viaduct after 1925 Santa Barbara Earthquake (Kirkbride 1927) 14

Figure 2.7 Sliding at a URC Pier of Kuzuryu River Bridge after 1948 Fukui Earthquake (Far East Command 1949) 14

Figure 2.8 Tilting of Upper Partition of URC Piers of Dou River Railway Bridge after 1976 Tangshan Earthquake (Chen 1978) 15

Figure 2.9 Damage at the Coping stone of a URC Pier of Pajaro Bridge after 1906 San Francisco Earthquake (Duryea and ASCE 1907) 15

Figure 2.10 Anchorage Failure at the Bearing of a URC Pier of Bridge 14.5 after 1964 Alaska Earthquake (McCulloch and Bonilla 1970) 16

Figure 2.11 Typical Cross-section Layout of Steel Jacketing Retrofit (Priestley et al. 1996) 30

Figure 2.12 Typical Layout of Concrete Jacketing Retrofit (Priestley et al. 1996) 31

Figure 2.13 Construction of the RC Jacket Retrofitting at a URM Pier of the Illinois Central Railroad Cairo Bridge over the Ohio River (Modjeski and Masters 1953) 32

Figure 2.14 External Prestressing Retrofit at a URC Railroad Bridge Pier in New Zealand (Walsh 2002) 33

Figure 3.1 Plan View of Lateral Push Tests on Cincinnati Bridge (Uppal et al. 2000) 38

Figure 3.2 Correlation between SAP2000 Model and Physical Bridge (Pier 16 of Cincinnati bridge) 38

Figure 3.3 Constitutive Law of Rail Steel in Modeling 39

Figure 3.4 Stiffness of Ballast under Lateral Load in Modelling (after Kerr, 1980) 41

Figure 3.5 Stiffness of Bearing under Lateral Load in Testing and in Modelling for Cincinnati Bridge 42

Figure 3.6 Typical Pier Condition in Cincinnati Bridge (Uppal et al. 2000) 43

Figure 3.7 Plan-view Layout of Lateral Push Tests of California Bridge (Maragakis et al. 2001) 44

Figure 3.8 Stiffness of Bearing under Lateral Load in Testing and in Modelling for California Bridge 44

Figure 3.9**.** Constitutive Law of Plain Concrete in Modeling 45

Figure 3.10 Load vs. Displacement of Modelling Results (Cincinnati Bridge) 47

Figure 3.11 Comparison of Experimental and Modelling Results (Span 16 @abutment, Cincinnati Bridge) 48

Figure 3.12 Comparison of Experimental and Modelling Results (Span 17 @pier 16, Cincinnati Bridge) 49

Figure 3.13 Load vs. Displacement of Modelling Results (California Bridge) 50

Figure 3.14 Comparison of Experimental and Modelling Results (East span, California Bridge) 51

Figure 3.15 Influence of Lateral Stiffness of Substructure on Load vs. Displacement (open-deck bridge) 52

Figure 3.16 Influence of Lateral Stiffness of Substructure on Tensile Stress in Rail (open-deck bridge) 52

Figure 3.17 Relationship between Substructure Lateral Stiffness and Secant Stiffness for Open-deck Bridge System 53

Figure 3.18 Influence of Lateral Stiffness of Substructure on Displacement at Different Position (Open-deck Bridge) 55

Figure 3.19 Influence of Lateral Stiffness of Substructure on Load vs. Displacement (ballast bridge) 56

Figure 3.20 Influence of Lateral Stiffness of Substructure on Tensile Stress in Rail (ballast bridge) 56

Figure 3.21 Relationship between Substructure Lateral Stiffness and Secant Stiffness for Ballast Bridge System 57

Figure 3.22 Influence of Lateral Stiffness of Substructure on Displacement at Different Position (Ballast Bridge) 58

Figure 3.23 Torsion with Respect to Pier Centerline Axis 59

Figure 3.24 Influence of Torsional Stiffness of Substructure on Load vs. Displacement (open-deck bridge) 60

Figure 3.25 Influence of Torsional Stiffness of Substructure on Tensile Stress in Rail (open-deck bridge) 60

Figure 3.26 Relationship between Substructure Rotational Stiffness and Secant Stiffness for Open-deck Bridge System 61

Figure 3.27 Influence of Rotational Stiffness of Substructure on Displacement at Different Position (Open-deck Bridge) 62

Figure 3.28 Influence of Torsional Stiffness of Substructure on Load vs. Displacement (ballast bridge) 63

Figure 3.29 Influence of Torsional Stiffness of Substructure on Tensile Stress in Rail (ballast bridge) 63

Figure 3.30 Relationship between Substructure Rotational Stiffness and Secant Stiffness for Ballast Bridge System 64

Figure 3.31 Influence of Rotational Stiffness of Substructure on Displacement at Different Position (Ballast Bridge) 65

Figure 4.1 a) Single-body and b) Dual-body Prismatic Block Systems 68

Figure 4.2 Example application of Tracker 5.0.5 in this study 69

Figure 4.3 Frame for Spring Restraint Attachment and Testing Setup 70

Figure 4.4 a) Ground Acceleration Time History and b) FFT Power Spectrum of NORTHR_MUL009 Record 72

Figure 4.5 a) Ground Acceleration Time History and b) FFT Power Spectrum of IMPVALL_E06140 Record 73

Figure 4.6 a) Ground Acceleration Time History and b) FFT Power Spectrum of GAZLI_GAZ000 Record 73

Figure 4.7 Coefficient of Friction Measurement Setup 74

Figure 4.8 Force-displacement Data for Coefficient of Friction Measurement 75

Figure 4.9 Response Time-history Comparison for X-direction Tip Displacement of Dual-body System w/ and w/o Horizontal Restraint under Earthquake NORTHR_MUL009, 1 in.=25.4 mm 77

Figure 5.1 Diagram of Housner (1963) Model 79

Figure 5.2 Comparison of r estimation by Housner (1963) with reported experimental data (after Kalliontzis et al. 2017) 79

Figure 5.3 Diagram of Kalliontzis et al. (2017) Model 80

Figure 5.4 Diagram of Chatzis et al. (2017) Model 82
Figure 5.5 Diagram of Ther and Kollár (2017) Model 82
Figure 5.6 Diagram of Lipscombe and Pellegrino (1993) Model.................................... 83
Figure 5.7 Diagram of Proposed Model in this Study 84
Figure 5.8 Diagram of e_X , e_Y and e_θ 86
Figure 5.9 Graphic Relationship of $\dot{x}_C{}^+$, $\dot{y}_C{}^+$ when $e_\theta = e_X = e_Y$ 86
Figure 5.10 Graphic Relationship of $\dot{x}_C{}^+$, $\dot{y}_C{}^+$ when $e_\theta = e_X < e_Y$ 87
Figure 5.11 Graphic Relationship of $\dot{x}_C{}^+$, $\dot{y}_C{}^+$ when $e_\theta = e_X > e_Y$ 88
Figure 5.12 Location of Vertical Impulse Resultant.. 89
Figure 5.13 Parametric Study on e_X and e_Y 90
Figure 5.14 Parametric Study on h / b and e_Y 90
Figure 5.15 Geometric Information of Specimen #2 91
Figure 5.16 Comparison between Results of Different CoR Expressions and Experimental Data 94

Chapter 1: Introduction

1.1 Motivation

The railroad infrastructure in the United States includes many bridges that are 100 years old or older (U.S. Govt. Accountability Office 2007). A common approach to bridge replacement is to reuse the existing substructure while replacing the superstructure. Often, the substructure is unreinforced masonry (URM) or unreinforced concrete (URC) piers. In order to use the URM and URC piers in an extended design life, they must be evaluated for their ability to withstand seismic loading.

1.2 Goals and Methodology

The objective of this project is to investigate the behavior and failure modes of URM and URC piers subject to earthquake loads and propose mitigation or retrofit methods for these structural elements.

A literature review was conducted to investigate the behavior and damage patterns of URM and URC railroad bridge piers in past earthquakes. It was found that railroad bridges generally performed well in past earthquakes. The track system, which restrain the horizontal movement of the pier top, is considered to contribute to the good performance. The theoretical analysis on this restraining effect has not been addressed in previous studies where only full-scale testing was conducted.

To quantify an equivalent spring stiffness of the restraining effect, a structure modelling scheme is proposed in SAP2000. It uses nonlinear link elements to simulate the behavior of the bearings and the ballast track structure under lateral forces. Experimental data from previous studies is used to calibrate and verify the proposed modelling scheme. This model is employed to investigate the influence of lateral stiffness and rotational stiffness of the substructure on the performance of the bridge structure under lateral pushover load with rail track intact.

Based on observation of URC/URM railroad bridge piers in previous earthquakes, the piers slide and rock, which are typical rigid body motions. Therefore, this study proposes to simplify the railroad piers into single-body or stacked dual-body rigid block systems with horizontal restraints at the top. It then examines the behavior of these systems when subjected to various ground motions. A series of rigid-body dynamic tests were conducted, and the restraining effect was verified by the testing data.

Finally, the study investigated an important index that evaluates the kinetic energy loss during impact for a rocking rigid body. A unified rotational coefficient of restitution was developed after reviewing previous related research.

1.3 Structure of the Dissertation

Chapter 2 presents the literature review of previous studies on seismic performance of railroad bridges; seismic performance of existing URM and URC railroad bridge piers; failure modes of URM and URC piers (tabulated in Appendix A); and seismic design, assessment, and retrofit requirements in the major codes around the world.

Chapter 3 develops the numerical investigation of the equivalent spring stiffness of the restraining effect of the rail track system. A structural analysis model of the rail track structure under lateral pushing load treats the rail as a continuous beam with spring support at each anchor position between the rail and ties. The connection between the ties and the bridge superstructure is modelled as a rigid link for open deck railroad bridges and as a spring link for ballasted deck railroad bridges. The proposed model is verified with the data from previous full-scale field testing. A parametric study is conducted for a range of the stiffness of the rail track structure under lateral loading.

Chapter 4 describes the experimental investigation of the dynamic response of column shaped rigid body specimens with a spring restraint on the top. Several parameters are considered in the test matrix: stiffness of restraint spring, height/breadth ratio, ground excitations and single-body or multi-body configurations. The testing results are discussed.

Chapter 5 develops the unified rotational coefficient of restitution. The models and hypotheses in all related previous research are summarized. The unified expression includes three coordinates (i.e., the horizontal and vertical displacements and angular displacement).

Finally, Chapter 6 summarizes the contributions of this study.

Chapter 2:

Seismic Performance of Unreinforced Masonry (URM) and Unreinforced Concrete (URC) Railroad Bridge Piers: State-of-the-Art

2.1 Introduction

In 1830, the first U.S. railroad for commercial transport of passengers and freight, built by the Baltimore & Ohio Railroad, opened (America's Library 2015). After 185 years, the railroad network in the U.S. has reached approximately 140,000 miles (Rodrigue 2015). It plays an important role in the development of the United States, and it dominated the transportation market before the construction of modern highways.

Railroad mileage peaked in 1916 with 254,000 route-miles (Rodrigue 2015), as shown in **Figure 2.1**. From the 1920s, the industry entered a long period of decline. The vast majority of railroad bridges surviving today were constructed between 1890 and 1930 (Solomon 2008). According to a 1993 bridge survey by Federal Railroad Administration (FRA), more than half of the U.S. railroad bridges were built before 1920 (U.S. Govt. Accountability Office 2007).

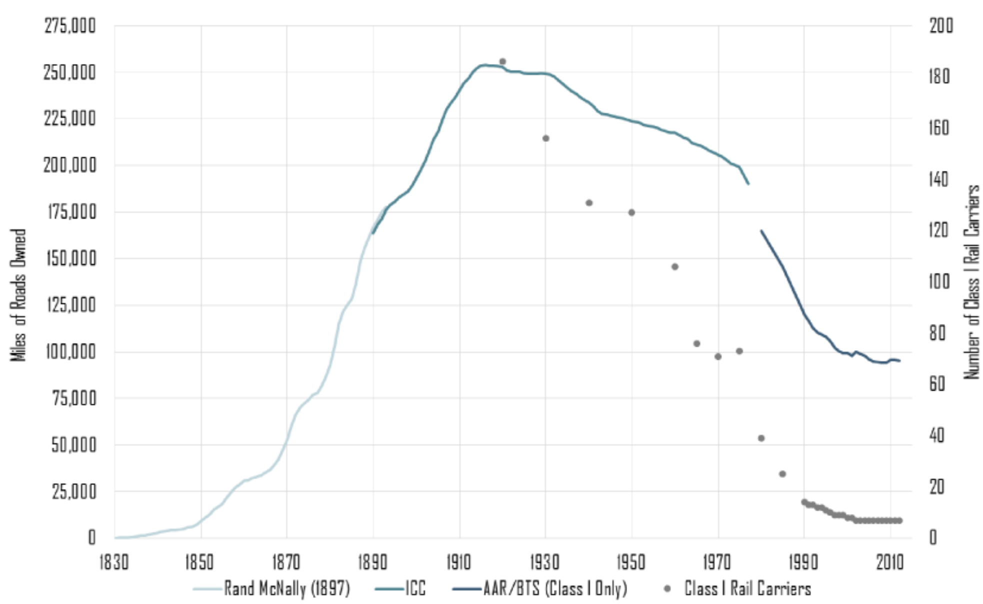

Figure 2.1 Rail Track Mileage and Number of Class I Rail Carriers, United States, 1830-2012 (Rodrigue 2015)

In 1887, the Pennsylvania Railroad began to replace wooden bridges with masonry structures on its east-west Main Line. After that, masonry viaducts dominated the structural type of railroad bridges in North America until the emergence of concrete structures in the first decade of the twentieth century (Tyrrell 1911). The advantages of masonry bridges include: (1) solidly built, requiring minimal maintenance under normal conditions; (2) ability to withstand the continued increase of axle weights and train speeds; (3) less likely to suffer from washouts (Solomon 2008). This may explain why, as an old building material, masonry structures represent 20% of the 76,000 railroad bridges in the U.S. (U.S. Govt. Accountability Office 2007).

Because of the important role of the railroad network, a critical impact would occur if the railroad system experiences damage or disruption from an earthquake. Based on research into railroad bridges in the Mid-American region (Day and Barkan 2003), Day and Barkan point out that the total length of all bridges in the areas potentially exposed to damaging Peak Ground Acceleration levels (2% probability of experiencing greater than 0.2 g in the next 50 years) is about 306,800 ft. (58 mi.). Eight bridges across the Ohio and Mississippi Rivers carry about 245 million revenue tons of freight per year, accounting for 11.4% of the national total rail freight originating in the United States. Thus, sufficient seismic research on railroad bridges should be conducted to protect railroad bridges and networks properly in order to prevent the potentially devastating impact caused by bridges failure after earthquakes on national operation.

2.2 Previous Seismic Research on Railroad Bridges

Several efforts related to seismic research have been undertaken in the past 25 years by the U.S. railroad community. In 1993, the American Railway Engineering and Maintenance-of-Way Association (AREMA) established a stand-alone committee (AREMA Committee 9) to develop seismic design guidelines specific to railway structures. In 1997, the U.S. Department of Transportation and the Japanese Ministry of Transport signed an agreement to improve the general understanding of the behavior of railway structures in earthquakes and reduce the potential for casualties, damage, and disruption of traffic (Prucz and Otter 2002).

Many of these efforts focus on the seismic performance of railroad systems in past earthquakes. Byers investigated railroad damage in 20 notable earthquakes with magnitudes greater than 6 (Byers 1996). He demonstrated that the most frequent reason for damage was soil movement due to liquefaction or lateral spreading at stream banks, and shaking. Since 1940, Byers (1996) says the seismic performance of railroad bridges is superior to highway bridges.

Prucz and Otter (2002) constructed a database containing information about 3,500 railway structures located in areas affected by earthquakes. The bridge data include information on each bridge's structural characteristics (i.e., type, length, height, number of spans, and span length) as well as information on seismic performance. This study includes a general description of the performance of railway structures during the 1886 Charleston Earthquake, the 1906 San Francisco Earthquake, and the 1964 Alaska Earthquake which caused extensive damage. It found that damage to railroad bridges has been relatively limited. Several factors that contribute to this good seismic response to ground shaking include: (1) proper selection of structure type and configuration, as well as sound design; (2) characteristics such as simplicity, symmetry, and regularity; and (3) proper consideration of details such as the bearing seat. Current railroad bridge design and construction practices typically follow these requirements.

Byers summarized seismic damages to railroads around the world in 93 earthquakes from 1886 through 2003 (Byers 2003). He collected more than 580 photographs that illustrate damage to railroad systems after earthquakes. Data related to railroad damage and earthquake characteristics as well as the sources of the data were listed in a spreadsheet. The type and severity of damage are also included in this spreadsheet. Researchers can use this database to further analyze and improve understanding of railroad structure response to seismic activity.

Based on his 2003 database, Byers (2004) analyzed the characteristics of damaging earthquakes, railroad damage mechanisms and effects on operations and recovery by introducing examples from various earthquakes. Damage that affected railroad operations after earthquakes included derailments and damage to bridges, tunnels, tracks and roadbed, railroad buildings and signals, and communication facilities. He concluded that: (1) railroads are apt to suffer from severe impact when they span active faults; (2) generally speaking, a comprehensive recovery plan might be a more economical solution to reduce impact of earthquakes than retrofitting.

In 2001, three significant earthquakes occurred around the world: the magnitude (M) 7.7 Gujarat Earthquake, the M6.8 Nisqually Earthquake, and the M8.4 Atico Earthquake. Byers examined the damage to railroad infrastructure, track, roadbed, bridges, tunnels, and buildings during these strong shocks (Byers 2004). He reported that: (1) track and roadbed damage resulted from settlement, slides, and rock falls; (2) damage to railroad bridges included minor displacement of steel girder spans, cracking of joints in masonry piers and arches, separation of wing walls from abutments, collapse of masonry spandrel walls of arches, rotation and displacement of a framed dump bent in a timber trestle, and movement of piers of an open bascule span that prevented closing of the span; (3) damage to tunnels was minor. Byers pointed out that, with appropriate operating restrictions, cracking along mortar joints within masonry piers and large displacement between abutment and roadbed might not significantly impact the safe operation of trains after earthquakes.

Abé and Shimamura reported on the performance of railway bridges along the Shinkansen line during the 2011 Tohoku Earthquake and several aftershocks (Abé and Shimamura 2014). Bridge structures of the Shinkansen line were retrofitted and upgraded to the updated seismic design code after severe structural damage was observed in the 1995 Kobe Earthquake. With this strategy, bridge damage was reduced considerably and the time for recovery of service operation was decreased correspondingly. No major damage is reported for structures that had been given the post-1995 earthquake seismic retrofit. A severe crack along the bed joint was observed at a brick masonry pier (shown in **Figure 2.2**). Excessive deformations of rail tracks were also observed at this bridge. A structural monitoring and an alarm system detected this behavior during the shock and provided warning.

Several studies have focused on seismic experimental and theoretical research into railroad bridges. Sharma et al. examined the design criteria used for railway bridges during the past century and analyzed their beneficial effects on the seismic performance for railway bridges (Sharma et al. 1994). The values of longitudinal force for open deck spans with various spans by chronological railroad design code were normalized to equivalent acceleration (g). Sharma et al. concluded that the design equivalent acceleration values for longitudinal forces based on railway design criteria were generally higher than 0.4g, the maximum value of Effective Peak Acceleration (EPA) in the western regions of the continent. The contribution to longitudinal resistance from the rail track structure was discussed preliminary that the track provides an additional restraint and a mechanism for transferring seismic loads to roadbed, and helps the substructure to be relieved from carrying all of the seismic load demand.

Railroad bridges have better seismic performance in past earthquakes than highway

Figure 2.2 Damaged Railroad Bridge and the Crack at the Pier (Abé and Shimamura 2014)

bridges (Byers 1996, Cook et al. 2006). The track system contributed to this improved performance because it acts as a restraint against horizontal movement of the superstructure during earthquakes (AREMA 2018). To verify this assumption, a series of field tests were conducted from 1994 to 2000 in the U.S.

(1) From 1994 to 1995, two full-scale field tests on a railroad ballast deck through-plate girder (TPG) bridge were conducted by the Association of American Railroads (AAR), the California Department of Transportation (Caltrans), and the University of Nevada Reno (UNR). One of the tests was designed to quantify the beneficial effects of the dynamic response of the bridge of the connection that the rails provide between the structure and the adjacent roadbed (Maragakis et al. 1996; Sandirasegaram 1997). The bridge was excited in both the transverse and longitudinal directions by a dynamic shaker, with rails intact and rails cut at the abutments, respectively. Natural frequencies and the corresponding mode shapes and modal damping values were identified based on the analysis of the field data from the resonance tests (as shown in **Table 2.1**).

    The authors concluded that: (a) in all cases, cutting the rails resulted in lower natural frequencies, which indicates a softer system; (b) no significant effects on the modal damping values were observed, with the exception of the modal damping of the fundamental transverse frequency; and (c) in the longitudinal direction, disconnecting the rails resulted in a sudden decrease of the vibrations that were transmitted to the roadbed. The authors mentioned that the effect of cutting the rails may be more significant for open deck bridges than for ballast bridges.

    The other test was designed to identify the ultimate capacity of the deck-abutment connections in the lateral direction (Maragakis et al. 2001). The track structure (i.e., the rails, ties and ballast, and the ballast pan) were cut completely free at the west abutment and the part of the deck above the central pier. The east abutment was left in its as-built condition with the ties, rails, ballast, and ballast pan intact.

Table 2.1 Summary of the Dynamic Experimental Results by UNR (Sandirasegaram 1997)

Mode	Rail Uncut		Rail Cut	
	Frequency	Damping	Frequency	Damping
First Transverse Mode	4.93	2.15	4.80	2.3
Second Transverse Mode	6.75	4.50	-	-
First Longitudinal Mode	6.56	5.00	5.95	5.33
First Vertical Mode	6.06	1.65	5.55	1.45

Lateral force was applied to the bridge directly over the bearings at the abutments. Force-displacement diagrams were obtained at both ends of the bridge. We may conclude that for this bridge: (a) the ultimate capacity at the as-built end was 45% greater than that at the free end, which could be explained by the presence of the ballast pan (tie-plate), ballast, ties, and rails; (b) the ultimate strength of the steel bearings is controlled by the tensile strength of the anchor bolts plus the friction force on the sliding surface; and (c) due to the additional strength that the railway elements provide, the seismic retrofitting requirements of this type of railway bridge could be less than those of highway bridges.

(2) In 1998, the Transportation Technology Center, Inc. (TTCI) deployed a field test on a 5-span 62-ft, open-deck deck plate girder (DPG) steel bridge subjected to lateral and longitudinal loading (Otter et al. 1999a; Uppal et al. 2000). The objectives were: (a) to quantify the total resistance of these spans; and the contribution of the rail to this total resistance; and (b) to investigate the contribution of anchor bolts, friction and continuity of the track structure to the bridge's resistance.

The authors concluded that: (a) the lateral resistance of this type of railroad bridge exceeds some of the most severe requirements used in seismic design of bridges; (b) the resistance to lateral displacement was provided primarily by anchor bolts, frictional and locking forces, and the continuous rail; and (c) the resistance of the approach abutment could be reduced by vertical uplift or liquefaction.

(3) In 2000, TTCI conducted a field test on two open deck I-beam railroad spans to examine the resistance to longitudinal movement provided by the track structure (Doe et al. 2001; Uppal et al. 2001). The intermediate span was tested to quantify the resistance between rail and bridge deck and the resistance between bridge deck and span. In addition, this test measured the resistance to longitudinal movement offered by friction between plates, hook-bolts, and box anchoring of bridge ties. Displacement measurements were taken at the interfaces of the rail to tie, tie to beam, and beam to pier. The conclusion is that for this bridge: (a) the coefficient of friction for resistance against longitudinal movement with the flat bearings greased and rails disconnected was 0.21; (b) the coefficient of friction between rail and bridge deck was 0.24 when the ties were box-anchored for this test and everything else was loose; (c) the coefficient of friction between bridge deck and span was 0.37 when rails were anchored but hook bolts were loose; (d) the coefficient of friction for the whole deck span system was 0.49 when ties and hook bolts were tightened. They concluded that properly anchored rail and bridge decks can provide significant resistance to ground motion, which may be enough to eliminate the need for seismic retrofit of many railroad bridges.

The Mid-America Earthquake (MAE) center conducted a study on seismic evaluation of a railroad bridge spanning the Mississippi River in Memphis, Tennessee (Foutch and Yun 2001). This bridge was built in 1894 on deep, soft soil within the New Madrid seismic zone. Six stone masonry piers with caisson foundation support a five span steel truss superstructure. A three-dimensional model of this bridge was built using SAP 2000 software. Using this model, mode analysis and elastic response analysis were carried out. The results showed that the first order period of transverse mode was 3.05 seconds; the first order period of vertical mode was 1.16 seconds; and the first order period of longitudinal mode was 1.19 seconds. The elastic analysis showed that under M7.5 earthquake excitation in tri-axial ground motions the most vulnerable components of the bridge are the bearings and the stone piers instead of superstructure members. The authors also investigated the possible failure mechanisms of the piers. They include: stone layers sliding along a horizontal plane, overturning of the upper portion of the piers, and overturning at the base with toe crushing. Based on the results of modeling for longitudinal and transverse directions by Drain 2DX software, a set of hazard curves were developed. The researchers found that for these stone piers, longitudinal response is governed by tilting under a shock with a return period of 473 years, and transverse direction is governed by sliding under a shock with a return period of 1575 years. Further experiments are needed to verify the analytical results above.

2.3 Seismic Performance of URM and URC Railroad Bridges Piers in Past Earthquakes

The historical performance of URM and URC railroad bridge piers in past earthquakes can provide a better understanding of the seismic behavior of these bridge elements. The published literature that recorded historical earthquakes and their destructive effect on railroad structures was reviewed.

In this part of the study, I: (1) synthesize and compile all the resources; (2) extract and summarize the seismic performance of URM and URC piers in past earthquakes; and (3) analyze the typical failure modes for these piers under seismic excitation.

Typically, the U.S. Geographic Survey or American Society of Civil Engineers (ASCE) recorded the condition of railroad structures following earthquakes in their investigation reports. For example, the effects of the 1906 San Francisco Earthquake on engineering infrastructure were investigated and reported by experts from ASCE in 1907 (Duryea and ASCE 1907). Although six railroad companies were operating within the area of destruction, the damage to railroad structures was much less than that for buildings and highway infrastructure. The typical damage to railroad structures was from the large displacement caused by the movement of active faults. For example, the railroad bridge across the Pajaro River that spanned an active fault line was affected severely by movement along the fault. The shocks moved all four URC piers and two abutments and increased the distance between the east and west abutments by 3.5 ft.

Other damages to the piers of this railroad bridge that were caused by inertial force and displacement are discussed in the following section. In this study, we review reports from U.S. Geological Survey, including the special report on the effects of 1964 Alaska Earthquake on the railroad system (McCulloch and Bonilla 1970).

Another resource for this part of study comes from the published papers by seismic experts investigating after major earthquakes. For example, the destructive effects of the 2011 Tohoku Earthquake on the railroad infrastructure was reported in the journal paper by Abé and Shimamura (Abé and Shimamura 2014). The damage to railroad structures in the Gujarat Earthquake, the Nisqually Earthquake and the Atico Earthquake were described by Byers (Byers 2004).

Based on the database in this study, 139 of 4351 performance records report as damaged: 23 with light damage; 29 with modest damage; and 87 with severe damage. Light damage means the damage did not affect traffic after earthquakes. Moderate damage means the structures had their integrity but damage affected traffic. Severe damage means the structures lost their integrity or collapsed. These data show that, historically, railroad bridges performed well in earthquakes. However, when damage occurred, it was likely to be severe.

Five URM pier damage records and nine URC pier damage records were in the databased. Appendix A summarizes damages to URM and URC railroad bridges from past earthquakes, according to data from the literature. **Figure 2.3** shows the locations of all five URM pier damage records and nine URC pier damage records. These locations of damage records were overlapped with the major fault lines (www.usgs.gov). This illustrates the correlation between the damage and bridge distance from the fault line. The records show that most damage occurred in bridges very close to the major fault lines. There are three exceptions: two piers damaged in the Tangshan, China 1976 earthquake were close to a minor fault line in northeast China. One pier in the Charleston, Missouri 1895 earthquake was close to the New Madrid minor fault line. The definition on destructive margin, collision margin, constructive margin and conservative margin, which are not introduced in this dissertation, can be found via link https://maxwatsongeography.wordpress.com/section-a/hazardous-environments/fault-linesplate-boundaries/.

Typical failure modes of URM and URC railroad piers can be generalized as follows:

(1) Integral displacement: horizontal, vertical or tilt - This is a typical failure mode for the bridge spanning an active fault in an earthquake. An example of this mode

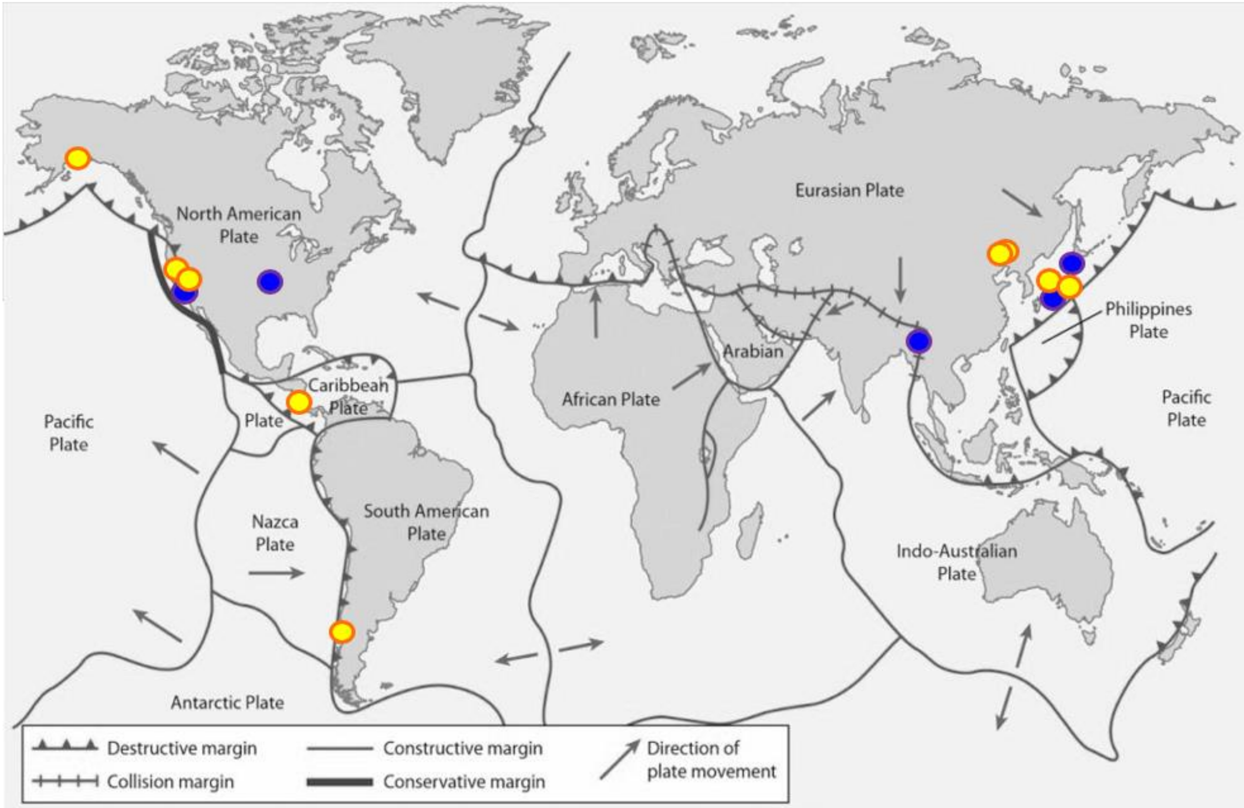

URM

Year	Earthquake	Location	M
1891	Mino–Owari Earthquake	Japan	8.0
1895	Charleston Earthquake	MO, USA	6.8
1897	Assam Earthquake	India	8.0
1925	Santa Barbara Earthquake	CA, USA	6.8
2011	Tōhoku Earthquake	Japan	9.1

URC

Year	Earthquake	Location	M
1906	San Francisco Earthquake	CA, USA	7.9
1948	Fukui Earthquake	Japan	7.3
1976	Tangshan Earthquake	China	7.8
1960	Valdivia Earthquake	Chile	9.5
1964	Alaska Earthquake	AK, USA	9.2
1978	Miyagi Earthquake	Japan	7.7
1989	Loma Prieta Earthquake	CA, USA	6.9
1991	Limon Earthquake	Costa Rica	7.7

Figure 2.3 Locations of damaged URM and URC railroad bridge piers in fault line map

is the Pajaro River railroad bridge in the 1906 San Francisco earthquake. A fault line crosses this bridge near the west end. Earth movement along the fault line increased the distance between the east and west abutments by 3.5 ft. and moved all 5 piers from their original position, as shown in **Figure 2.4**.

(2) Horizontal crack along construction joint in plain concrete piers - This is a typical failure mode for plain concrete piers. An example of this mode is Pajaro River railroad bridge in 1906 San Francisco earthquake (Duryea and ASCE 1907), as shown in **Figure 2.5**. Since the construction joints are the inherent defects within unreinforced concrete piers, cracking will occur when the tensile stress excesses the ultimate tensile strength at these inherent defects.

(3) Cracking of joints in brick or stone masonry piers - This is a typical failure for unreinforced masonry piers since the joints between masonry units are the weak points in these piers. Examples of this mode are the Dos Pueblos bridge on the Southern Pacific Railroad in the 1925 Santa Barbara Earthquake (Byers 2003) and a brick masonry railroad pier on the Shinkansen line in the 2001 Tohoku Earthquake, as shown in **Figure 2.6**, respectively. Similar to the construction joints in URC piers, weak bonding between the mortar and masonry units will lead to cracking when the bond is stressed.

(4) Sliding along the horizontal run-through cracks - An example of this mode is the Kuzuryu River railroad bridge in the 1948 Fukui earthquake (Far East Command 1949), as shown in **Figure 2.7**. The cracks initiated at the construction joints in URC piers and bed joints in URM piers. These joints are the inherent weak points of these structures. With intense shocks, run-through cracks develope along the weak bond between the blocks. The upper and lower parts slide along these run-through cracks when the horizontal earthquake load exceeded the friction resistance between the two parts.

(5) Tilting of upper portion of piers after the horizontal run-through cracks appeared- An example of this failure mode occurred at the piers of the Dou River railway bridge in the 1976 Tangshan Earthquake (Chen 1978), as shown in **Figure 2.8**. The upper partition of damaged piers tilted or rocked due to the excessive overturning moment. The tilted part may either return to the vertical position or remain tilted (as in the example of the Dou River railway bridge). Either condition can affect train operations after an earthquake because of the excessive displacement of the superstructure.

(6) Coping stone (pier cap): loosened, displaced, torn - An example of this mode is the Pajaro River railroad bridge in the 1906 San Francisco earthquake, as shown in **Figure 2.9**. The bond between the coping stone and main body of the pier may

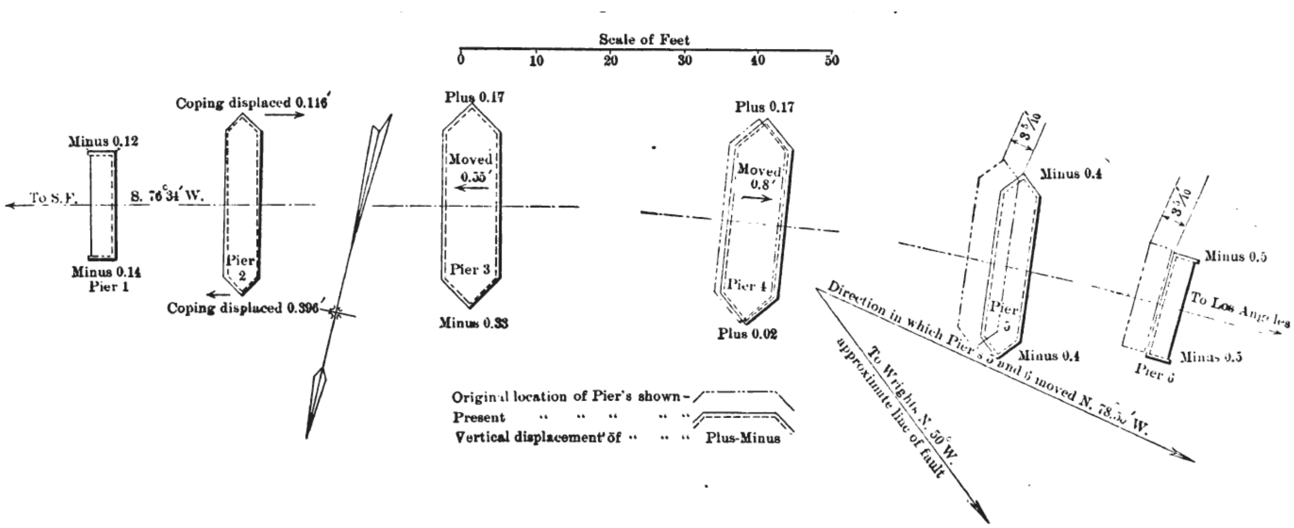

Figure 2.4 Displacement of Piers of the Pajaro River Bridge after 1906 San Francisco Earthquake (Duryea and ASCE 1907)

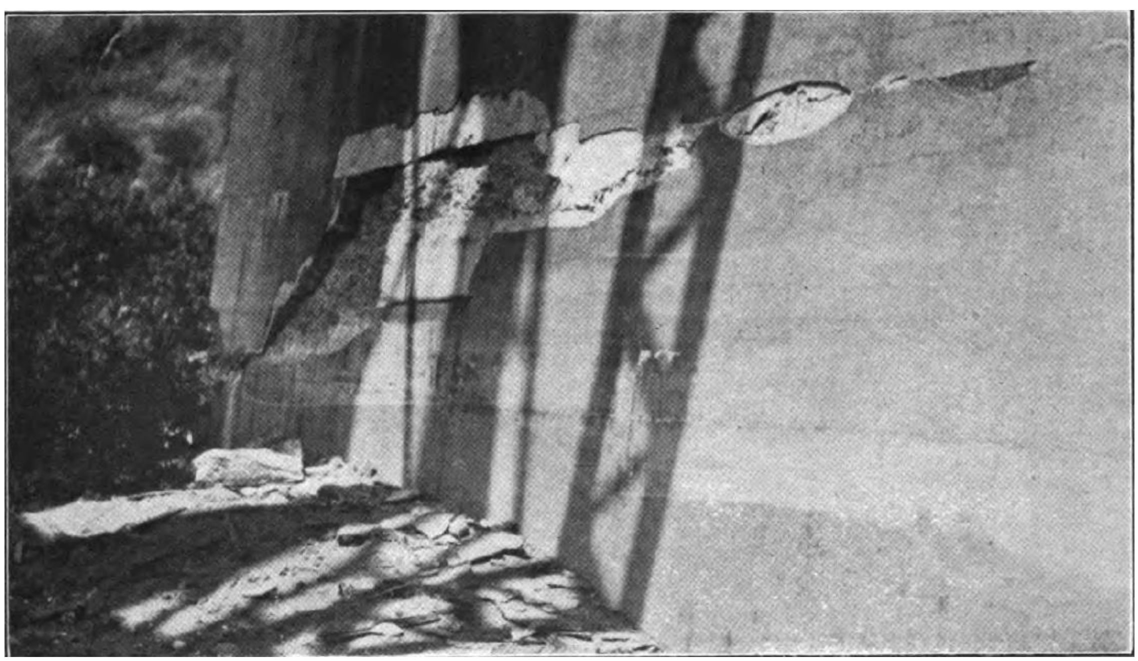

Figure 2.5 Cracking Damage at the Base of a URC Pier of Pajaro Bridge after 1906 San Francisco Earthquake (Duryea and ASCE 1907)

Figure 2.6 Cracking Damage of a URM Pier of Dos Pueblos Viaduct after 1925 Santa Barbara Earthquake (Kirkbride 1927)

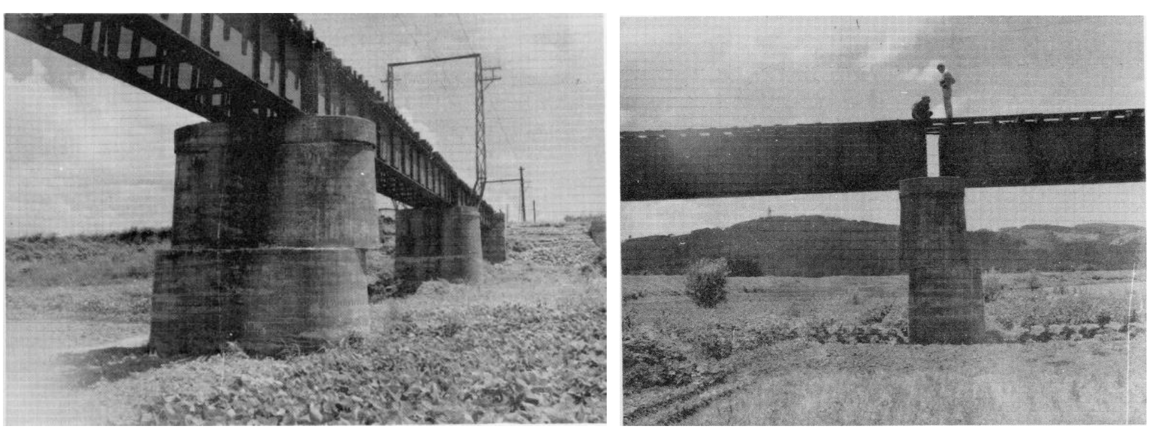

Figure 2.7 Sliding at a URC Pier of Kuzuryu River Bridge after 1948 Fukui Earthquake (Far East Command 1949)

Figure 2.8 Tilting of Upper Partition of URC Piers of Dou River Railway Bridge after 1976 Tangshan Earthquake (Chen 1978)

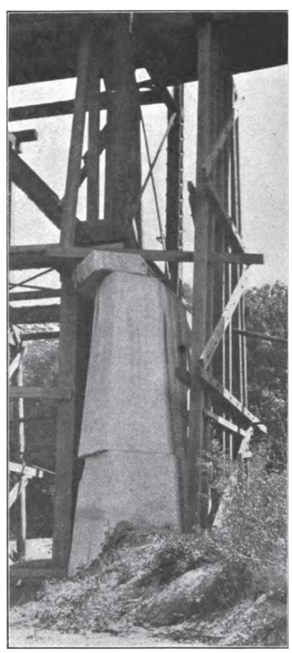

Figure 2.9 Damage at the Coping stone of a URC Pier of Pajaro Bridge after 1906 San Francisco Earthquake (Duryea and ASCE 1907)

become the weakest part within the substructure system. Displacement may occur under high shear force conditions.

(7) Anchorage failure between bearings and piers - An example of this failure mode is Bridge 14.5 in the 1964 Alaska earthquake (McCulloch and Bonilla 1970), as shown in **Figure 2.10**. Anchor bolts are the typical connection between the bearing and the pier. Thus, the anchorage strength is important when the bridge experiences high-level horizontal or vertical seismic excitation.

2.4 Seismic Design

In 1941, an earthquake load was first listed as a design load in section 3.2.1 of the bridge design code by the American Association of State Highway and Transportation Officials (AASHTO) (AASHTO 1941). However, there were no practical requirements to calculate seismic load and check the corresponding stresses. Following several major earthquakes in the past half century, AASHTO's seismic design provision for bridges was developed and improved, introducing stricter requirements.

In 1993, the American Railway Engineering and Maintenance-of-Way Association (AREMA) established a stand-alone committee (AREMA Committee 9) to develop seismic design guidelines specific to railroad structures. In 1994, guidelines for the design of railroad bridges under seismic forces were introduced in Chapter 9 of AREMA's Manual for Railway Engineering (MRE) (Moreu and LaFave 2012).

AREMA and AASHTO's current provisions for seismic design for bridge are discussed below:

Figure 2.10 Anchorage Failure at the Bearing of a URC Pier of Bridge 14.5 after 1964 Alaska Earthquake (McCulloch and Bonilla 1970)

2.4.1 AREMA MRE 2018

MRE Chapter 9 provides guidelines for seismic design of railroad bridges, along with commentaries and references (AREMA 2018).

General requirements: Three-level performance criteria must be satisfied in the bridge design process: serviceability limit state, ultimate limit state, and survivability limit state.

The serviceability limit state requires the critical members to remain in the elastic range under ground motion of 50-100 years average return period. Earthquake damage to bridges will not affect the safe operation of trains under restricted speeds.

The ultimate limit state requires that the strength and stability of the critical members will not be exceeded under ground motion with 200-500 years average return period. The integrity of the bridge structure should be preserved during this state. Ductility of the structure is required to minimize damage and the loss of use due to the large displacement caused by seismic excitation. Running trains need to stop under this level of ground motion until bridge inspections are completed.

The survivability limit state requires the structural survival of the bridge under ground motion with 1000-2400 years average return period. Further ductility capacity of the structure may be required to avoid collapse. Running trains need to stop under this level of ground motion until bridge inspections are completed.

Analysis: The methods recommended by MRE include Equivalent Lateral Force (ELF) Procedure and Modal Analysis (MA) Procedure. Typically, ELF is recommended for the analysis of regular bridges while MA is for the analysis of multi-span irregular bridges.

Design forces: To get the final seismic design loads, MRE allows combining the loads in each of the two principal directions of the structure using one of the following: (1) the square root of the sum of the squares (SRSS) method; and (2) an alternate method that includes combination of the forces in principle direction 1 with 30% of the forces from principle direction 2, and combination of the forces in principle direction 2 with 30% of the forces from principle direction 1.

The seismic design loads for the ultimate limit state and survivability limit state could be computed by increasing the forces under the serviceability limit state by the ratio of the Base Acceleration Coefficients which is determined per the formula and base acceleration maps in Section 1.3.2.3.

For bridge design of concrete structures, the load combination formula is **1.0D+1.0E+1.0B+1.0PS+1.0EQ** and load factor design shall be used. For bridge design of steel structures, the combination formula is **D+E+B+PS+EQ**, and allowable stress design shall be used. In the combination formulas, D, E, B, PS, and EQ stand for dead load, earth pressure, buoyancy, secondary forces from prestressing and earthquake load, respectively.

Response Limits: For bridge design of concrete structures, the design strength of each member shall follow the requirements in MRE Chapter 8, Concrete structures and foundations. For bridge design of steel structures, the allowable stresses for each member shall follow the requirements in MRE Chapter 15, Steel structures. Each member under design loads of three-level limit state shall be checked to satisfy the limit requirements in MRE.

Detailing considerations: To satisfy the performance criteria under the ultimate limit state and the survivability limit state, MRE lists corresponding requirements to guarantee the continuity, ductility, and redundancy of the bridge structure. Continuously welded rails (CWR) that satisfy certain requirements are considered to be a redundant load path for seismic load and to increase the damping improving the energy dissipating capacity of the structure.

Summary: The bridge seismic design approach specified in MRE 2012 contains no requirements on the response limit for URM or URC bridge piers. Thus, it is difficult to determine if the strength of URM or URC bridge piers matches the seismic criteria under the three-level limit state. Since URM or URC piers contain no reinforcement, old piers cannot be considered as structures with proper ductility capacity per the ductility provisions in MRE. Furthermore, it may be doubtful to utilize load factor design in analysis of old piers.

2.4.2 AASHTO LRFD Bridge Design Specifications 2017

AASHTO's requirements for the seismic design of highway bridges are in Section 3.10, 3.4, and 4.7 of the 2017 edition of LRFD bridge design specifications (AASHTO 2017).

General requirements: One-level force-based design criteria are adopted in the specifications. Earthquake ground motions with a 7% probability of exceedance in 75 years, i.e., a return period of about 1000 years, are defined as the design earthquake. Under this earthquake load, bridge structures satisfy the performance that have a low probability of collapse but may suffer significant damage and disruption to service. Higher performance levels may be adopted but need to be authorized by the bridge owner.

Based on the comments in the specifications, bridges are designed to resist small to moderate earthquakes within the elastic behavior range of the structural components. Collapse of bridge structures should be prevented during large earthquakes.

The specifications could provide adequate strength capacity to resist design force demands. However, the displacement capacity that is critical in the limit states is not under supervision by a designer. The comments in the specifications mention that bridges designed by the force-based method should be checked by displacement-based methods such as the *AASHTO Guide Specifications for LRFD Seismic Design* (AASHTO 2011), especially for high seismic zones.

Analysis: The requirements for the dynamic analysis method under earthquake loads are specified in Article 4.7.4 and summarized in Table 4.7.4.3.1-1 (shown in **Table 2.2**) in the specifications. Seismic analysis is not required for single-span bridges in all seismic zones and multi-span bridges in low seismic zones (Seismic Zone 1). Generally, uniform load elastic method (UL) and single-mode elastic method (SM) are recommended for regular bridges, and multimode elastic method (MM) is recommended for irregular bridges. For critical bridges in high seismic zones, either elastic or inelastic time history method (TH) may be required, based on seismic zone identification.

Design forces: Two load cases are considered during the combination of the seismic effect in two perpendicular horizontal directions. Load case 1 consists of 100 percent of the absolute value of the elastic seismic forces resulting from the seismic loading in the longitudinal direction, combined with 30 percent of the absolute value of the elastic seismic forces resulting from the seismic loading in the transverse direction. Similarly, load case 2 consists of 100 percent of the absolute value of the elastic seismic forces resulting from the seismic loading in the transverse direction; combined with 30 percent of the absolute value of the elastic seismic forces resulting from the seismic loading in the longitudinal direction.

Earthquake load is considered in the “Extreme Event I” load combination in the AASHTO 2017 LRFD bridge design specifications. The total factored force effect for bridge piers under this combination is:

Table 2.2 Minimum Analysis Requirements for Seismic Effects (AASHTO 2017)

Seismic zone	Single-span bridges	Multi-span bridges					
		Other bridges		Essential bridges		Critical bridges	
		regular	irregular	regular	irregular	regular	irregular
1	No seismic analysis required	*	*	*	*	*	*
2		SM/UL	SM	SM/UL	MM	MM	MM
3		SM/UL	MM	MM	MM	MM	TH
4		SM/UL	MM	MM	MM	TH	TH

$$Q = \sum \eta_i \gamma_i Q_i$$

$$= \eta_{DC}\gamma_p DC + \eta_{LL}\gamma_{EQ} LL + \eta_{WA} \times 1.0 \times WA + \eta_{FR} \times 1.0 \times FR + \eta_{EQ} \times 1.0 \times EQ$$

where:

η_i = load modifier specified in article 1.3.2, $\eta_i = \eta_D \eta_R \eta_I$, for the Extreme Event limit state, η_{DC}, η_{LL}, η_{WA}, η_{FR}, η_{EQ} are taken as 1.0

η_D = a factor relating to ductility, as specified in Article 1.3.3, for the Extreme Event limit state η_D =1.0

η_R = a factor relating to redundancy as specified in Article 1.3.4, for the Extreme Event limit state η_R =1.0

η_I = a factor relating to operational classification as specified in Article 1.3.5, for the Extreme Event limit state η_I =1.0

γ_p = load factors for permanent loads, γ_p were taken as 1.0 in this example

γ_{EQ} = load factor for live load applied simultaneously with seismic loads, γ_{EQ} could be taken as 0.5 for a common condition according to art.C.3.4.1

DC = dead load of structural components and nonstructural attachments

LL = vehicular live load

WA = water load and stream pressure, in this example: only buoyancy was considered

FR = friction load, in this example: friction load was neglected

EQ = earthquake load

AASHTO 2017 LRFD bridge design specifications require that seismic design force for individual components and connections of bridges be determined by dividing the elastic forces obtained from the analysis by the appropriate Response Modification Factor (R) (ACI et al. 2003) specified in Table 3.10.7.1-1 and Table 3.10.7.1-2 (shown in **Table 2.3** and **Table 2.4**). The R-factors are obtained by assuming that the individual components will yield and develop a ductile mechanism under the calculated design seismic loads. Thus, detailing considerations need to be guaranteed to make sure that the mechanism is formed without brittle behavior.

Response Limits: For concrete and steel structures design, the response limits must follow the requirements in Sections 5 and 6, respectively.

Table 2.3 Response Modification Factors for Substructures (AASHTO 2017)

Substructure	Operational category		
	Critical	Essential	Other
Wall-type piers (larger dimension)	1.5	1.5	2.0
Reinforced concrete pile bents			
• Vertical piles only	1.5	2.0	3.0
• With batter piles	1.5	1.5	2.0
Single columns	1.5	2.0	3.0
Steel or composite steel and concrete pile bents			
• Vertical pile only	1.5	3.5	5.0
• With batter piles	1.5	2.0	3.0
Multiple column bents	1.5	3.5	5.0

Table 2.4 Response Modification Factors for Connections (AASHTO 2017)

Connection	All Operational Categories
Superstructure to abutment	0.8
Expansion joints with a span of the structure	0.8
Columns, piers, or pile bents to cap beam or superstructure	1.0
Columns or piers to foundations	1.0

Detailing considerations: To guarantee the ductility and redundancy of bridges under seismic loading, AASHTO provides several requirements on the detailing design, e.g., the minimum support lengths of bearing seats, detailing of the expansion joints and restrainers, design of the abutments, hold-down devices and shear keys, etc. Furthermore, AASHTO published guidelines on the design and application of the seismically isolated bridges in 1991 (AASHTO 1991).

Summary: The current edition of AASHTO's bridge design code is based on the research findings and engineering experience of recent years. The requirements are not applicable for URM or URC piers built a century ago. For example, the ductility concept that is fundamental in the current code is based on the post-yield behavior of reinforced concrete members. Since no reinforcement was embedded in the old piers, they cannot be analyzed as components with ductility capacity. Meanwhile, no requirements are provided for the response limits on the URM and URC members in the current code.

2.4.3 AREMA MRE 1907

As mentioned previously, since currently more than half of the railroad bridges in U.S. were built before 1920, it is reasonable to review the design code for railroad bridges of a century ago to build a solid foundation for the analysis of these historical piers.

The first edition of the MRE by AREMA was published in 1900, the same year AREMA was established, and its contents have been refreshed or renewed annually. In 1907, the specifications for design loads of railroad bridges were first listed in MRE section "Iron and Steel Structures" (AREMA 1907). Some significant differences from the current code are summarized below:

Live load: The minimum live load for each track is specified to be Cooper's E-40. This requirement was changed to E60 in the 1920 edition, E72 in the 1935 edition, and E80 in the 1967 edition. The current code specifies E80.

Lateral load: The lateral load on the loaded chord was specified at 200 lbs. per linear foot plus 10 percent of the specified train load on one track. The lateral load on the unloaded chord was specified to be 200 lbs. per linear foot.

Wind load: Substructures must be designed for a lateral force of 50 lbs. per sq. ft. on one and one-half times the vertical projection of the structure unloaded; or 30 lbs. per sq. ft. on the same surface plus 400 lbs. per linear ft. of the structure applied 7 ft. above the rail for assumed wind load on train when the structure is either fully loaded or unloaded on either track with empty cars assumed to weigh 1200 lbs. per linear ft., whichever gives the larger load.

Longitudinal load: Substructures must be designed for a longitudinal force of 20 percent of the live load, applied to the rail.

Besides the design load, the analysis method and response limit are different from the design of railroad piers of a century ago. According to treatises and textbooks of that era (Baker 1909; Derleth 1907; Ketchum 1921), safety checking for railroad bridge piers could be generalized as follows:

(1) Calculate the forces to be resisted.
(2) Determine load cases.
(3) Calculate overturning moments and resistance moments under each load case in both directions.
(4) Examine the safety factors against overturning under each load case in both directions.
(5) Calculate sliding forces and resistance to sliding under each load case in both directions.

(6) Examine the safety factors against sliding under each load case in both directions.
(7) Calculate maximum and minimum "intensities of pressure", i.e. stresses, on subfoundation under each load case in both directions.
(8) Check the safety factors of maximum stress under each load case in both directions to avoid crushing of the substructure at the edge of the subfoundation.
(9) Check the safety factors of minimum stress under each load case in both directions to avoid the uplift of the substructure at the edge of the subfoundation.

According to this process, we find that the design of old URM and URC piers includes safety factors for overturning and sliding at critical sections and the allowable stress check for masonry or concrete material at the base of the substructures. The analysis is under elastic behavior, which is different from the ultimate strength analysis used in current codes. "Over-engineered" design was typical in that era. For example, the safety factors against overturning and sliding are typically taken to be 3.0 or more (International Correspondence Schools 1908). This explains the strong appearance of old URM and URC piers.

2.4.4 Code for Seismic Design of Railway Engineering (GB50111-2006 (2009 Edition)) in China

The first edition of the seismic design code for railway engineering in China was published in 1977. This code was amended and supplemented comprehensively in 1987 and 2006. After 30 years of development, the seismic design concept in the Chinese code has gradually changed from strength-based design to displacement-based design with ductility design consideration (Ni 2005). In 2009, to satisfy the rapid development of high-speed rail (HSR) in China, several supplements to the requirements on seismic design of HSR bridges were adopted in GB50111-2006 (2009 Edition) (NRA China 2009). This was adopted by *Code for Design of High Speed Railway* (TB10621-2014) in 2014 (NRA China 2014). The experiences summarized from the M8.0 2008 Sichuan earthquake have been integrated into GB50111-2006 (2009 Edition).

General requirements: In GB50111-2006 (2009 Edition), railway bridges are categorized into four seismic protection levels:

Level A: Significant bridges with a long span or complex structural type or difficulty in recovering from severe earthquake damage.

Level B: (1) for a regular speed railroad, simple support concrete girder bridges with span ≥ 48 m (158 ft.), simple support steel girder bridges with span ≥ 64 m (210 ft.), continuous concrete girder bridges with main span ≥ 80 m (263 ft.), continuous steel girder bridges with main span ≥ 96 m (315 ft.); (2) for High-speed Rail (HSR), bridges with span ≥ 40 m (131 ft.); (3) bridges with pier height ≥ 40 m (131 ft.); (4) normal water depth ≥ 8 m (26 ft.); (5) regular bridges with long span or complex structural type or difficulty to recover from severe earthquake damage.

Level C: (1) HSR bridges except those defined in Level B; (2) bridges with pier heights from 30 m (99 ft.) to 40 m (131 ft.); and (3) bridges with normal water depth from 5 m (17 ft.) to 8 m (26 ft.).

Level D includes: all other railway bridges not defined in Levels A, B, or C.

According to GB50111-2006 (2009 Edition), railroad bridges are designed to withstand three levels of earthquake motion: low-level earthquake, design earthquake, and high-level earthquake. The return periods of the three-level earthquake are 50, 475 and 2475 years respectively. The requirements for the performance of railroad bridges under these three earthquake motions are:

After a low-level earthquake, bridges must retain design operational functions without damage or with little damage. Structures must work in the elastic range.

After a design earthquake, bridges must recover design operational functions in a short period with repairable damage. Structures might work in the inelastic, exceeding elastic limits, range.

After a high-level earthquake, bridges must survive without integral collapse. After emergency repairs, bridges must be able to support a train under restricted speeds.

The requirements for seismic design checking are listed in **Table 2.5**. Specifically: (1) checks on a strength, eccentricity and stability are required for low-level earthquake; (2) connection detail must be checked for the design earthquake; (3) Ductility checks may be required for the high-level earthquake.

Analysis: For simply supported bridges, the seismic analysis can be made by single pier modeling that considers the mass effect from the superstructure or whole bridge modeling considering the stiffness effect from the superstructure.

For low-level earthquake design, the response spectrum method is recommended for Level B bridges. Besides the response spectrum method, the time-history analysis method is recommended for Level B and C bridges and new structural type bridges.

For design earthquake design, the static analysis method is recommended. The response spectrum method should be used to design bearings in continuous bridges.

For high-level earthquake design, simplified time-history analysis method is

Table 2.5 Seismic Design Checking Requirements (NRA China 2009)

Type		low-level earthquake	Design earthquake	high-level earthquake
simple support girder bridges	plain concrete	pier and foundation: checking on strength, eccentricity and stability	checking on connection details	no requirement on checking, casing reinforcements are required
	reinforced concrete	pier and foundation: checking on strength and stability	checking on connection details	checking on ductility by using simplified method
Other girder bridges and Level B bridges		pier and foundation: checking on strength, eccentricity and stability	checking on connection details	for reinforced concrete piers: checking on ductility and maximum displacement by using non-linear time-history response analysis method

recommended for the reinforced concrete piers of simply supported bridges. The nonlinear time-history analysis method is recommended for Level B bridges and new structural type bridges.

Design forces: Calculation of horizontal seismic loadings in both longitudinal and transverse directions is required during the seismic checking process. For cantilever structures and prestressed concrete rigid frame bridges with design intensity of 9 degrees, the vertical seismic load must be taken into account. The vertical seismic load should value is either 7% of the sum of dead load and live load, or the result of dynamic analysis by 65% of the fundamental horizontal acceleration (a). However, the combination of seismic loads in longitudinal and transverse directions is not considered in GB50111-2006 (2009 Edition).

The critical combinations of the seismic loads with other loads, i.e. self-weight, earth pressure, hydrostatic pressure, buoyancy force, live load, centrifugal force and earth pressure by live load, must be checked under both with-train and without-train conditions. For the with-train condition: (1) seismic load in longitudinal direction caused by live load is not taken into account; (2) 50% of the seismic load in transverse direction caused by live load is applied at 2 meters above the top of rail.

Response limits: The requirements for the response limits of railroad structures are included in *Code for Design on Subsoil and Foundation of Railway Bridge and Culvert* (TB10002.5-2005). The allowable stress method is adopted in TB10002.5-2005.

Detailing considerations: The requirements for detail design provided in GB50111-2006 (2009 Edition) guarantee the ductility of the bridge piers. For example, the maximum longitudinal reinforcement ratio, minimum diameter of stirrups, minimum transverse reinforcement ratio, and maximum stirrup spacing are recommended both within and outside the plastic hinge zone. The detailing of welding and hooking are suggested as well.

The nonlinear time-history analysis method is recommended for checking after a high-level earthquake. Based on the results from the time-history analysis, the ductility ratio is calculated using the following equation:

$$\mu_u = \frac{\Delta_{\max}}{\Delta_y} < [\mu_u]$$

Where:

μ_u	=	displacement ductility ratio
$[\mu_u]$	=	limit on displacement ductility ratio, set to be 4.8
$\Delta_{\max}$	=	maximum displacement of the piers under nonlinear response analysis
Δ_y	=	yield displacement of the piers

2.5 Seismic Assessment

As mentioned previously, railroad bridges have historically performed well in earthquakes, suffering little or no damage. However, due to limited knowledge about earthquake characteristics and bridge seismic behavior, URM and URC bridge piers designed and built a century ago may not have adequate capacity, e.g. strength and deformation, to resist shocks in the future despite surviving previous earthquakes. Considering the uncertainty of earthquake location and intensity, future seismic damage to the piers is unpredictable. Thus, it is necessary to evaluate the strength and deformation capacity of old piers using proper seismic assessment approaches.

Interest in seismic research and corresponding retrofit methods increased after the severe damage to highway bridges in the 1971 San Fernando Earthquake. In 1983, the Applied Technology Council (ATC) issued guidelines for seismic retrofitting for highway bridges (ATC 1983). Meanwhile, more research was carried out in the 1980s (ACI et al. 2007). The earlier guidelines and approaches for seismic assessment and retrofit of bridges were based solely on strength-based methods without considering the inelastic behavior of the structure after yield and the deformation demand on the bridges. Damage in the Loma Prieta and Northridge Earthquakes raised concern from bridge community on this issue.

Over the past three decades, researchers have been pursuing comprehensive assessment methods that can take into account both the strength and deformation capacities at component and structure levels. In this procedure, the deformation-based approach and the energy-based approach were adopted as guidelines for the seismic assessment and retrofit successively in the 1990s (ACI et al. 2007).

Recently, seismic engineering societies have broadly accepted the performance-based evaluation method. AASHTO and AREMA have adopted the concept in their guidelines and design code. In this method, instead of placing sole emphasis on the ultimate capacities of structures at maximum design seismic loading, the capacities of bridges are evaluated for multiple earthquake levels. Design or retrofit will satisfy multiple performance objectives under diverse seismic hazard levels. For example, under low-intensity and frequent seismic loading, elastic behavior may be needed for structures to satisfy the performance with need to repair. Under moderately-intensive seismic loading, inelastic behavior and limited repairable damage may be allowed. Under severely-intensive earthquakes, the ultimate capacity needs to be evaluated and the bridge retrofitted to avoid collapse.

The seismic evaluation procedure for a bridge includes: (1) evaluation of the seismic demand on the structural components; (2) evaluation of the capacity of each component; and (3) examination of the demand-capacity ratio and identifying the potential damage in the components and structural system (ACI et al. 2007).

The common analytical methods of seismic demand evaluation are reviewed and introduced below:

Linear elastic analysis methods (AASHTO 2017; AREMA 2018): The common linear elastic analysis methods include the single-mode response spectrum method, the multimode response spectrum method, and the linear time-history analysis method. For simple or regular bridges whose structural response can be represented approximately with the fundamental vibration mode dynamic model, the single-mode response spectrum method is adequate to obtain the seismic demand. For irregular bridges where single-mode response is not adequate to represent the structural response under seismic excitation, the multimode response spectrum and linear time-history analysis methods are required. Force demands are obtained from the linear elastic analysis by these methods. The force demands are reduced by a response modification factor R (as shown in **Table 2.3** and **Table 2.4**) to account for the ductility of the analyzed components in AASHTO's LRFD 2017 design code.

Nonlinear analysis methods (ASCE and FEMA 2000): The common nonlinear analysis methods include the limit analysis method, the pushover analysis method paired with linear dynamic analyses, and the acceleration time-history analysis method. The limit analysis and pushover methods pertain to static nonlinear procedures. The limit analysis method is developed using the virtual work principle. In limit analysis, the location of plastic hinges needs to be assumed appropriately to obtain a reasonable mechanism after yield. But this limits the application of this method to complex structures because it is difficult to find a proper collapse mechanism. The pushover analysis method is used to estimate member demands, the monotonic force-displacement relationship, and the displacement capacity of the structural system. However, this method may result in unrealistic seismic demands in members if misassumptions are made about the boundary condition, deck stiffness, and coherence of the ground motions (ACI et al. 2007). The acceleration time-history method is a more complex, nonlinear analysis approach, but it could approach the real response of the structures if reasonable simplifications are used.

Evaluating the actual capacities of the components and structural system is another significant part of the demand-capacity ratio procedure. It can be accomplished in the following steps (ACI et al. 2007; Priestley et al. 1996):

(1) Identify the actual properties of the material: To obtain the real capacities of components, it is important to use the actual material properties in the analysis. As the material properties in the design codes are conservative with the reliability consideration, the properties from codes cannot be used directly in the seismic capacity analysis of structures. It is preferred to obtain the actual strength from material testing on the existing piers. However, several adjustments on the material strength may be taken based on the recommendations in relevant literature. For example, a 50% increase in the concrete design strength and 10% overstrength in the yield strength of reinforcement is suggested to estimate the actual strength in ATC-32 (Nutt et al. 2000). The adjustment parameters are 70% and 10% for concrete and reinforcement, respectively, in MCEER/ATC-49 (ATC MCEER Joint Venture and NCHRP 2003).

(2) Calculate the flexural capacities of individual components based on moment-curvature analyses: Actual material properties, stress-strain relationships of concrete and reinforcements with consideration on the confinement effect and strain-hardening behavior need to be used.

(3) Calculate the lower-bound shear capacities of individual components based on specified material properties: Although there is no consensus within the engineering community which shear capacity equation is the best, most provide conservative estimates for the shear capacity of members tested in the laboratory

(ACI et al. 2007). Thus, it is reasonable to estimate the shear capacity of members using the smallest result from these suggested equations.

(4) Evaluate the anchorage of reinforcement and shear strength of joints

(5) Determine strengths of footings, pile-cap connections, and piles

(6) Determine the bridge response by considering the bridge as an individual framing system

Based on the results of demand and capacity analyses, the demand-capacity ratio can be determined and evaluated. The critical sections should be located where the demand-capacity ratios exceed unity. Appropriate retrofit measures could be applied to these critical sections based on the seismic assessment results.

2.6 Seismic Retrofit

After the seismic assessment analyses, two decisions need to be made at the beginning of a bridge seismic retrofit: (1) whether the critical sections with damage risk are worth retrofitting and (2) which level the bridges should be retrofitted to (Priestley et al. 1996). These two issues must be analyzed in light of the available financial resources and cost-effectiveness analysis. Since these issues are at least partially in the domain of economics, they are not discussed as major topics in this research. The engineered retrofit design, measures, and implementation for URM and URC railroad bridge piers are the major topics in this research, while cost-effectiveness analysis will be discussed preliminarily.

The retrofit design sections in current codes are reviewed and summarized below:

(1) AREMA MRE 2018: The purposes of retrofit schemes are listed in the code (AREMA 2018): (1) change the dynamic response to reduce the global seismic demand in a structure; (2) strengthen components to increase the local seismic capacity; (3) provide alternate paths for seismic loading to improve the redundancy of a structural system; (4) provide restrainers, extended bearing seats, and other devices to accommodate displacements; (5) design non-critical components to post-yield response to increase the ductility of a structure and relieve the seismic stresses of critical components. These considerations represent the requirements on seismic demand, seismic capacity, ductility, and redundancy to the bridge seismic retrofit design. However, there are no more detailed design guidelines for bridge retrofit in the MRE.

(2) FHWA Seismic retrofitting Manual for Highway Bridges: The performance-based retrofit philosophy is used in the design requirements in the FHWA manual

(Buckle et al. 2006). Performance criteria are given for two earthquake ground motions with different return periods, 100 and 1,000 years. A higher level of performance is required for the event with the shorter return period (the lower level earthquake ground motion) than for the longer return period (the upper level earthquake ground motion). Criteria are recommended according to bridge importance and anticipated service life, with more rigorous performance being required for important, relatively new bridges, and a lesser level for standard bridges nearing the end of their useful life. Retrofitting measures are designed according to an assigned Seismic Retrofit Category (SRC). Bridges in Category A need not be retrofitted whereas those in Categories B, C and D require successively more rigorous consideration and retrofitting as required.

Retrofit measures and implementation for bridge piers are reviewed and summarized as below:

(1) Steel jacketing (Priestley et al. 1996): In this measure, two half shells of steel plate are placed around the pier. The gap between the steel and pier is filled with cement grout. This measure is applicable to circular and rectangular columns (as shown in **Figure 2.11**). The jacket increases the reinforcement ratio of the cross-section, also providing effective confinement to the core concrete pier. This measure can improve the seismic capacity effectively. U.S. bridges treated in this manner behaved well during the 1994 Northridge Earthquake.

(2) Concrete jacketing (Priestley et al. 1996): In this measure, a reinforced concrete jacket is placed around the pier (as shown in **Figure 2.12**). This improves the seismic capacity, e.g. flexural strength and shear strength, and ductility of the piers. In the U.S., this measure has been used in several railroad retrofit projects on piers with under-reinforcement. For example, from 1949 to 1952, the concrete

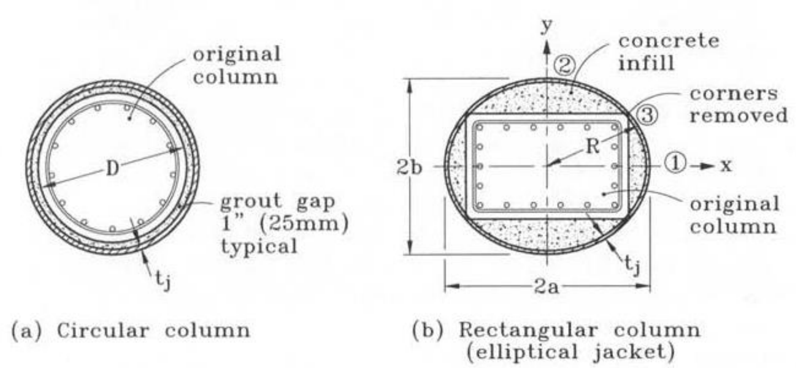

Figure 2.11 Typical Cross-section Layout of Steel Jacketing Retrofit (Priestley et al. 1996)

jacketing approach was used in retrofitting the substructure of the Illinois Central Railroad Cairo Bridge over the Ohio River (Modjeski and Masters 1953). This project included replacement of all six truss spans and retrofitting three stone masonry piers. These masonry piers were built in 1889 and developed cracks along the mortar joints after the 1895 M6.6 Charleston Earthquake. The piers were strengthened by placing a 2 ft. thick concrete jacket reaching up to bottom of the stone coping. This concrete jacket was attached with expansion anchors to alternate stone courses by a pattern of anchors approximately 4 ft. on centers. Reinforced consisted of ¾ in. diameter bars with horizontal bars at 12 in. centers and vertical bars at 18 in. centers. This retrofit is shown in **Figure 2.13**. Composite-Material Jackets: Retrofit could be made using carbon-FRP (Fiber Reinforced Polymar) or Glass-FRP bonded to the column with epoxy. This approach has been proved effective in laboratory tests (Priestley et al. 1996). This measure could provide confinement for the core concrete and increase the ductile behavior of the piers. However, debonding of the epoxy adhesives may lead a durability issues for FRP retrofitted piers (Au and Büyüköztürk 2006). In 2011, Choi et al. conducted a study on the application of FRP-steel plate (FSP) for retrofitting plain concrete piers in Korea (Choi et al. 2011). FSP is a type of sandwich composite consisting of a steel plate between two FRP plates. With the steel plate, this hybrid material could be fixed to the pier body by durable anchoring instead of adhesive layers. An effective retrofit scheme with FSP material is developed in this study to restrict joint cracking and improve displacement capacity and strength in bending.

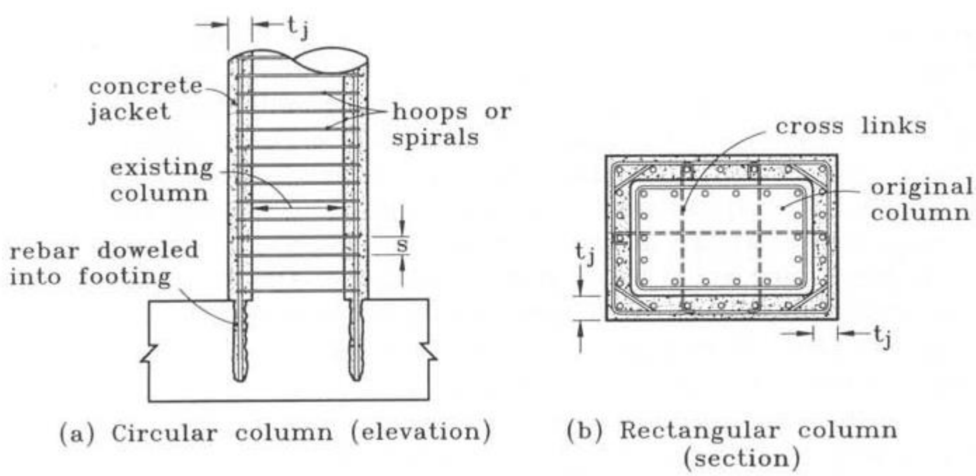

Figure 2.12 Typical Layout of Concrete Jacketing Retrofit (Priestley et al. 1996)

Figure 2.13 Construction of the RC Jacket Retrofitting at a URM Pier of the Illinois Central Railroad Cairo Bridge over the Ohio River (Modjeski and Masters 1953)

(3) External prestressing: URM and URC piers have inherent weakness under seismic load due to the presence of mortar joints or construction joints. These piers may be severely damaged by an earthquake when loads produce tensile stress. A retrofit measure by stressing the plain piers vertically with external prestressing cables has been utilized in New Zealand railroad bridges (Walsh 2002). As shown in **Figure 2.14**, caps are built at the top and bottom of the old piers. Prestressing strands protected by steel ducts are placed and prestressed between the top and bottom caps. The prestressing forces the mass piers into controlled compression loading, reducing the possibility of tension stresses developing during the earthquakes.

(4) Reinforced shotcrete overlay, grouted reinforcing bars within drilled cores (Abrams et al. 2007): Abrams et al. conducted several model tests on retrofit schemes for URM brick wall piers. The tests evaluated reinforced shotcrete overlay and grouted reinforcing bars within drilled cores. The results indicated that reinforced shotcrete is an effective retrofit approach due to deformation capacity and energy-dissipation through yielding of the reinforcement. Grouted reinforcing bars within drilled cores provided a moderate improvement to the lateral resistance capacity of URM piers due to the insufficient anchorage of the

Figure 2.14 External Prestressing Retrofit at a URC Railroad Bridge Pier in New Zealand (Walsh 2002)

grout core. The slip of the core in its cavity resists the yield of the embedded steel bars and limits the ductile behavior of the piers.

2.7 Conclusions and Recommendations

URM and URC railroad bridge structures built up to a century ago still serve a considerable percentage of in-service U.S. railroad bridges. Research, literature, and provisions in code about seismic performance of URM and URC railroad bridges are reviewed to explore reasonable research approaches for evaluating the resistance capacity of these bridges in future earthquakes. The findings are summarized below:

(1) Previous seismic research on railroad bridges has concentrated in two areas: seismic performance of piers in past earthquakes and seismic experimental and theoretical research. However, these studies did not focus on URM and URC railroad piers.

(2) In this study, the performance records of old URM and URC railroad bridge piers in past earthquakes are synthesized and summarized. Recorded damages are tabulated in Appendix A. Records show that old railroad bridge structures performed well in earthquakes. However, if damage appeared, it was highly possible to be severe. Typical failure modes of URM and URC bridge piers under earthquake loads include: (1) integral displacement in horizontal or vertical directions or integral tilting; (2) horizontal cracks along construction joints in

URC piers; (3) cracking of mortar joints in brick or stone masonry piers; (4) sliding along the horizontal run-through cracks; (5) tilting of the upper portion of piers after horizontal run-through cracks form; (6) coping stone failure, e.g., loosened, displaced, or torn; (7) anchorage failure between bearings and piers. These failure modes are considered in evaluation of theoretical analytical results and selection of retrofit measures.

(3) The design of old URM and URC railroad bridge piers was based on an elastic analysis approach. The process included checks of the safety factors of overturning and sliding at critical sections and the allowable stress of masonry or concrete material at the base of the substructures. This design philosophy is different from requirements in current design codes such as AREMA MRE, AASHTO LRFD Specifications and Chinese GB50111-2006. These codes have no requirements for the response limits of URM and URC structures. Thus, further studies need to be carried out to determine a proper approach for evaluating the actual capacity of old piers under seismic loading.

(4) Performance-based evaluation method is broadly accepted by seismic engineering societies. Multi-level performance objectives under diverse seismic hazard levels are considered in the capacity evaluation of bridge structures. Different analysis methods, e.g., single-mode or multimode response spectrum method, linear time-history analysis method, limit analysis method, pushover analysis, and non-linear time-history analysis method could be used in seismic demand evaluation of URM and URC piers. The proper method should be selected by considering structural regularity, assumptions on the boundary condition and structural stiffness, and calculation capacity, etc.

(5) Based on review of current seismic retrofit provisions in codes, it is reasonable to employ retrofit schemes with multi-level performance criteria, according to the importance and service life of the bridges. It might be appropriate to use the performance criteria in the design provision of the AREMA MRE. Further theoretical or experimental research may need to be implemented to determine proper measures specified for URC and URM railroad bridge piers.

Chapter 3:

Restraining Effect of Rail Track Structure on the Performance of Railroad Bridge under Lateral Load

3.1 Introduction

Railroad bridges typically have better seismic performance as compared to highway bridges (Byers 1996, Cook et al. 2006). The track system was considered as a contributor to this better performance because it can act as a restraint against horizontal movement of the superstructure during earthquakes (AREMA 2018).

1994 to 1995, two full-scale field tests on a railroad ballast deck through-plate girder bridge with jointed rail track were conducted by AAR, Caltrans, and UNR. One of the tests evaluated the impact of the continuity of the rail track structure between the deck and adjacent roadbed on the dynamic response of the bridge superstructure (Maragakis et al. 1996; Sandirasegaram 1997). The other test investigated the static ultimate capacity of the deck-abutment connections when the bridge superstructure was pushed in the lateral direction (Maragakis et al. 2001).

In 1998, a field test on a 5-span 18.9-m (62-ft), open-deck deck-plate-girder (DPG) steel bridge with jointed rail track subjected to lateral and longitudinal loading was conducted by the Transportation Technology Center, Inc. (TTCI) (Otter et al. 1999a; Uppal et al. 2000). The resistance to lateral and longitudinal displacement provided by anchor bolts, frictional and locking forces, and the continuous rail was identified in the test.

In 2000, a field test on two open-deck I-beam railroad spans to examine the resistance to longitudinal movement provided by the track structure was conducted by TTCI (Doe et al. 2001; Uppal et al. 2001). Several critical friction properties that contribute to the resistance of longitudinal movement of the bridge superstructure were investigated separately, including the coefficient of friction between rails and ties, the coefficient of friction between ties and the bridge girder, and the coefficient of friction between the girder bearings and pier head.

These full-scale field experiments systematically studied the restraint effect on the horizontal movement of bridge superstructure from the rail track structure for both ballast deck bridges and open deck bridges. However, the restraint effect of the rail track structure on the performance of bridge piers was not explored. Meanwhile, there exists a need to analyze these field experiments theoretically by using numerical approaches.

In this study, a structural analysis model of the rail track structure under lateral pushing load was developed by treating the rail as a continuous beam with support at each anchor position between rail and ties. The connection between the ties and the bridge superstructure was modeled as a rigid link element for open deck railroad bridges and as a spring link element for ballasted deck railroad bridges. The proposed model was implemented for ballast-deck and open-deck girder bridges and verified with the data from the previous field testing. A parametric study was conducted to investigate a range of the stiffness of the rail track structure under lateral loading.

Several studies were conducted on the numerical modelling methods to investigate the behavior of rail track system. For instance, Dong et al. (1994) developed a two-dimensional finite element model of a long track consisting of rail, tie and ballast to study the dynamic interactions between trains and rail track. With the calculation capacity limitation at that time, the tie was modelled as a lumped mass and the ballast was modelled as a one-dimensional linear spring element. A nonlinear wheel-rail contact model was proposed by using a set of vertical contact spring elements distributed between the wheel and rail. Since the concern of the study is on the wheel loading applied onto the track structure, the discussions were carried out on the influence of the axle weight and wheel rotation speed, the ballast stiffness in the wheel loading direction. In Ganesh Babu and Sujatha's study (2010), the finite element models of a 1.95-meter rail track section with consideration of subgrade, ballast and rail pad parameters were developed to investigate the influence of prestressed and wood crossties on the ground vibrations excited by cyclic axle loads. The FE model was developed in three-dimensions, however the material properties of the track components, e.g. rails, concrete and wood ties, ballast and subgrade, are assumed to be linear elastic. There are also other similar studies that investigate the behavior of the rail track system by the finite element method. However, they are concerned with either the interaction of the vehicle, wheel and track or the evaluation of different types of crossties. The numerical modelling that evaluates the effect of rail track structure on the behavior of bridge superstructures and substructures has not been thoroughly studied. This study proposes a three-dimensional numerical analysis approach in SAP2000 that investigates the interaction between the rail track and the bridge structure by considering the nonlinear properties of steel and concrete materials as well as the nonlinear behavior of the ballast and bearings subjected to lateral loads. The modelling considerations are introduced below.

3.2 Modelling Based on Previous Experimental Studies

3.2.1 Modelling for Uppal et al. (2000) testing

3.2.1.1 Introduction of the testing and continuities of rail track along the bridge in the modelling

Uppal et al. (2000) tested a single-track open deck bridge in Cincinnati, OH. (referred to as the Cincinnati Bridge). The bridge had seven spans with identical 18.9-m (62-ft) riveted steel deck-plate-girders. The spans rested on flat-plate bearings and were supported by concrete piers. Five tests, including three lateral pushes and two longitudinal pushes, were implemented on these seven bridge spans. The layout of this testing program is shown in **Figure 3.1**.

In this study, the leftmost three spans, spans 16, 17 and 18 in **Figure 3.1** are modelled. The rail and guardrail are continuous between span 16 and the embankment at the abutment, are continuous between spans 16 and 17 at pier 16 and are discontinuous between spans 17 and 18 at pier 17. The modeling considerations of the components and their connections for this bridge system is discussed below. As an example, the correlation between the model and the physical bridge at pier 16 of Cincinnati bridge is illustrated in **Figure 3.2**.

3.2.1.2 Rail track and guardrail track

The American Railway Engineering and Maintenance-of-Way Association (AREMA) standard rail with 196.4 kg/m (132 lb/ft) unit weight was used as the rail track for the Cincinnati Bridge. AREMA standard rail with 148.8 kg/m (100 lb/ft) was used as the guardrail. ASTM A499 (ASTM International 2015) Grade 50 steel was used for the rail and guardrail. The rails are modelled as wide flange sections with cross-sectional properties of the actual rail section. The rail material properties include: yield strength 344.7 MPa (50 ksi), ultimate tensile strength 551.6 MPa (80 ksi), Poisson’s ratio 0.3 and modulus elasticity 200 GPa (29000 ksi). The stress-strain curve of the steel which includes the elasticity stage and post-yield hardening stage is shown in **Figure 3.3**.

The three-dimensional frame element, which can consider the effects of biaxial bending, torsion, axial deformation and biaxial shear deformations, in SAP2000 is used for the simulation of the rail steels. The element sizes range from 305 mm to 457 mm (1 to 1.5 ft.) depending on the length of the member in the model.

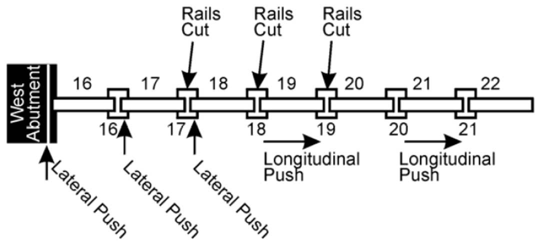

Figure 3.1 Plan View of Lateral Push Tests on Cincinnati Bridge (Uppal et al. 2000)

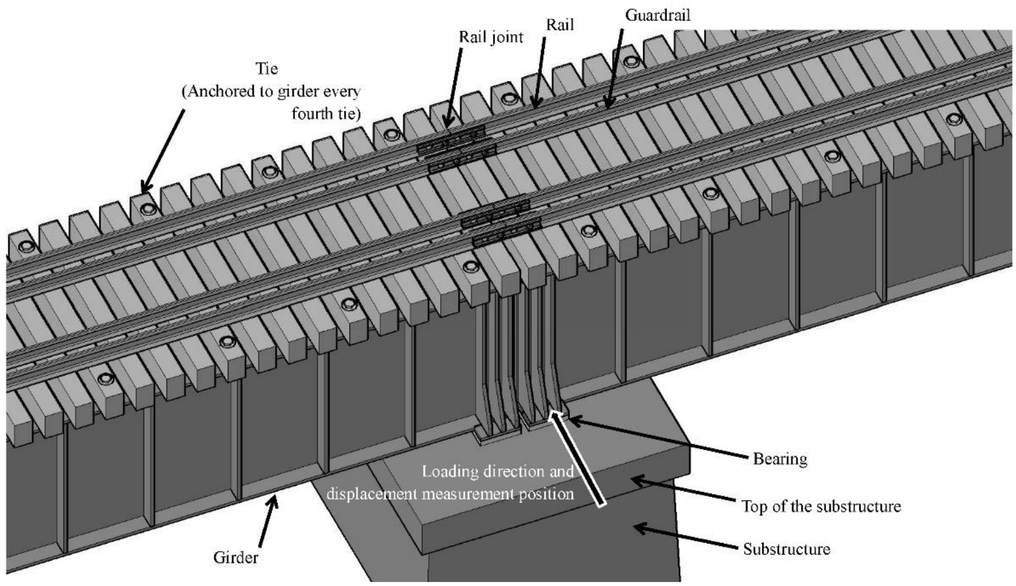

a) Physical bridge components

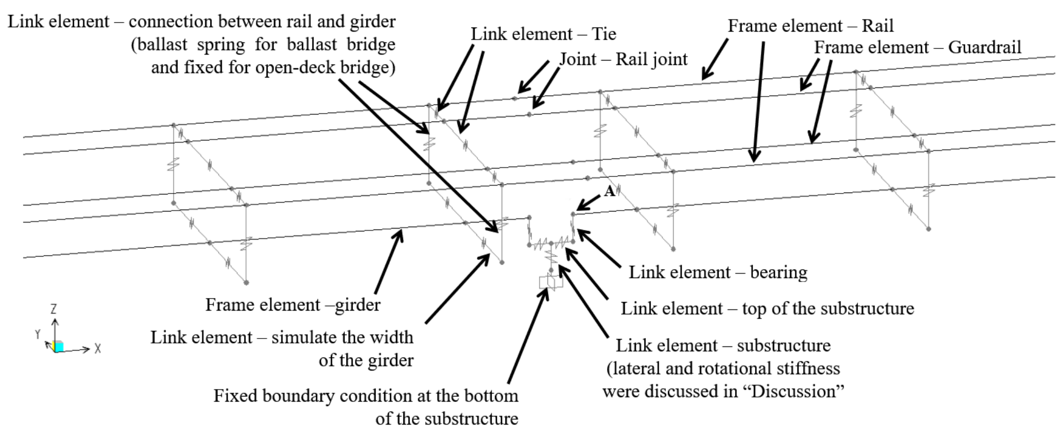

Joint A: The end of the girder, also the position of lateral loading and lateral displacement measurement.

b) SAP2000 model

Figure 3.2 Correlation between SAP2000 Model and Physical Bridge (Pier 16 of Cincinnati bridge)

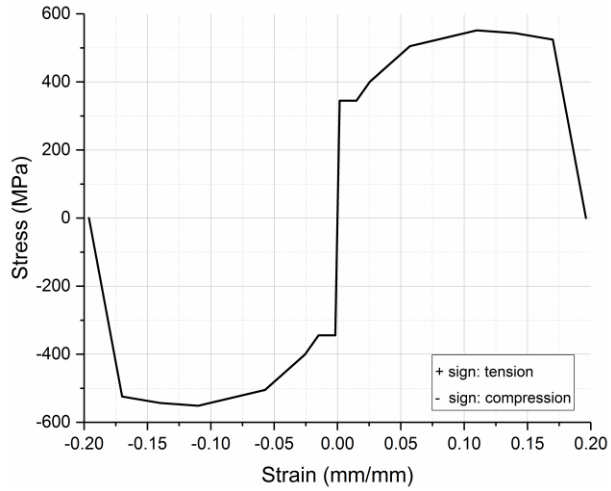

Figure 3.3 Constitutive Law of Rail Steel in Modeling

3.2.1.3 Rail joints

Due to the configuration of rail joints, physically they are only able to transfer a portion of the axial force and the moment between adjacent rail ends. However, few studies are available to indicate the range for this internal force transfer ratio of rail joints which is possibly due to the variation of the joint types for different rail sizes and the variation of joint fasten level. In this study, this release percentage in the model is calibrated by using the experimental load-displacement curves of the field testing. In the models, the rail joints of the rail track and the guardrail track are assumed to be located at the middle of adjacent bridge girder ends and transfer half of the axial force and the moment. This is realized in the models by releasing 50-percent of the fixity at the ends of adjacent frame elements connected by the rail joint.

3.2.1.4 Timber ties

The bridge used timber cross-ties with 203 mm (8 in.) wide by 303 mm (13 in.) deep on 356 mm (14 in.) centers. In the model, the spacing between two adjacent ties is 1.42 m (56 in.) to represent the rail being anchored to every fourth tie which have a regular 0.36 m (14 in.) spacing on the bridge deck.

The three-dimensional frame element is used to simulate timber ties. The element sizes range from 305 mm to 457 mm (1 to 1.5 ft.). The timber is an orthotropic material (Green et al. 1999) that has independent mechanical properties in the three perpendicular axes: longitudinal (parallel to the grain), radial (perpendicular to the grain in the radial direction) and tangential (perpendicular to the grain, tangent to the growth rings). The longitudinal direction corresponds to the length direction of the tie and local axis 1 in the model. The radial and tangential directions correspond to the local axes 2 and 3 of the local polar coordinate system in the model, respectively. Since the lateral pushing on the bridge girder is transferred to the rails through the timber ties, which are anchored to the bridge girder every fourth tie, the mechanical properties of the timber, at least in the length direction, needs to be considered. By considering the recommendations in the previous research (Ganesh Babu and Sujatha 2010, Green et al. 1999), the following material properties are employed in SAP2000 model: modulus of elasticity E_1=1378 ksi, E_2=137.8 ksi and E_3=68.9 ksi, Poisson's ratio u_{12}=0.35, u_{13}=0.38 and u_{23}=0.41, and shear modulus G_{12}=144 ksi, G_{13}=132 ksi and G_{23}=14 ksi where 1, 2 and 3 correspond to the numbers of local axes.

In the real bridge, the rails were fixed to the timber ties with tie plates and cut spikes. Since there is almost no relative translational or rotational movement between the rails and ties in the lateral direction, these connections are simulated as fixed connections in the model.

3.2.1.5 Ballast

The rail track and guardrail track were laid in ballast at the embankment zone off the end of the bridge. The resistance of the ballast to the rail-tie structure lateral displacement consists of the friction forces between the stone aggregate and the bottom and the two long sides surfaces of the ties, and the pressure the ballast provides against the front-end surface of the ties.

In the model, the restraint of the ballast against the lateral movement of the ties is modelled as a spring link between the ties and the embankment by using the link element in SAP2000. The spring stiffness of this link under lateral load is defined based on Kerr's (1980) study as shown in **Figure 3.4**. This ballast embankment zone is modelled as a length of 6.1 m (20-ft) off the end of the bridge to consider the influence of ballast resistance on the lateral movement of the rail track on the embankment.

3.2.1.6 Bridge girders

The steel deck-plate girders are modelled with corresponding cross-section properties and self-weight to represent the real structure. The three-dimensional frame element is used. The mesh size is 1.5 ft.

On the main spans, the track system was fixed to the bridge girder every fourth timber tie with hook bolts which restrict the translational and rotational movement of the ties from

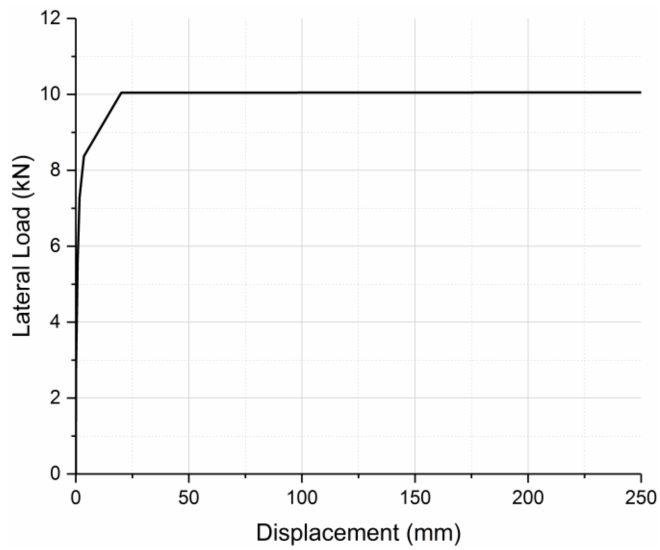

Figure 3.4 Stiffness of Ballast under Lateral Load in Modelling (after Kerr, 1980)

the beneath girder top flange. Thus, the connections between the track system and the bridge girder are simulated as fixed connections by using the rigid link element in SAP2000. These rigid link elements are connected to the bridge girder through the rigid link elements in the horizontal plane that simulate the width of the girder member.

3.2.1.7 Bearings

As stated in Uppal et al.'s report (2000), the girders rested on flat-plate bearings that were supported by concrete piers. The connection between each bearing and the pier consists of two anchor bolts with a nominal diameter of 38 mm (1.5-in.).

The bearings are modeled as spring links in the pushing direction between the girders and substructure by using the link element in SAP2000. The stiffness of these spring links is determined based on the testing at pier 17 in the report (Uppal et al. 2000). In the testing, the rail tracks were cut and be discontinuous at both ends of span 18. The span was pushed laterally at one end, pier 17. The pushing load versus the displacement of the girder end is shown in the upper part of **Figure 3.5**. The bearings on the pushing end were almost the only resistance to the lateral load except the small rotation resistance provided by the bearings on the other end, pier 18. Thus, in this study the stiffness of the spring link in the model is consistent with the force-displacement results in Uppal et al.'s testing, as shown in the lower part of **Figure 3.5**.

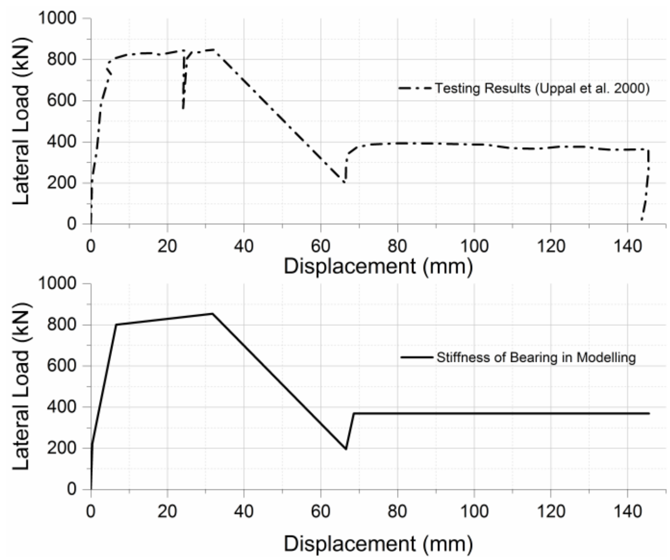

Figure 3.5 Stiffness of Bearing under Lateral Load in Testing and in Modelling for Cincinnati Bridge

3.2.1.8 Substructures

Piers 16, 17, 18 and the abutment provided support to the spans studied here. Based on Uppal et al.'s report (2000), the piers and the abutment have very short height and relatively large cross-section areas (shown in **Figure 3.6**). Thus, the substructures are modelled as rigid ground supports to the bearings on top. This is modeled in SAP2000 by using three link elements: a vertical one to simulate the substructure and two horizontal ones to simulate the width of the top of the substructure which connect to the link elements simulating the aforementioned bearings. The two horizontal link elements are rigid in all six degrees-of-freedom. The stiffnesses of the vertical link element in the six degrees-of-freedom are configured as fixed for this Cincinnati Bridge study. They are changed in the *Discussion* section where the influence of the stiffness of the substructure members on the bridge behavior is investigated.

3.2.2 Modelling for Maragakis et al. (2001) testing

3.2.2.1 Introduction of the testing and continuities of rail track along the bridge in the modelling

Maragakis et al. (2001) tested a railroad bridge with two simple-supported spans that was located in California (referred to as the California Bridge). The bridge consisted of a

Figure 3.6 Typical Pier Condition in Cincinnati Bridge (Uppal et al. 2000)

ballasted steel deck girder superstructure and a concrete two-column bent pier. As shown in **Figure 3.7**, the track structure of the west span, i.e. the rails, ties and ballast as well as the ballast pan, was cut completely free at the west abutment and the central pier. The east abutment was left in its as-built condition with the ties, rails, ballast, and ballast pan intact. The lateral force was applied to the bridge directly onto the lower portion of the girder at both abutments. Force-displacement diagrams were obtained at both ends of the bridge. The modelling consideration of the bridge system components and their connections is discussed below.

3.2.2.2 Rail track components and rail joints

AREMA standard rail with 168 kg/m (113 lb/ft) unit weight and Grade 50 steel was used as the rail track in the California Bridge. There is no guardrail for this ballasted bridge. The material properties of the rail steel in the model are the same with the Cincinnati Bridge model. The model configuration for the ties and the ballast are the same as the Cincinnati Bridge model. The rail joints are assumed to be located at the middle between the bridge girder ends and their adjacent abutments. The model configuration of the partial fixity release at rail joints is the same as the Cincinnati bridge model.

3.2.2.3 Bearings

The ballasted girder spans were supported by high seat type steel rocker bearings. The bearings are again modeled as a spring link that provides a lateral connection between the girder and the pier by using the link element in SAP2000. The spring stiffness of this connection is modeled with a nonlinear force-displacement curve based on the testing results of the west span in Maragakis et al. (2001). The load-displacement curves that were obtained in the testing as well as used in the model are shown in **Figure 3.8**.

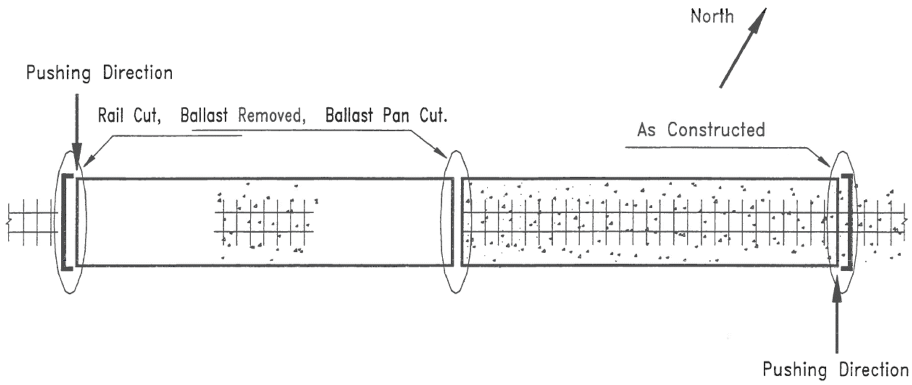

Figure 3.7 Plan-view Layout of Lateral Push Tests of California Bridge (Maragakis et al. 2001)

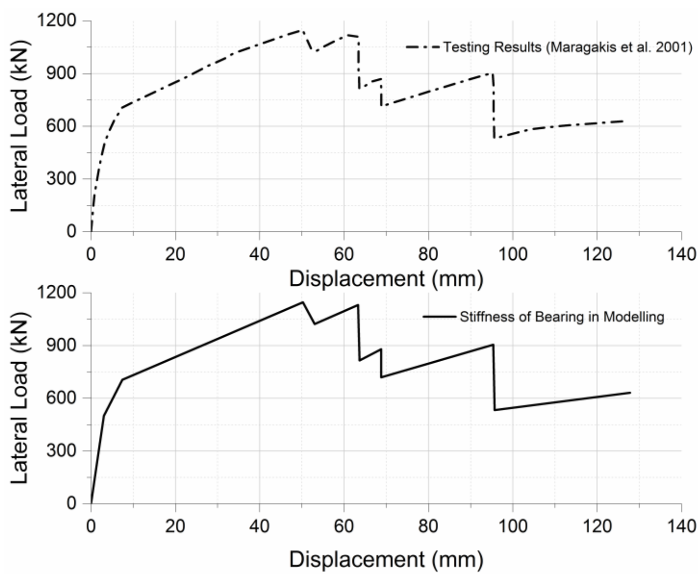

Figure 3.8 Stiffness of Bearing under Lateral Load in Testing and in Modelling for California Bridge

3.2.2.4 Substructures

The bridge girders were supported on two abutments and one center concrete pier. The abutments are modelled as rigid ground supports to the superstructure. The center pier was modeled as a plain concrete continuum with a compressive strength of 4000 psi by using frame element in SAP2000. The modulus of elasticity was 24.9 GPa (3605 ksi) (ACI 2014), Poisson's ratio 0.2, and a nonlinear stress-strain curve for unconfined concrete (Mander et al. 1988; Computers & Structures Inc. 2016) were used as shown in **Figure 3.9**. The three-dimensional frame element in SAP2000 is used and the element size is 0.84 m (2.76 ft.) for this 7 m (23 ft.)-high pier.

3.3 Results and model verification

3.3.1 Natural frequencies and modal analysis

A modal analysis was conducted for the California bridge model in SAP2000. The first three natural frequencies and mode types of SAP2000 analysis and the experimental results for the rail intact and rail cut cases are tabulated in **Table 3.1**. The fundamental frequencies in numerical analysis for the rail intact and rail cut cases is 5.39 Hz and 5.25 Hz. Both are in transverse direction. The second and third natural frequencies for rail intact case in SAP2000 are 7.55 Hz and 8.74 Hz. They are in vertical direction and longitudinal direction respectively. For rail cut case, the second and third natural frequencies in SAP2000 are 6.74 Hz and 7.71 Hz. They are also in vertical direction and longitudinal direction respectively.

By comparing with the experimental results, the fundamental frequencies of the

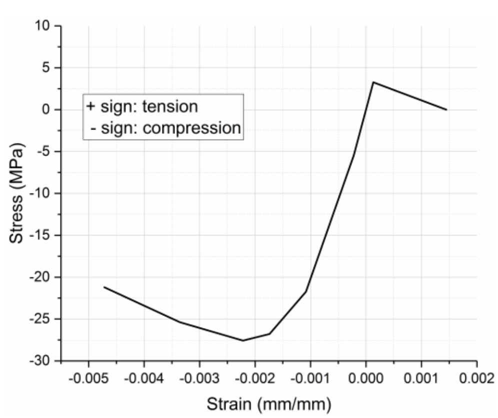

Figure 3.9**.** Constitutive Law of Plain Concrete in Modeling

Table 3.1 Frequencies and Mode Types of First Three Vibration Modals

Modal Number	Numerical Results		Experimental Results (Maragakis et al. 1998)	
	Natural Frequency (cycle/sec.)	Mode Type	Natural Frequency (cycle/sec.)	Mode Type
1	5.39 (5.25)	Transverse	4.93 (4.80)	Transverse
2	7.55 (6.74)	Vertical	6.06 (5.55)	Vertical
3	8.74 (7.71)	Longitudinal	6.56 (5.95)	Longitudinal

Note: Numbers without and with parentheses are results of rail intact and rail cut cases respectively.

numerical analysis are 9.3% and 9.4% higher than the testing results for rail intact and rail cut cases respectively. The differences between the model analysis and testing results increase for the second and third natural frequencies. Since the transverse, or lateral, direction is the research objective in this study which is identical with the fundamental frequency direction, it would be reasonable to use the proposed model scheme for the following nonlinear static loading study in the lateral direction.

3.3.2 Load-displacement curve

Nonlinear static analyses, using the nonlinear material constitutive law for the steel and concrete and the nonlinear spring link element for the bearings and ballast, were implemented in SAP2000 (Computers & Structures Inc. 2016) to simulate the behavior of the bridge structures under lateral pushing load at span ends in the experiments. In the analyses, the lateral load was directly applied at the span end of the superstructure girder to align with the configuration in the field testing. Both the force-load and the displacement-load can be applied in SAP2000. In this study, the force-load method was used for the ascending portion in order to capture the initial portion of the load-displacement curve which has relative high stiffness. The force load was increased gradually with an increment of 222.4 kN (50 kips) until approaching the ultimate load where the increment was decreased to 44.5 kN (10 kips) or 4.45 kN (1 kip). The ultimate load is defined as the force load just before the condition of non-convergence in the SAP2000 model. This non-convergence may be caused by the non-injective characteristic, one ordinate value has more than one corresponding abscissa value on the curve, of the nonlinear load-displacement property for the link element of bearings and ballast and the nonlinear constitutive law of the steel material corresponding to the post-peak, or downward, part of the curve. The post-ultimate portion of the load-displacement curve is obtained by applying the displacement-load. The increment of displacement-load is 2.54 mm (0.1 in.).

3.3.2.1 Span 16 at abutment of Cincinnati Bridge

The rail track structure is continuous at both ends for this span. One end is connected to the ballasted embankment, and the other end is connected to adjacent span 17, as shown in **Figure 3.1**. The results of load versus lateral displacement are plotted as a dashed line with triangle markers in **Figure 3.10**. The curves show nonlinear characteristics due to primarily the nonlinear property of the links. From 0 to 890 kN (200 kips, point A in **Figure 3.10**), the curve consists of two portions with the slope decreasing at 222.4 kN (50 kips). The secant stiffness before 890 kN (200 kips) reaches 147 kN/mm (839 kip/in.). After 890 kN (200 kips) the stiffness drops significantly. The ultimate load is 1010 kN (227 kips) at a displacement of 31.3 mm (1.23 in.). By comparison span 18 @pier 17 which had rail discontinuous at both span ends (the diamond marker in **Figure 3.10**) has a secant stiffness of 121 kN/mm (692 kip/in.) at yield point B in **Figure 3.10** and an ultimate load of 854 kN (192 kips). This indicates for open-deck bridges the continuous rail track structure benefits the bridge system in terms of the ultimate lateral pushing resistance and the secant stiffness before yielding (yielding is defined at the point after it the displacement increases rapidly in this study). This coincides with the conclusions of Otter et al (1999b)'s study.

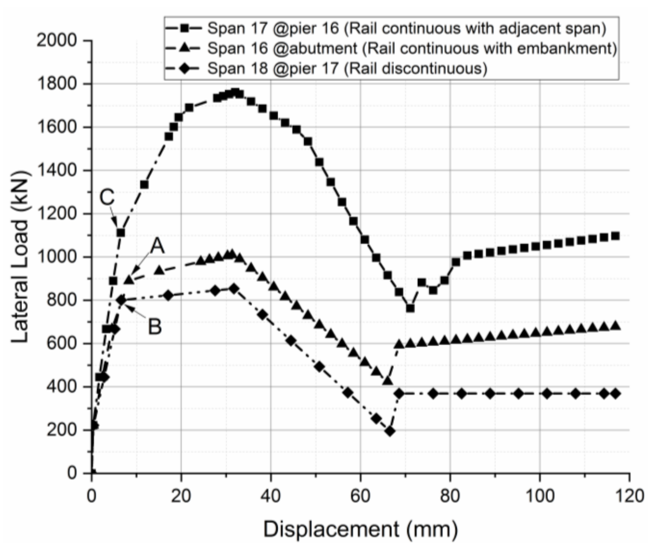

Figure 3.10 Load vs. Displacement of Modelling Results (Cincinnati Bridge)

The results of model analysis and experiment are compared in **Figure 3.11**. The model results match the experimental results on the ascending portion, especially in the initial part before 889.6 kN (200 kips). The modeling results have a larger ultimate load and corresponding displacement than the testing results. This may be caused by the over-estimation of the bearing lateral capacity in the model due to the difference of deterioration level of bearing-pier connection between different spans which will be discussed later.

3.3.2.2 Span 17 at pier 16 of Cincinnati Bridge

Referring to **Figure 3.1**, one end of span 17 was continuous to the adjacent span 16 while at the other end, the rails and guiderails were cut and discontinuous with adjacent span 18. The pairs of lateral pushing load and corresponding displacement results are plotted with the square marker line in **Figure 3.10**. The curve shows nonlinearity due to primarily the nonlinear property of the link elements. Similar to the results of span 16, from 0 to 1112 kN (250 kips, point C in **Figure 3.10**), the curve consists of two portions of linear increase with slope deceasing after 222.4 kN (50 kips). From 1112 kN (250 kips) to the ultimate load of 1761 kN (396 kips), the lateral displacement of bridge system increases severely as the pushing load increases. The secant stiffness at 1112 kN (250 kips) is 171 kN/mm (976 kip/in.) which is larger than the secant stiffness of 121 kN/mm (692 kip/in.) for span 18 @pier 17 which had rail discontinuous at both span ends (referring to the diamond marker line in **Figure 3.10**). This shows the contribution of the

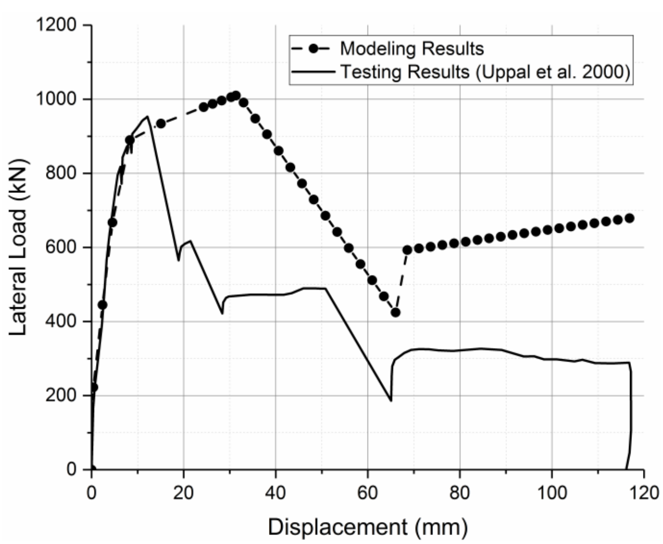

Figure 3.11 Comparison of Experimental and Modelling Results (Span 16 @abutment, Cincinnati Bridge)

rail track on the lateral pushing resistance both in ultimate load and secant stiffness before yielding that coincides with the findings in Otter et al (1999b).

The modeling and testing results are compared in **Figure 3.12**. It is noted that in the experiment the lateral loading had to stop at 1357 kN (305 kips), referring to the peak point at about 30.5 mm (1.2 in.) displacement in **Figure 3.12**, because of the "incipient failure of the deteriorated surface concrete of the pier" reported in Otter et al.'s report (1999b). At that time, the anchor bolts of the bearing and the span were in good condition and should be able to provide more lateral resistant capacity. This does not coincide with the assumption of rigid substructure in the aforementioned modeling analysis. However, the testing result curve also consists of two portions before "ultimate state". The load at yield point, about 1023 kN (230 kips), is close to the model result 1112 kN (250 kips).

3.3.2.3 East Span at abutment of California Bridge

For the east span of the California Bridge, the rail track structure was intact at the connection between the east span, with ballast track, and the ballast embankment. Similar SAP2000 analysis and loading pattern with the Cincinnati Bridge are implemented. The load versus displacement results are plotted in dot-dash line with box markers in **Figure 3.13**. The yield point is around 667 kN (150 kips). The secant stiffness at 667 kN (150 kips) is 143 kN/mm (817 kip/in.) compared with the secant stiffness of 102 kN/mm (583 kip/in.) for the west span which has rail discontinuously (as shown in dash line in **Figure 3.11**). The lateral displacement rapidly increases as the pushing load increases. The

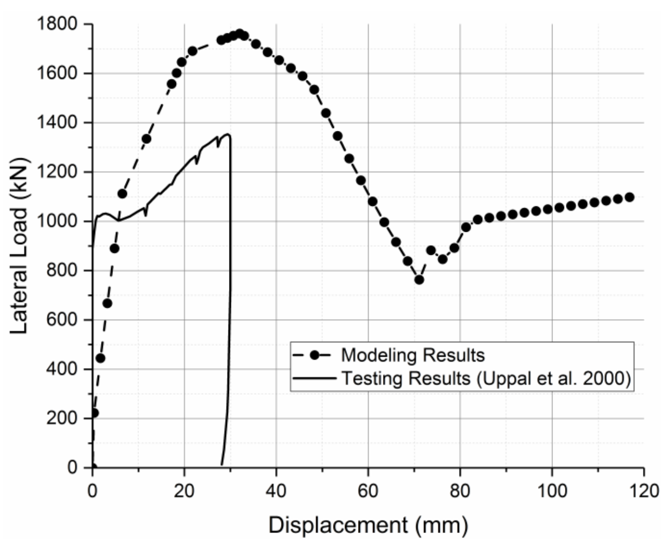

Figure 3.12 Comparison of Experimental and Modelling Results (Span 17 @pier 16, Cincinnati Bridge)

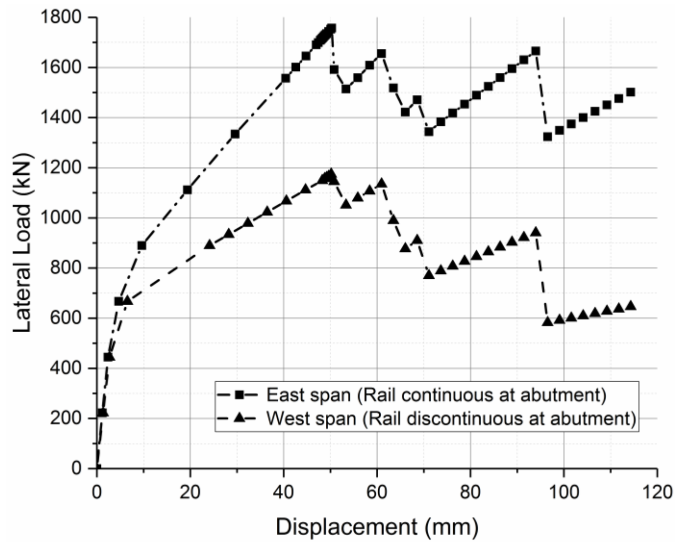

Figure 3.13 Load vs. Displacement of Modelling Results (California Bridge)

ultimate load is 1757 kN (395 kips) at a lateral displacement of 50.3 mm (1.98 in), while the ultimate capacity of the west span is 1174 kN (264 kip) at a displacement of 50.3 mm (1.98 in.). It indicates that for the ballasted bridge the rail track structure provides contribution to the secant stiffness before yield and ultimate resistance to the lateral pushing load, which coincides with the findings by Maragakis et al (2001).

The model results and experimental data are compared in **Figure 3.14**. The model results provide a reasonable prediction to the experiment before the ultimate state in the testing. The modeling has a relatively higher ultimate capacity than the testing result. This may be caused by the over-estimation on the bearing capability in the model due to the variation of the deterioration of bearings and their connections with the substructure.

3.4 Discussion

In the aforementioned modelling analysis for Cincinnati Bridge, a rigid substructure is assumed which means infinite stiffness in displacement and rotation for the substructure. This assumption can be appropriate for a very short substructure, like the piers in the Cincinnati Bridge (**Figure 3.7**). However, it may not be appropriate to represent the behavior of bridges with taller piers.

A parametric analysis of the Cincinnati Bridge was carried out to determine the influence of the lateral and rotational substructure stiffness on the displacement behavior of the bridge, stress level in rail and failure modes under ultimate lateral loading. The

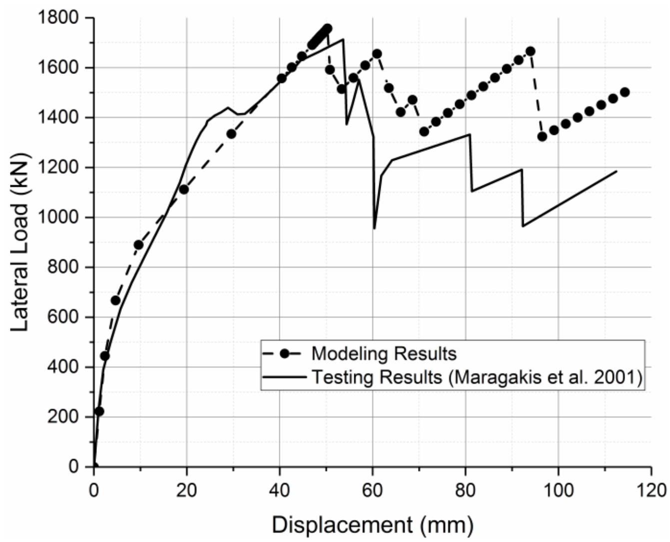

Figure 3.14 Comparison of Experimental and Modelling Results (East span, California Bridge)

parametric study focuses on the ascending portion of the load-displacement curve, especially the secant stiffness, and the post-ultimate portion of the curve is not examined.

3.4.1 Influence of Lateral Stiffness of Substructure

3.4.1.1 Open-deck Girder Bridge

In order to explore the influence of the lateral stiffness of the substructure on the behavior of an open-deck girder bridge with continuous rail structure under lateral load at the end of the span, the lateral deformation stiffness of the "Link" element that simulates the substructure in SAP2000 model was varied from infinite (the same model for Span 17 of Cincinnati Bridge aforementioned) to 175 kN/mm (1000 kip/in.), 87.6 kN/mm (500 kip/in.), 35.0 kN/mm (200 kip/in.) and 17.5 kN/mm (100 kip/in.). The behavior of lateral load versus displacement at the end of span and the stress level in rail under different levels of pier lateral stiffness are plotted in **Figure 3.15** and **Figure 3.16** respectively. The influence of the lateral stiffness of substructure on the secant stiffness of the bridge system is tabulated in **Table 3.2** and illustrated in **Figure 3.17**. The secant stiffness is defined as the slope of the straight line between original point and the yield point in the load-displacement figures.

As shown in **Figure 3.15** and **Table 3.2**, as the pier stiffness decreases from infinite to 17.5 kN/mm (100 kip/in.), the secant stiffness of the bridge system decreases. This implies that at the initial phase of loading before system yielding, the lateral stiffness of

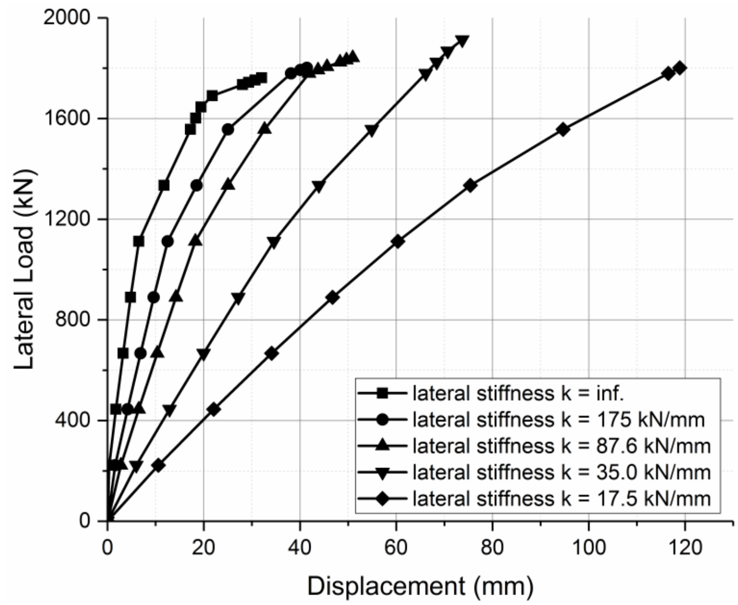

Figure 3.15 Influence of Lateral Stiffness of Substructure on Load vs. Displacement (open-deck bridge)

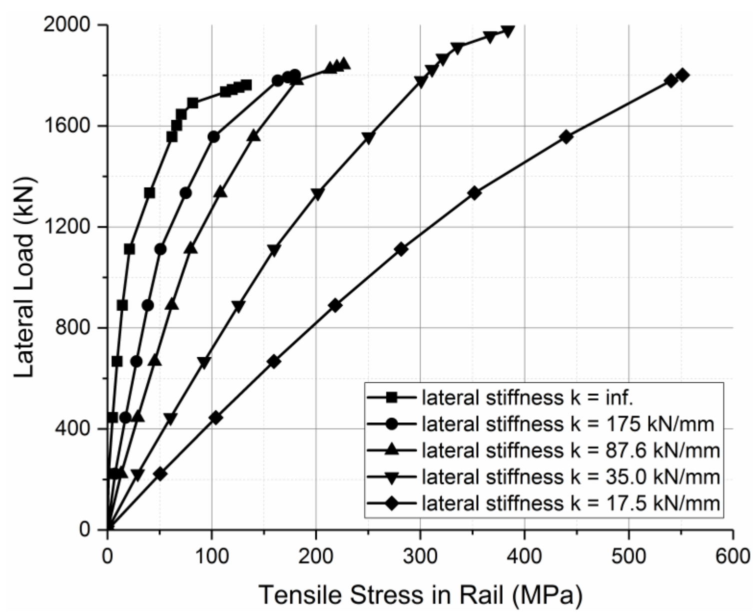

Figure 3.16 Influence of Lateral Stiffness of Substructure on Tensile Stress in Rail (open-deck bridge)

Table 3.2 Influence of Substructure Lateral Stiffness on System Secant Stiffness for Open-deck Bridge Models

Lateral Stiffness of Substructure (kN/mm)	infinite	175	87.6	35.0	17.5
Secant Stiffness of Bridge System (kN/mm)	171	89.0	60.9	32.2	17.7

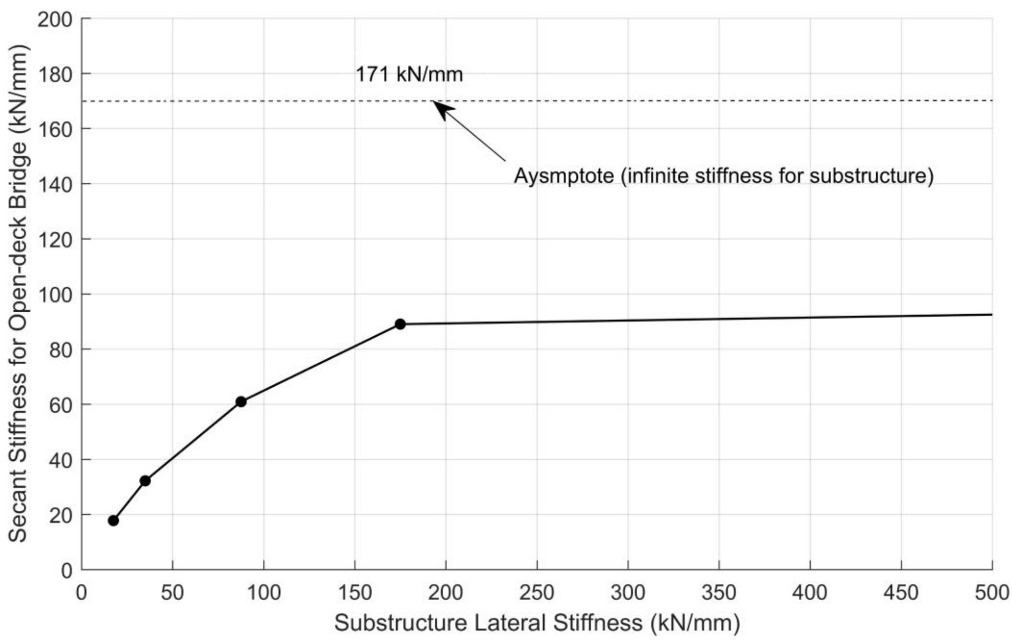

Figure 3.17 Relationship between Substructure Lateral Stiffness and Secant Stiffness for Open-deck Bridge System

the substructure plays an important role in the performance of the bridge system.

Figure 3.16 shows that the stress level in the rail steel increases with the decrease of the lateral stiffness of the substructure. It indicates that the rail picks up more of the load as the pier stiffness decreases. The model with the smallest pier stiffness fails by the failure of rail steel (the tensile stress reaches the ultimate stress of 551 MPa).

Figure 3.18 shows that as the lateral stiffness of the substructure decreases most of the total lateral displacement changes from being the local displacement of bearings to the lateral displacement of the substructure. The failure of the bridge system is governed by the bearing capacity for a stiffer substructure and by the rail steel failure for a substructure with less lateral stiffness.

3.4.1.2 Ballast Bridge

Similar to the analysis for the open-deck girder bridge, a parametric study is performed for the ballasted deck bridge. The model for Span 17 of the Cincinnati Bridge was used and the load-displacement property of the Link element between rail and girder was changed to the one shown in **Figure 3.4** that was used to simulate the lateral displacement behavior of the ballasted structure. The analytic results are plotted in **Figure 3.19** and Figure **3.20** to show the influence of the lateral stiffness of the substructure on the load-displacement behavior of bridge structure and the stress level within the rail steel respectively. The influence of the lateral stiffness of substructure on the secant stiffness of the bridge system is tabulated in **Table 3.3** and illustrated in **Figure 3.21**.

Above a load of 890 kN (200 kips), the stiffness of the structure is similar and mostly independent of the substructure stiffness. The behavior of each model at ultimate load is controlled by the lateral displacement capacity of the bearing while independent of the lateral stiffness of the pier. This is verified by **Figure 3.22** in which the relative displacement between the top of bearing and the top of substructure for models reaches 31.8 mm (1.25 in.) which identities the maximum lateral displacement capacity of bearing. As shown in **Figure 3.20**, none of the rail steel in the models reaches the ultimate tensile stress. This can be explained by the ballast between the rail track structure and bridge girder. The ballast does not transfer much of the displacement from the bridge girder and the bearing to the track structure. The rail track structure is able to “float” on the ballast and has smaller lateral displacement and smaller stress level during lateral loading in comparison with open-deck bridges.

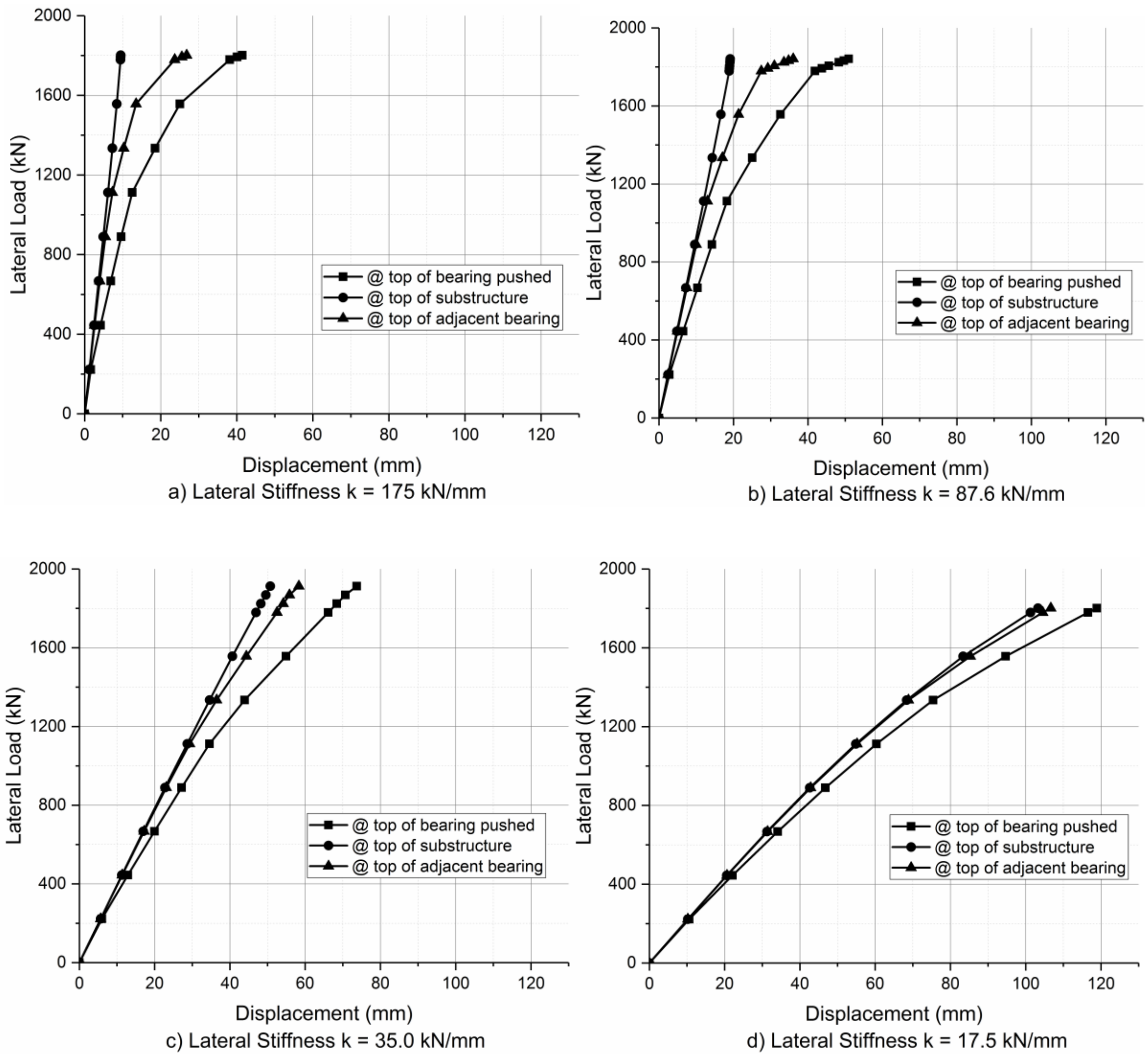

Figure 3.18 Influence of Lateral Stiffness of Substructure on Displacement at Different Position (Open-deck Bridge)

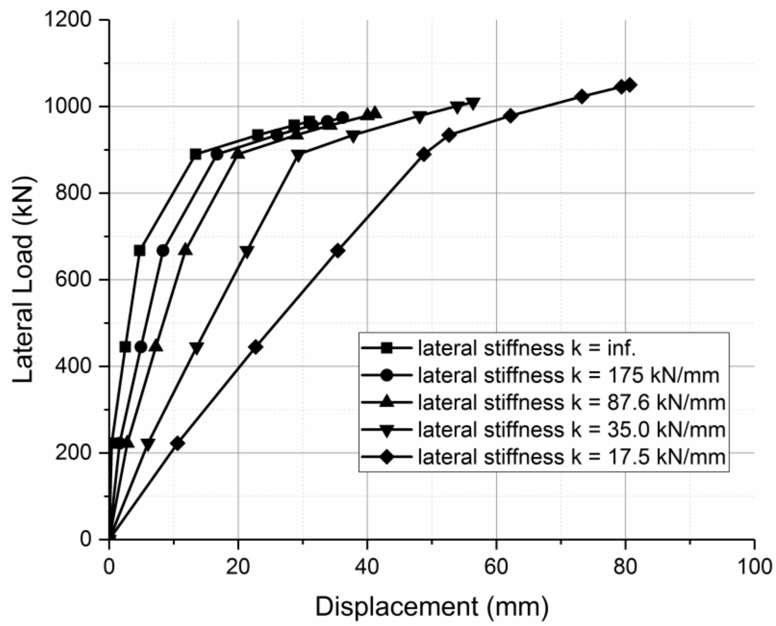

Figure 3.19 Influence of Lateral Stiffness of Substructure on Load vs. Displacement (ballast bridge)

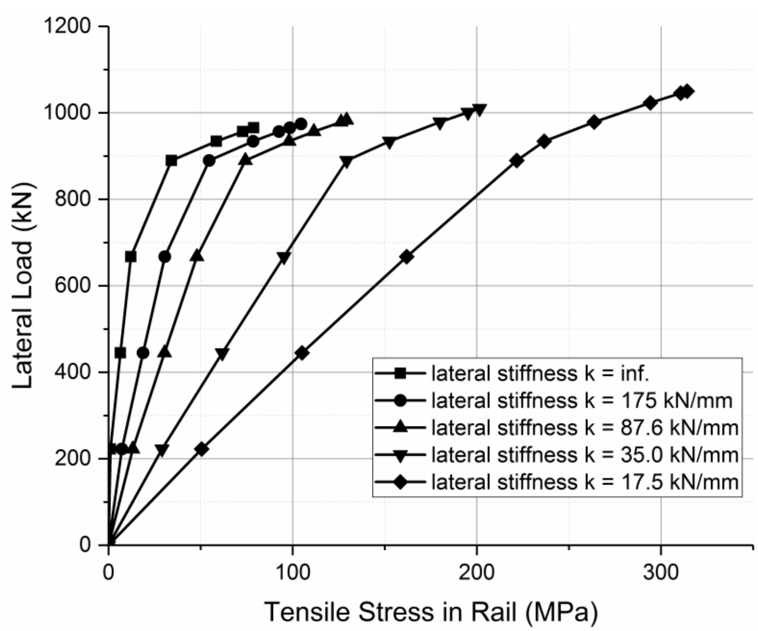

Figure 3.20 Influence of Lateral Stiffness of Substructure on Tensile Stress in Rail (ballast bridge)

Table 3.3 Influence of Substructure Lateral Stiffness on System Secant Stiffness for Ballast Bridge Models

Lateral Stiffness of Substructure (kN/mm)	infinite	175	87.6	35.0	17.5
Secant Stiffness of Bridge System (kN/mm)	141	79.9	56.5	31.2	18.8

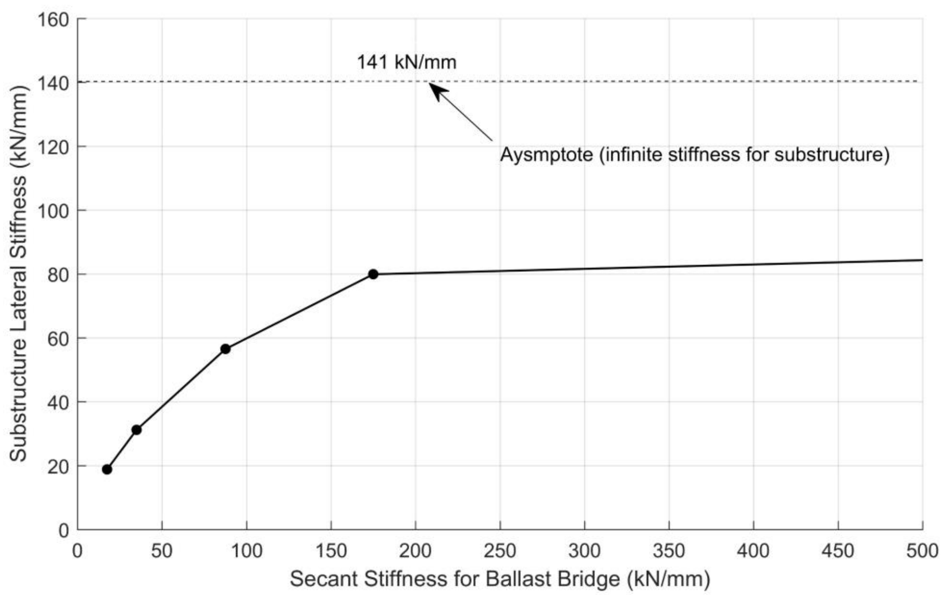

Figure 3.21 Relationship between Substructure Lateral Stiffness and Secant Stiffness for Ballast Bridge System

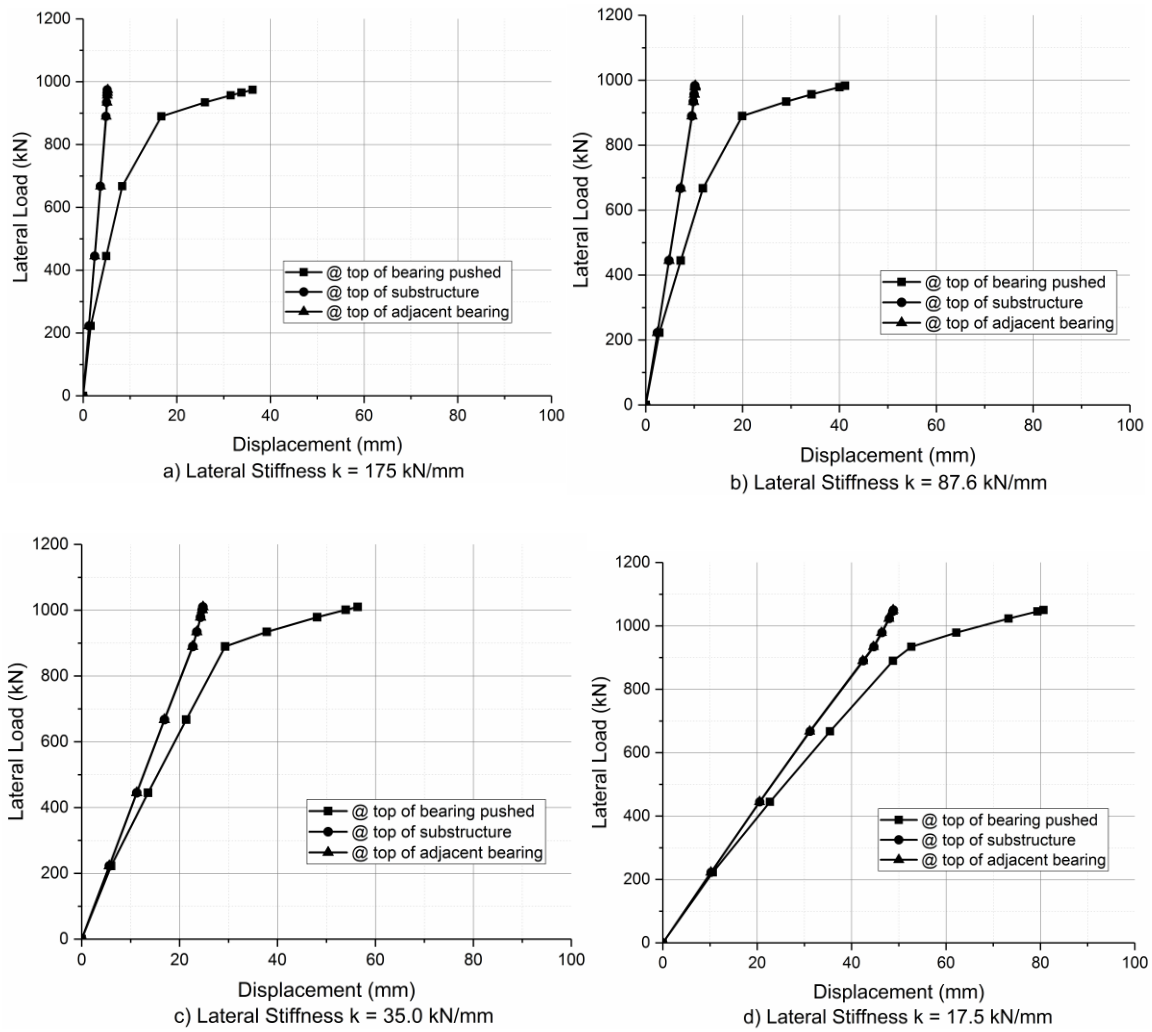

Figure 3.22 Influence of Lateral Stiffness of Substructure on Displacement at Different Position (Ballast Bridge)

3.4.2 Influence of Rotational Stiffness of Substructure

3.4.2.1 Open-deck Girder Bridge

The torsional, as shown in **Figure 3.23**, stiffness of substructure may have influence on the displacement performance of a bridge under lateral loading. Based on the model of

Span 17 of the Cincinnati Bridge, a parametric study was performed with the torsional stiffness of the substructure varied from infinite to 565 kN-m/rad (5000 kip-in./rad) and 226 kN-m/rad (2000 kip-in./rad). The results for the load-displacement at the end of span and load-stress in rail are plotted in **Figure 3.24** and **Figure 3.25**. The influence of the rotational stiffness of substructure on the secant stiffness of the bridge system is tabulated in **Table 3.4** and illustrated in **Figure 3.26**.

As shown in **Figure 3.24** and **Table 3.4**, the change of rotational stiffness has almost no impact on the stiffness of the bridge. The stress in the rail steel is only about 20% of the ultimate strength of 552 MPa. On the other hand, the failure of the models is all due to excessive displacement, reaching the maximum displacement at the ultimate load for bearing 31.8 mm (1.25 in.), **Figure 3.27**. Also, in the same figure, the rotation of the pier top causes the bearings at the same pier to move in the opposite direction (yield negative in displacement in **Figure 3.27**). As long as the load increases, these two bearings turn to move in the same direction with load due to the existence of rail track structure.

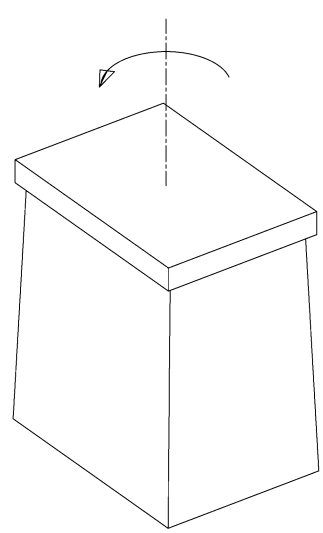

Figure 3.23 Torsion with Respect to Pier Centerline Axis

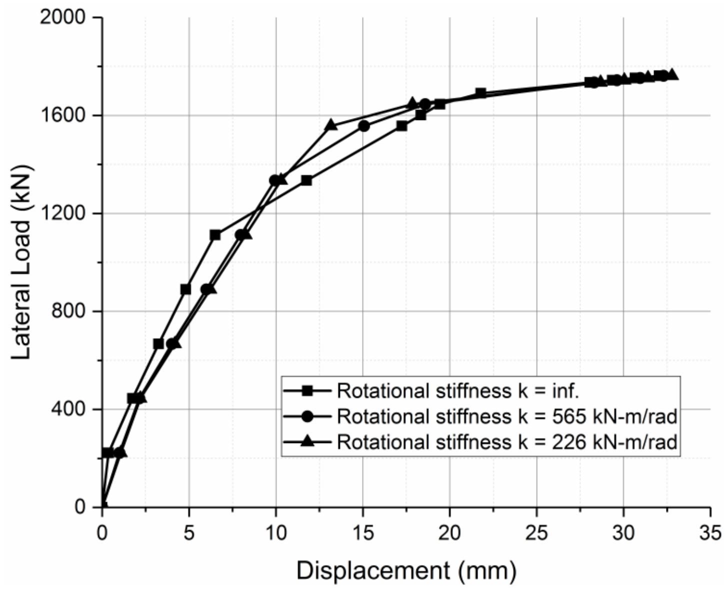

Figure 3.24 Influence of Torsional Stiffness of Substructure on Load vs. Displacement (open-deck bridge)

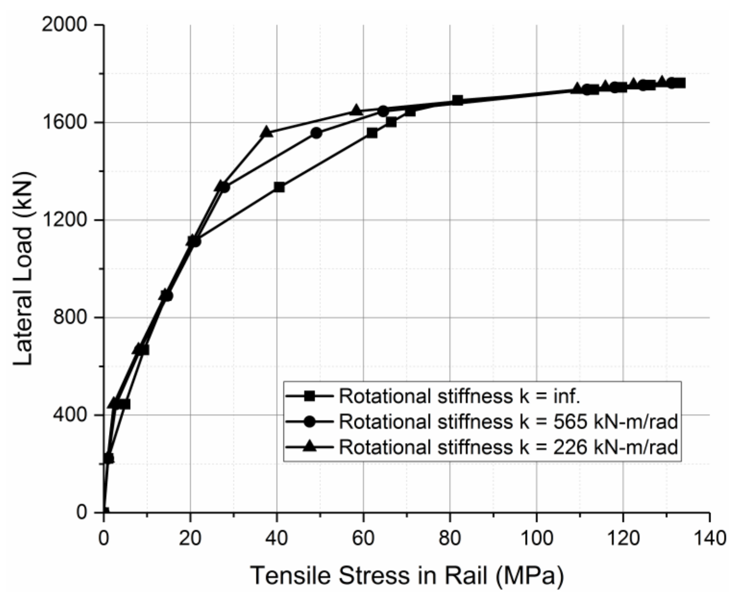

Figure 3.25 Influence of Torsional Stiffness of Substructure on Tensile Stress in Rail (open-deck bridge)

Table 3.4 Influence of Substructure Rotational Stiffness on System Secant Stiffness for Open-deck Bridge Models

Torsional Stiffness of Substructure (kN-m/rad.)	infinite	565	226
Secant Stiffness of Bridge System (kN/mm)	171	140	135

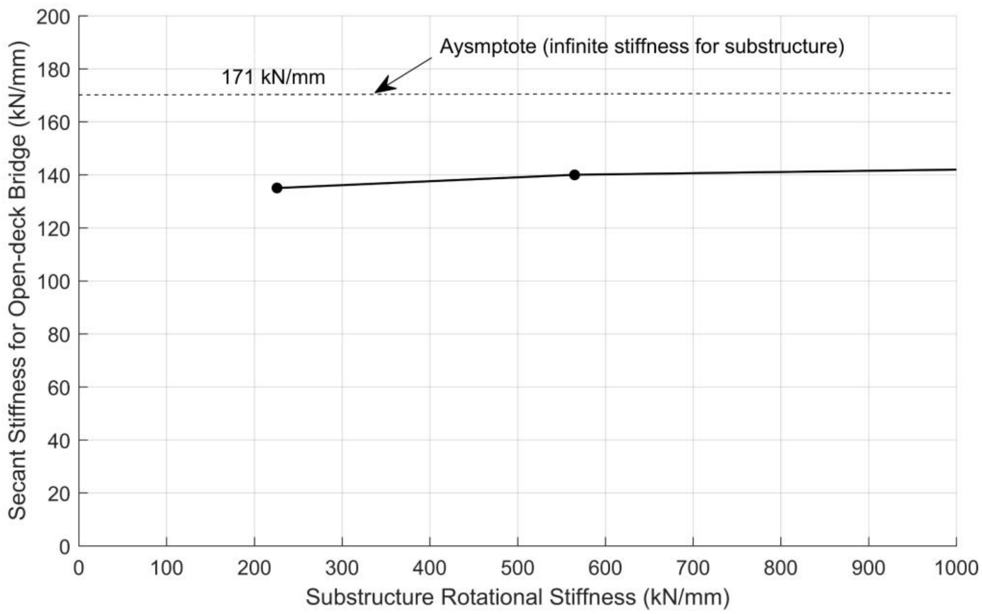

Figure 3.26 Relationship between Substructure Rotational Stiffness and Secant Stiffness for Open-deck Bridge System

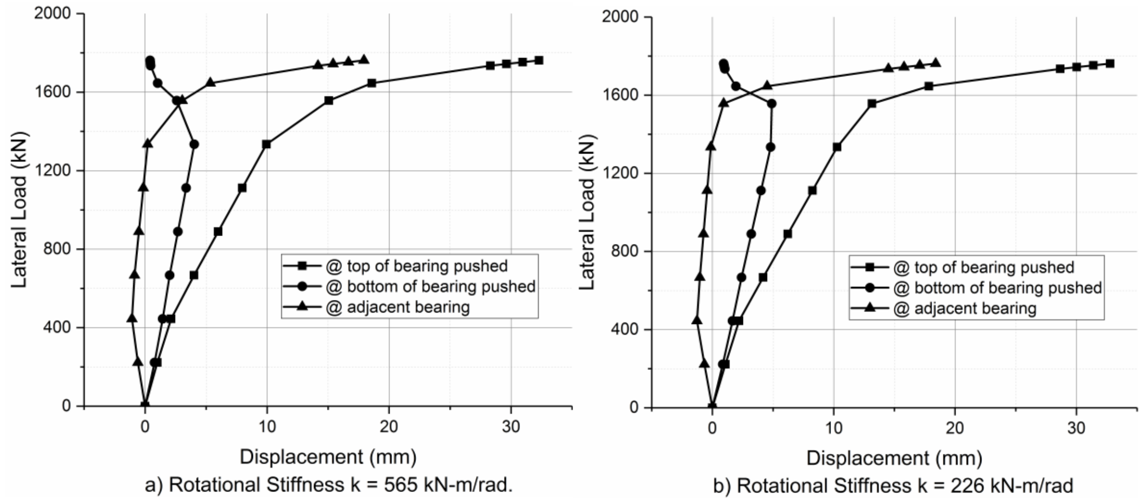

Figure 3.27 Influence of Rotational Stiffness of Substructure on Displacement at Different Position (Open-deck Bridge)

3.4.2.2 Ballast Bridge

A similar parametric study is carried out on the influence of torsional stiffness of substructure for ballast bridges. The torsional stiffness varied from infinite to 565 kN-m/rad (5000 kip-in./rad) and then 226 kN-m/rad (2000 kip-in./rad). The results of load-displacement and load-tensile stress level in rail are plotted in **Figure 3.28** and **Figure 3.29**. The influence of the rotational stiffness of substructure on the secant stiffness of the bridge system is tabulated in **Table 3.5** and illustrated in **Figure 3.30**.

Based on **Figure 3.28**, **Figure 3.29** and **Table 3.5**, it is found that the pier torsional stiffness affects the lateral stiffness of the bridge structure, its ultimate load and corresponding displacement at ultimate load. As the rotational stiffness of substructure decreases, the lateral stiffness of the bridge structure system decreases, meanwhile the ultimate load and the corresponding displacement at ultimate load increases. From **Figure 3.31**, the structure reaches its ultimate due to the excessive lateral deformation, over 30.8 mm (1.25 in.) (referring the peak in **Figure 3.5**), of the bearing. These phenomena can be explained by the existence of ballast between the rail track and bridge girder. The ballast tranfers little of the pier displacement to the rail track on the top. Thus, no excessive tensile force is generated in the rail track with the increase of lateral load on the bearing. The majority of the lateral displacement of the bridge system comes from the rotation of the pier top. The rail contributed little to the lateral stiffness and capacity of the bridge.

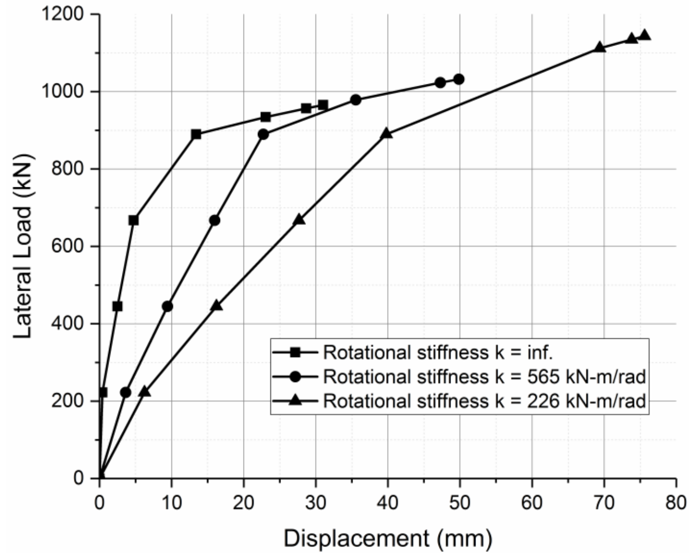

Figure 3.28 Influence of Torsional Stiffness of Substructure on Load vs. Displacement (ballast bridge)

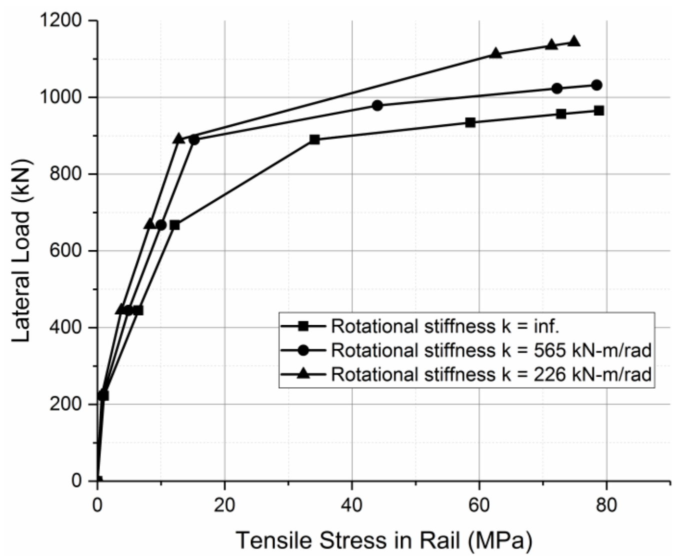

Figure 3.29 Influence of Torsional Stiffness of Substructure on Tensile Stress in Rail (ballast bridge)

Table 3.5 Influence of Substructure Rotational Stiffness on System Secant Stiffness for Ballast Bridge Models

Torsional Stiffness of Substructure (kN-m/rad.)	infinite	565	226
Secant Stiffness of Bridge System (kN/mm)	141	41.7	24.1

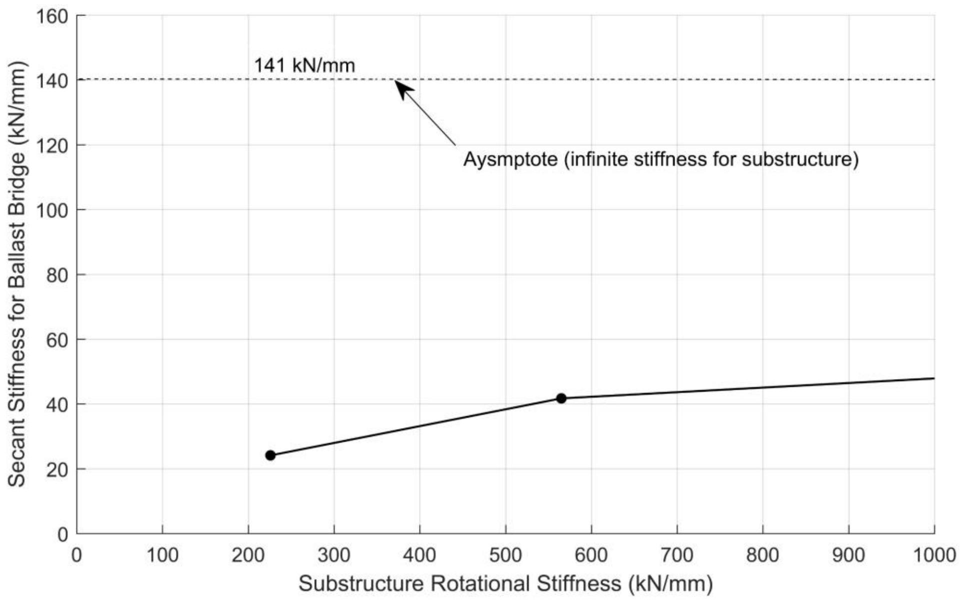

Figure 3.30 Relationship between Substructure Rotational Stiffness and Secant Stiffness for Ballast Bridge System

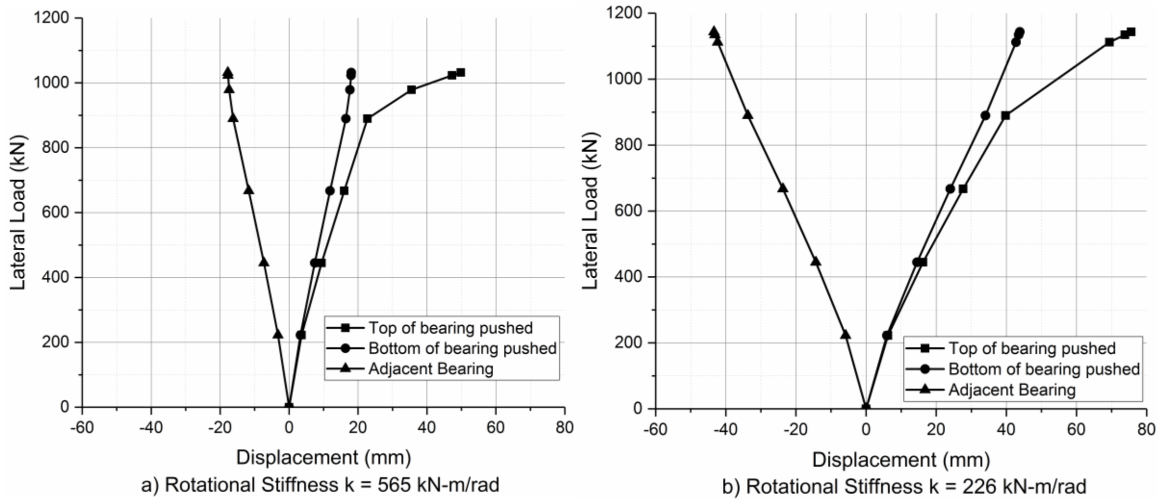

Figure 3.31 Influence of Rotational Stiffness of Substructure on Displacement at Different Position (Ballast Bridge)

3.5 Conclusions

In order to find out the influence of the rail track on the lateral behavior of a railroad bridge system under lateral load at the end of span, a nonlinear three-dimensional model analyses for both the ballast bridge and the open-deck girder bridge are implemented in SAP2000 and validated based with the experimental research reported in the literature. Several conclusions are drawn below:

(1) The SAP2000 model scheme proposed in this study by using the link element to simulate the behavior of bearings and ballast reaches a reasonable agreement with the previous full-scale field experimental results on both open-deck and ballast railroad bridges regarding the fundamental frequency and mode type and the force-displacement behavior before the ultimate state.

(2) For the open-deck girder bridge model, the secant stiffness of the bridge system increases with the increase of the lateral stiffness of substructure. The model with a higher pier stiffness has a smaller ultimate displacement. It is found that the failure of the bridge system is governed by the bearing capacity for a stiffer substructure and by the rail steel failure for a substructure with less lateral stiffness.

(3) For open-deck bridges the rotational stiffness of the substructure has little impact on the secant lateral stiffness of the bridge system. The stress of rail steel remains at a low level. The cause of ultimate state is the excessive bearing deformation.

(4) For ballast bridges, the secant stiffness of the bridge system increases when the lateral stiffness of substructure increases. Due to the existence of ballast between the rail track and bridge girder, the lateral displacement and tensile stress of the rail steel remain small. The bridge system reaches the ultimate state when the bearing reaches the lateral displacement capacity.

(5) For ballast bridge models, as the rotational stiffness of substructure decreases, the secant lateral stiffness of bridge structure system also decreases. Meanwhile the ultimate load and corresponding system lateral displacement at ultimate state increases. The bridge system reaches the ultimate due to the excessive lateral deformation of the bearing.

(6) A range of secant stiffness for both open-deck and ballasted bridges with rail intact between each span under lateral pushing load are obtained. A further study to investigate the seismic performance of the substructure will be conducted by simplifying the restraining effect of the rail track structure as a spring with a range of stiffness identified in this study.

Chapter 4:

Shaking Table Experiment Results and Discussion

4.1 Introduction

Housner (1963) initiated the research on the analytical solution of the rocking behavior of freestanding rigid blocks under various ground motions. Numerous additional studies examined the assumptions in Housner's research extended the research to include multiple modes (Ishiyama, 1982, Shenton, 1996), multiple bodies (Psycharis, 1990; Wittich and Hutchinson, 2017), three dimensions (Konstantinidis and Makris, 2007), flexibility of the body and interface (Chatzis and Smyth, 2011).

However, little research has been conducted on the dynamic behavior of a rigid body with horizontal restraint. The only research that was found was conducted by Giresini and Sassu (2017). The study focused on the dynamic behavior of horizontally restrained blocks which represent masonry/concrete wall façades subjected to out-of-plane constraints (e.g. flexible roof/floor, perpendicular wall panel, and an anti-overturn retrofit device). The major contribution is the extension of the conventional knowledge on the rocking behavior of freestanding rigid blocks with consideration of horizontally restraining boundary conditions. However, the paper only considered the pure rocking behavior of slender blocks (height/thickness > 5) and ignored other possible modes, such as sliding and rocking-sliding, which would be applicable for non-slender blocks such as bridge piers. The paper also only considered single-body motion and ignored the possibility of multi-body motion behavior. Finally, there was no experimental validation of the analytical models.

4.2 Testing Program

In this study, a series of rigid-body dynamic tests are conducted using a small-scale shaking table. The specimens are prismatic blocks. The major parameters in the test matrix design are stiffness of restraint spring (K), height/breadth (H/B) ratio of block, coefficient of friction between the specimen and base slab, ground excitations, coefficient of restitution (r) and single-body or stacked dual-body configurations (shown in **Figure 4.1**).

Considering the material of the specimens and the capability of the shake-table, the scale factors (value of model specimen/value of prototype) for the length and modulus of elasticity of the specimens and the acceleration of ground motions are adopted as 1/120, 1 and 1 respectively. Thus, the scale factors for mass, displacement response and acceleration response of the specimens are $(1/120)^3$, 1/120 and 1 respectively using the

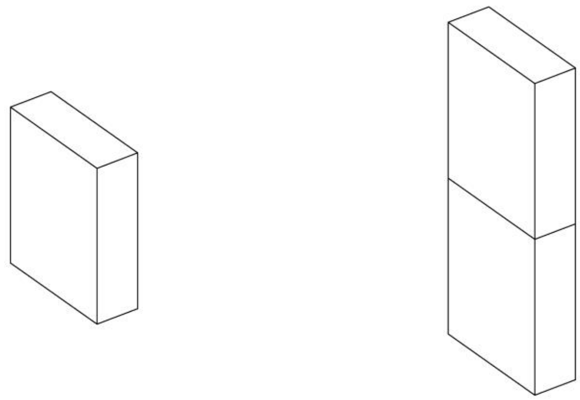

a) b)

Figure 4.1 a) Single-body and b) Dual-body Prismatic Block Systems

similitude law (Caccese and Harris, 1990; Harris and Sabnis, 1999).

The testing program and the components are as follows:

a. Shaking table:

Quanser Shake Table II is employed in this testing. The payload area is 46 cm × 46 cm (18.1 in.× 18.1 in.). The maximum payload at 2.5 g table acceleration is 7.5 kg (16.5 lb.). The maximum travel is ±7.6 cm (3 in.). The maximum velocity and acceleration capacity are 66.5 cm/s (26.2 in./s) and 2.5 g respectively with 7.5 kg (16.5 lb.) payload.

b. Instrumentation:

Instrumentation for the tests is summarized in **Table 4.1**. It is noted that in order to prevent the drag force on the specimens from the attached displacement sensors the video analysis method, by using Tracker 5.0.5 (Brown and Cox, 2009) (**Figure 4.2**), is adopted to obtain the position history of the specimens. Tracker 5.0.5 were validated by measuring the motion of shake table surface and comparing with the string potentiometer measurement. The shake table is heavy. The drag force of string potentiometer on the table can be ignored. Two video recorders were deployed, one in front of the setup and the other one on top. The one on top is to observe any motion that occurred outside the investigated plane of the video recorder in front to capture any three-dimensional motion.

c. Frame for spring restraint

In order to apply a spring restraint to the top of the specimen, a special frame is designed and attached to the shaking-table surface (**Figure 4.3**). Based on the payload of the table

Table 4.1 Instrumentation List

Instrument	Objectives	Quantity
Camera	Observe the setup and specimen failure modes	1
Video recorder	Observe the motion history for video analysis	2
String potentiometer	Monitor the horizontal displacement history of shake-table	2
Accelerometer	Monitor the horizontal acceleration history of specimens and shake-table	2
NI DAQ	Data acquisition and conditioning; data storage	1

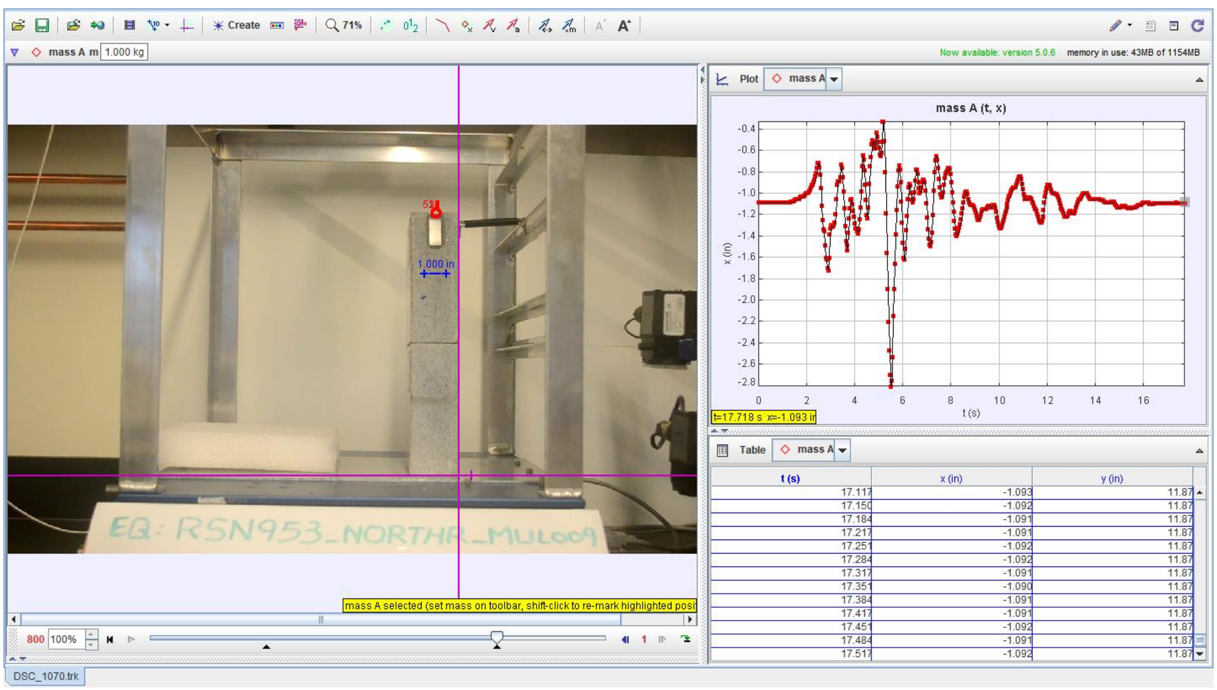

Figure 4.2 Example application of Tracker 5.0.5 in this study

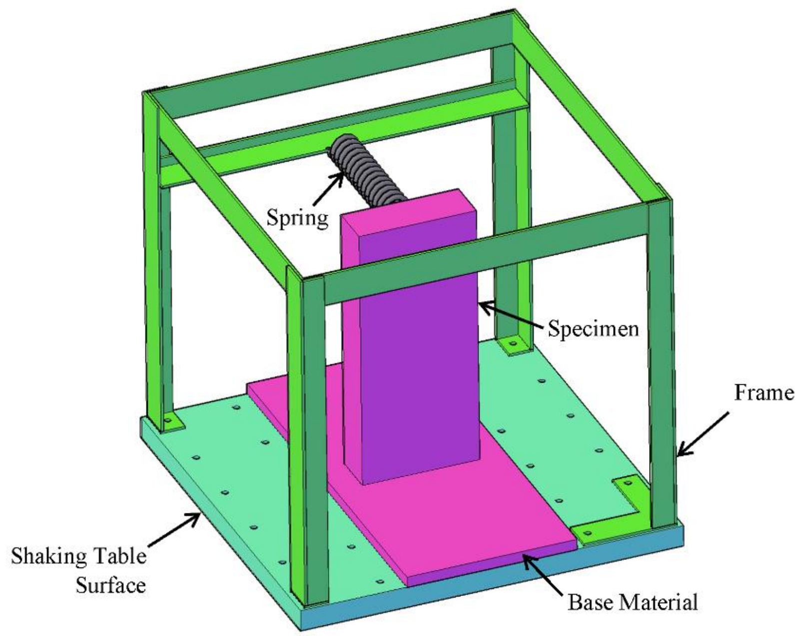

Figure 4.3 Frame for Spring Restraint Attachment and Testing Setup

and the height of specimens, the frame is designed as 425 mm (16.75 in.) height, 445 mm (17.5 in.) width and 451 mm (17.75 in.) depth. It is built with 3.2 mm (1/8 in.) thick aluminum plates. Based on a structural analysis using SAP2000, the maximum lateral deformation in the direction of shaking of this frame under 1.0 g table acceleration generated potential energy equivalent to approximately 0.7% of the kinetic energy of specimen which has ignorable impact on the measurement of the actual displacement of the specimen.

d. Testing specimens

Granite stone is used for the specimens in the small shaking table tests due to its high strength, allowing one block to be used for multiple tests. The geometry characteristics of the stone block specimens are tabulated in **Table 4.2**. The base material was selected as aluminum.

e. Spring stiffness

Using similitude law (Caccese and Harris, 1990; Harris and Sabnis, 1999), the scale ratio of spring stiffness between the model and real structure can be obtained following force equilibrium and scale ratio just obtained before:

Table 4.2 Geometries of Blocks

Specimen number	Dimensions mm (in.) H × B1 × B2	Weight kg (lb)	Slenderness ratio		Note
			H / B1	H / B2	
1	152 × 57 × 152 (6 × 2.25 × 6)	3.4 (7.5)	2.7	1	For dual-body tests
2	152 × 57 × 152 (6 × 2.25 × 6)	3.4 (7.5)	2.7	1	For single-body & dual-body tests
3	203 × 76 × 203 (8 × 3 × 8)	9.0 (19.9)	2.7	1	For single-body tests
4	406 × 51 × 152 (16 × 2 × 6)	8.9 (19.5)	8	2.7	For single-body tests

Force equilibrium: Force provided by spring ($k\Delta$) = Inertial force of the block (ma)

Scale ratio of k = scale ratio of mass × scale ratio of acceleration / scale ratio of displacement = $[(1/120)^3 \times 1] / (1/120) = (1/120)^2$

Based on the analysis in Chapter 3, maximum equivalent stiffness of railroad system is 171 kN/mm. Therefore, the corresponding model spring stiffness is taken as 11.9 N/mm and used for the spring selection.

f. Test matrix

The test matrix is tabulated in **Table 4.3**. It is noted that three types of earthquake records, near fault with a pulse, near fault without a pulse and far field, were considered. The ground motion history records were downloaded from PEER Ground Motion database (Ancheta et al., 2014). Their ground acceleration time histories and FFT power spectra are plotted in **Figure 4.4, Figure 4.5 and Figure 4.6**.

g. coefficient of friction

The coefficient of friction between granite specimen and aluminum base was measurement per ASTM G115 standard (2018). The test set up is illustrated in **Figure 4.7**. A digital force gauge (Mark M7-10) was used to apply a push load to the bottom part of the specimen. The force and displacement time histories were obtained by the force gauge and string potentiometer. And the static and dynamic coefficients of friction were calculated following ASTM G115.

Table 4.3 Test Matrix

<table>
<tr><th>Specimen #</th><th>H/B</th><th>Horizontal restraint</th><th>Ground motion</th></tr>
<tr><td rowspan="2">1</td><td>2.7</td><td rowspan="8">No restraint/
Restraint (k =11.9 N/mm)</td><td rowspan="8">Sine waves (varied of amplitudes (1 cm, 2 cm and 3 cm) and frequencies (0.5 Hz to 4.5 Hz with 0.1 Hz increment toward failure))
Earthquake record in PEER database:
(Far field: NORTHR_MUL009
Near fault with a pulse: IMPVALL_E06140
Near fault without a pulse: GAZLI_GAZ000)</td></tr>
<tr><td>1.0</td></tr>
<tr><td rowspan="2">3</td><td>2.7</td></tr>
<tr><td>1.0</td></tr>
<tr><td rowspan="2">4</td><td>8.0</td></tr>
<tr><td>2.7</td></tr>
<tr><td rowspan="2">1+2 stacked</td><td>5.6</td></tr>
<tr><td>2.0</td></tr>
<tr><td>2</td><td>2.7</td><td>No restraint</td><td>Free rocking (for measurement of coefficient of restitution, discussed in Chapter 5)</td></tr>
</table>

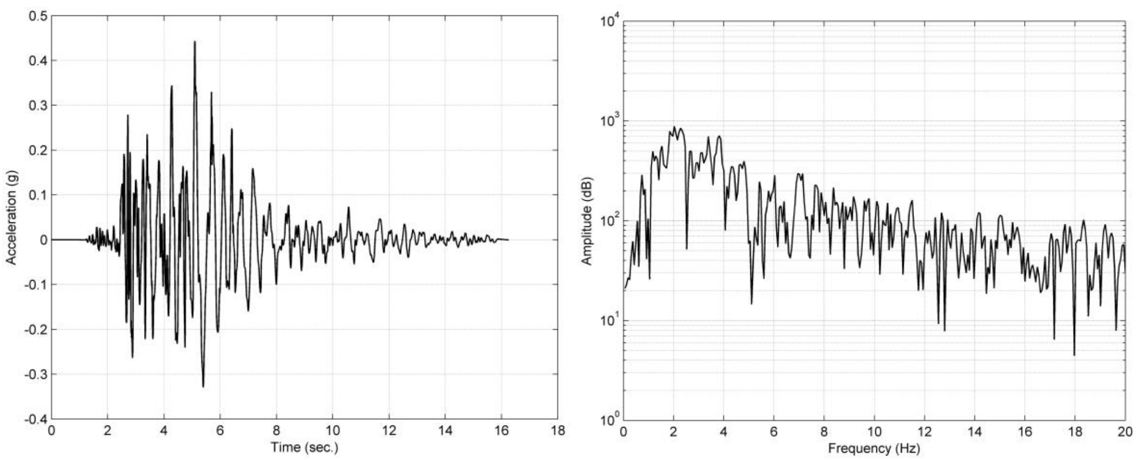

a) b)

Figure 4.4 a) Ground Acceleration Time History and b) FFT Power Spectrum of NORTHR_MUL009 Record

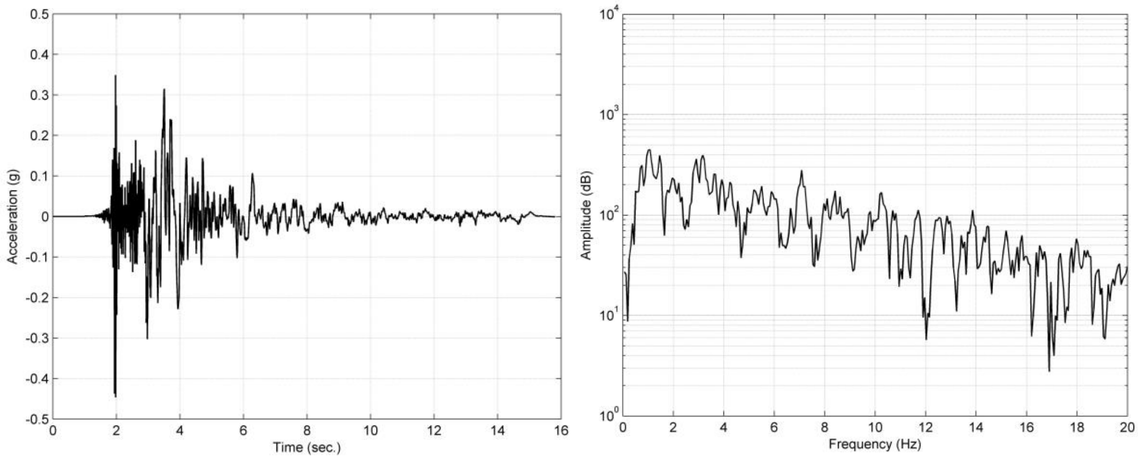

a) b)

Figure 4.5 a) Ground Acceleration Time History and b) FFT Power Spectrum of IMPVALL_E06140 Record

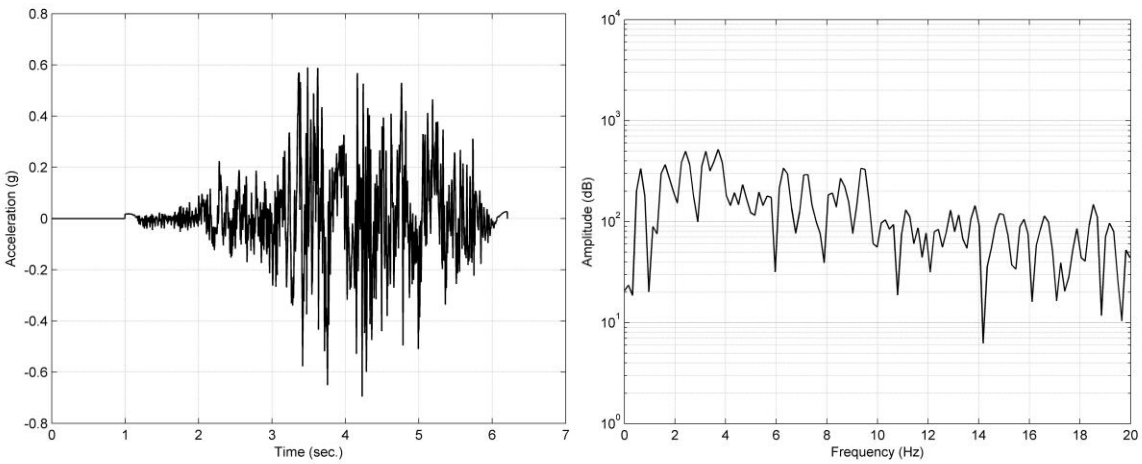

a) b)

Figure 4.6 a) Ground Acceleration Time History and b) FFT Power Spectrum of GAZLI_GAZ000 Record

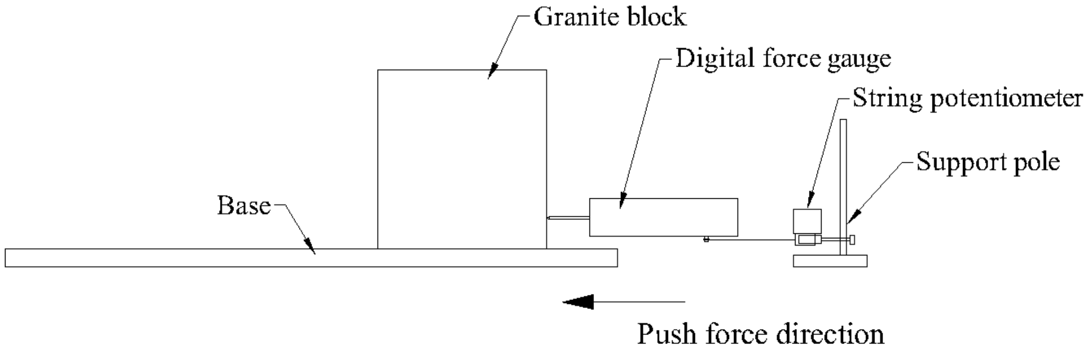

Figure 4.7 Coefficient of Friction Measurement Setup

4.3 Testing Result and Discussion

4.3.1 Coefficient of Friction

The force and displacement data were synchronized to have the same start time. The force-displacement curve data are plotted in **Figure 4.8**. Per ASTM G115, the static coefficient of friction is 0.552, and the dynamic coefficient of friction is 0.505.

4.3.2 Failure mode under Sinusoidal Input

This study investigated the failure modes of single-body specimens without restraint under sinusoidal ground motion inputs. The input set includes sinusoidal waves with various amplitudes and frequencies. The slenderness ratio H/B, weight of the specimens and the characteristics of the shake inputs were considered in the test design. The testing results are tabulated in **Table 4.4**.

The results indicated that the failure mode was directly related to the slenderness ratio H/B and the weight of the specimens, and the maximum acceleration of the ground input. Sliding failure occurred for the specimens with slenderness ratio of 1.0. Rocking overturning failure occurred for the specimens with slenderness ratio larger than 1.0, i.e. 2.7 and 8.0. For the specimens with the same slenderness ratio, slightly larger maximum ground acceleration was needed to trigger the failure of the heavier specimen. For the specimens with the same weight, larger maximum ground acceleration was needed to trigger the failure of the specimen with a smaller slenderness ratio. It was also observed that either amplitude or critical frequency of the ground shake input is not the only factor that triggers the failure. The failure is due to the critical acceleration of ground input that is generated by the combination of amplitude and frequency of the input.

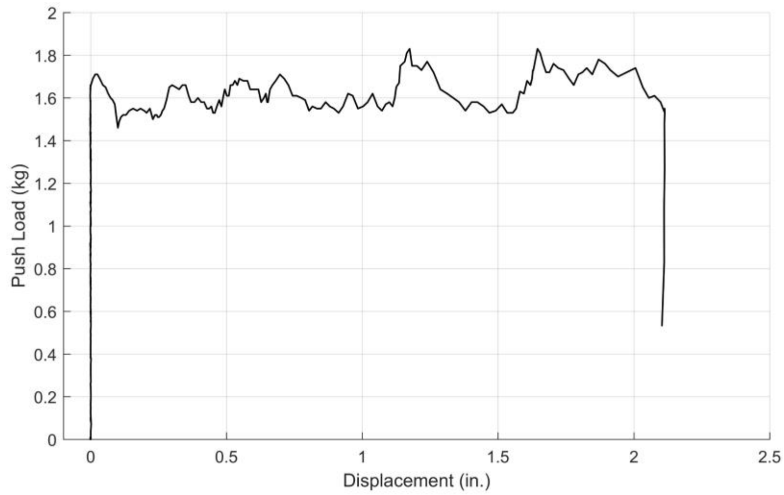

Figure 4.8 Force-displacement Data for Coefficient of Friction Measurement

Table 4.4 Failure Mode Results of Single-body Specimens without Restraint under Sinusoidal Waves

Specimen number (weight in lb)	*H*/*B*	Amplitude (m)	Critical frequency (cycle/sec)	Maximum ground acceleration (g)	Failure mode
2 (7.5)	1.0	0.01	4.5	0.659	sliding
		0.02	3.0	0.686	sliding
		0.03	2.4	0.701	sliding
	2.7	0.01	2.9	0.436	rocking overturning
		0.02	2.1	0.431	rocking overturning
		0.03	1.7	0.438	rocking overturning
3 (19.9)	1.0	0.01	4.4	0.828	sliding
		0.02	3.2	0.880	sliding
		0.03	2.9	0.996	sliding
	2.7	0.01	3.0	0.506	rocking overturning
		0.02	2.1	0.504	rocking overturning
		0.03	1.8	0.626	rocking overturning
4 (19.5)	2.7	0.01	2.6	0.313	rocking overturning
		0.02	2.1	0.393	rocking overturning
		0.03	1.7	0.356	rocking overturning
	8.0	0.01	1.5	0.196	rocking overturning
		0.02	1.1	0.187	rocking overturning
		0.03	0.7	0.112	rocking overturning

4.3.3 Restraining effect

The restraining effect of the spring on the rigid motion can be observed in **Figure 4.9** by using a dual-body system testing as an example. The system was subjected to a far-field earthquake record NORTHR_MUL009. It can be observed that the displacement response at the top of the spring restrained specimen (solid line) is almost identical with the ground motion input which proves the benefit of the restraining effect on the seismic behavior of the rigid body structures. On the other hand, the specimen without the spring restraint (dot-dash line) failed at about 4 seconds by the excessive acceleration.

4.4 Conclusions

A set of shaking table testing was conducted on the single-body and dual-body prismatic block systems. Several parameters were considered in the testing design, such as the slenderness ratio and weight of the specimens, the horizontal restraint condition at the top of the specimens, the various ground motion inputs etc. The conclusions were drawn as following:

1. The failure modes of the single-body specimens without horizontal restraint included sliding and rocking overturning. They were directly related to the slenderness ratio H/B and the weight of the specimen, and the maximum acceleration of the ground input. Specimens with smaller slenderness ratio or larger weight required larger maximum ground acceleration to have the failure occurred.

2. For the rigid-body system, either amplitude or critical frequency of the ground shake input is not the only factor that triggers the failure. The failure is due to the critical acceleration of ground input that is generated by the combination of amplitude and frequency of the input.

3. The benefit of the restraint effect on the dynamic behavior of the prismatic rigid body structures was confirmed in the shake table test.

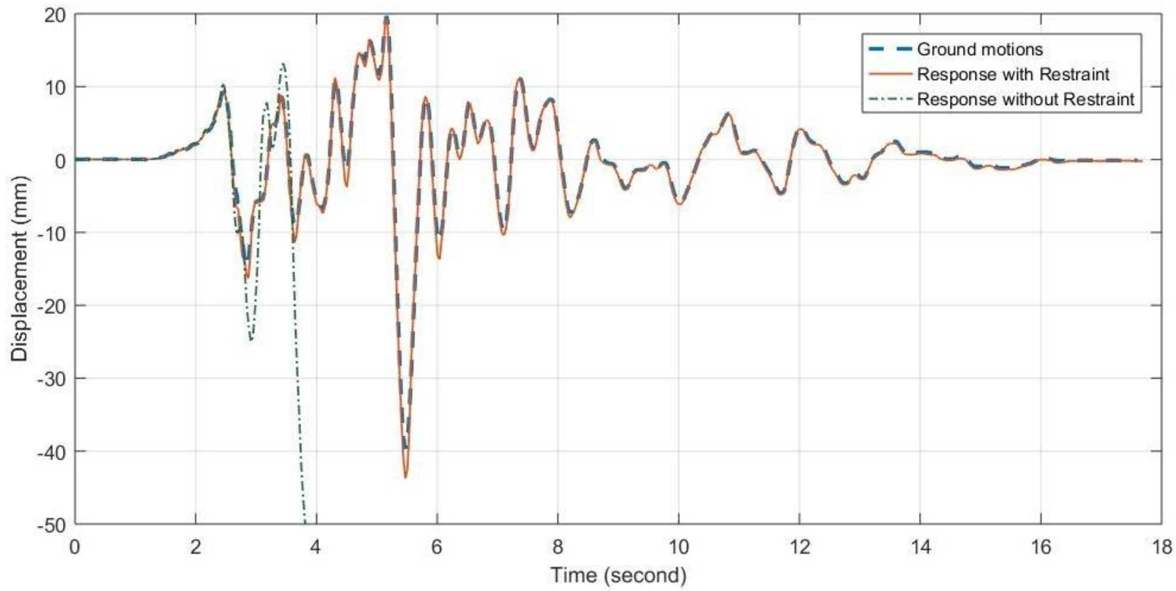

Figure 4.9 Response Time-history Comparison for X-direction Tip Displacement of Dual-body System w/ and w/o Horizontal Restraint under Earthquake NORTHR_MUL009, 1 in.=25.4 mm

Chapter 5:

Unified Expression for Coefficient of Restitution in Rocking Problem

5.1 Introduction

The rotational coefficient of restitution (CoR) is an important factor to evaluate the energy dissipation when a block impacts the base in the rocking problem. Similar to the concept of CoR in linear impacts (Newton 1687), Housner (1963) gave the definition of the rotational coefficient of restitution for the rocking problem as the ratio of the kinetic energy just after the impact and the kinetic energy just before the impact. This can be expressed in **Eq. 5-1**:

$$r = (\frac{1}{2} I_0 \dot{\theta}_2^{\,2}) / (\frac{1}{2} I_0 \dot{\theta}_1^{\,2}) = (\frac{\dot{\theta}_2}{\dot{\theta}_1})^2 \qquad \text{Eq. 5-1}$$

where: r is the coefficient of restitution, I_0 is the mass moment of inertia about the rocking center, and $\dot{\theta}_2$ and $\dot{\theta}_1$ are the angular velocity of the block just after and just before the impact respectively.

By considering the conservation of moment of momentum about the rotation center during the impact, the coefficient of restitution for the prism block was solved for and can be expressed as **Eq. 5-2**. α represents the angle of the line through center of gravity of the prism block and rocking center O with the vertical, as shown in **Figure 5.1**.

$$r = (1 - \frac{3}{2}\sin^2 \alpha)^2 \qquad \text{Eq. 5-2}$$

However, the **Eq. 5-2** has proven to underestimate the CoR obtained from experimental data (Kalliontzis et al. 2017) as illustrated in **Figure 5.2**. This means the r value of this equation overestimates the kinetic energy lost during the impact, potentially resulting in unconservative designs. Several researchers proposed improvements of **Eq. 5-2** to make the calculated CoR closer to the experimental data. For example, Kalliontzis et al. (2017) proposed the actual rocking center is closer to the center line. Chatzis et al. (2017) proposed the resultant of impulse is closer to the center line. Ther and Kollár (2017) proposed the bottom surface is uneven and rocking includes consecutive impacts. Lipscombe and Pellegrino (1993) proposed the rocking block would bounce up after the impact. However, all of them could only explain part of the experimental results and couldn't explain the rocking impact mechanism comprehensively.

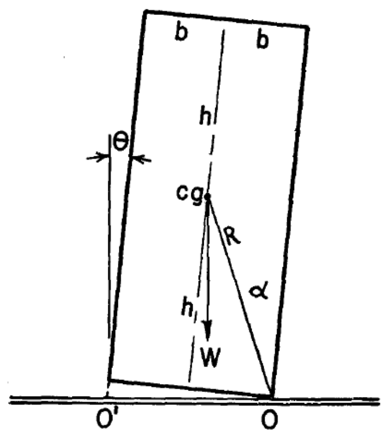

Figure 5.1 Diagram of Housner (1963) Model

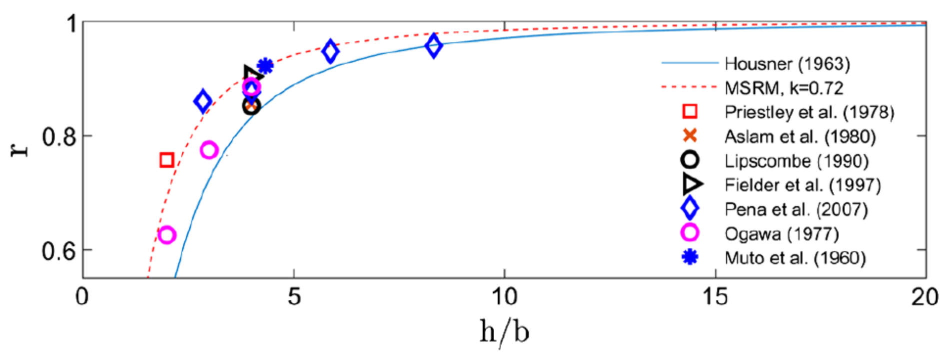

Figure 5.2 Comparison of r estimation by Housner (1963) with reported experimental data (after Kalliontzis et al. 2017)

A unified expression for the rotational CoR in the rocking problem is proposed in this study. It was derived by considering the conservation of momentum in three degree of freedom, i.e. x and y directions and rotation, instead of only considering the rotation direction in the previous research. The expression shows the rotational CoR is related to the slenderness of the prism block, the resultant position of impulse during impact and the linear CoRs in the normal and tangential directions at the impact surface. Housner's CoR expression and other improved CoR expressions are shown to be special cases of the unified CoR expression.

5.2 Improved CoR Expressions in Previous Research

5.2.1 Kalliontzis et al. (2017)

In Housner's CoR model, the contact points of the block and the base during impact was assumed to be at the bottom corners. Kalliontzis et al. (2017) improved this assumption and assumed the contact points, and the rotation centers, are located at some distance from the centerline of the block. The model is illustrated in **Figure 5.3**. That distance is equal to part of the half width of the block, i.e. $\bar{b} = kb$ where $0 \le k \le 1$ and b is the half width of the block. Following the same derivation as Hourner (1963), the improved CoR expression was obtained as **Eq. 5-3**. With the introduction of factor k, the improved CoR estimations are less than the ones estimated by Housner's expression. By using a set of experimental data, Kalliontzis et al. suggested a k value of 0.72.

However, the authors did not explain how the block would rock about a point rather than the corner if the corner is intact. Moreover, the location of the rocking center, i.e. k =0.72 is not convincible to extend to the general cases.

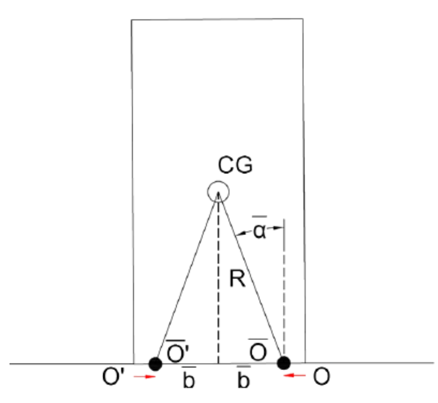

Figure 5.3 Diagram of Kalliontzis et al. (2017) Model

$$r = \left[\frac{4 - 3(\sin^2 \alpha)(1 + k^2)}{4 - 3(\sin^2 \alpha)(1 - k^2)} \right]^2 \qquad \text{Eq. 5-3}$$

5.2.2 Chatzis et al. (2017)

Chatzis et al. (2017) challenged the assumption of the vertical impulse resultant position in Housner's CoR equation. In Houser's equation, it was assumed that the conservation of moment of momentum is about the bottom corners of the block. This assumption means the bottom corners are not only the rocking centers but also the vertical impulse resultant points. Chatzis et al. assumed that the vertical impulse is distributed along the contact surface between the block and the base and the position of the impulse resultant is somewhere between the bottom corners, i.e. λb where $0 \le \lambda \le 1$, and depends on the distribution function of the vertical impulse. The authors didn't recommend the method to determine the location of impulse resultant. The model is illustrated in **Figure 5.4**. The improved CoR expression is given as **Eq. 5-4**.

$$r = \left[\frac{1 - \frac{3}{4}(2 - \lambda)\sin^2 \alpha}{1 - \frac{3}{4}\lambda \sin^2 \alpha} \right]^2 \qquad \text{Eq. 5-4}$$

5.2.3 Ther and Kollár (2017)

Ther and Kollár hypothesized the bottom surface of the block is not perfectly smooth, but has a series of bumps aligned between the bottom corners. In this case, two impacts instead of one in Housner's model occur in one half cycle of a rocking cycle if one bump is in the middle of the bottom surface. Likely, $n+1$ impacts occur in one half cycle rocking if there are n bumps in the middle of the bottom surface. The model is illustrated in **Figure 5.5**. The authors found, by simply applying Housner' equation multiple times on series impacts, that the angular velocity immediately after the impact at the bottom corner is higher than Housner's equation estimation. The kinetic energy loss by this modified model is inversely proportional to the number of bumps.

This hypothesis gave a possible explanation on the underestimation of Housner's CoR equation. However, it still uses the same assumptions of Housner's model, i.e. no sliding and no bouncing up during impact.

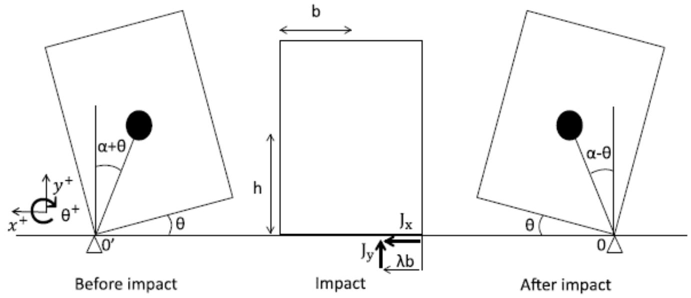

Figure 5.4 Diagram of Chatzis et al. (2017) Model

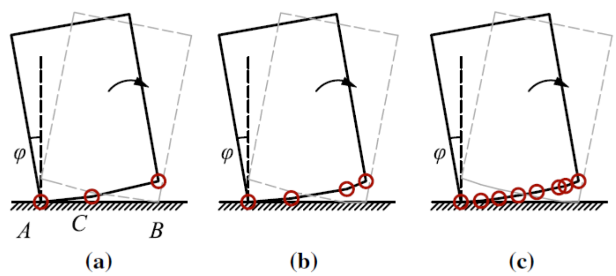

Rocking block. **a** one bump in the middle, **b** two bumps, **c** several bumps

Figure 5.5 Diagram of Ther and Kollár (2017) Model

5.2.4 Lipscombe and Pellegrino (1993)

Lipscombe and Pellegrino discussed the kinetic energy loss of the bouncing mode as the block impacts on the base. The model is illustrated in **Figure 5.6**. Three coordinates, X_G, Y_G and θ, were introduced. The authors proposed the modified expression of CoR as **Eq. 5-5** and introduced the ratio of linear velocities in the Y direction immediately after and before the collision e into the equation. h and b represent the half height and half width of the block respectively. As e is always equal to or larger than zero, the CoR value of this improved equation is equal to or less than the Hourner’s estimation.

However, the authors still assumed the impact occurred only at the bottom corners rather than the bottom surface. Meanwhile the influence of sliding motion in X direction on the CoR was not considered sufficiently.

$$r = \frac{2h^2 - b^2 - 3b^2 e}{2h^2 + 2b^2} \qquad \text{Eq. 5-5}$$

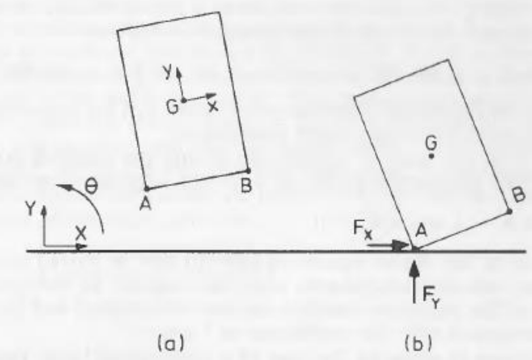

FIG. 9. (*a*) General Configuration of Block during Free Flight in Two-Dimensional Bouncing Model. Three Coordinates (X_G, Y_G, θ) Identify Each Configuration. (*b*) Collision between Corner A and Foundation, Showing (Positive) Impulsive Reactions Applied to Block

Figure 5.6 Diagram of Lipscombe and Pellegrino (1993) Model

5.3 Unified CoR Expression

This section introduces the derivation of a unified CoR expression. The model diagram and the sign convention are shown in **Figure 5.7**. A prismatic rigid block has a mass of m. h and b are the half height and half width of the block respectively. R is the distance from the center of gravity (C.G) to the bottom corners. The moment of inertia about the center of gravity is I_C.

J_X is the impulse resultant in X direction and is located at the contact surface; J_Y is the impulse resultant in Y direction and its location depends on the impulse distribution in the Y direction, it is assumed to have a distance λb from the rocking center, i.e. point O, where $0 \le \lambda \le 1$.

Three coordinates x_C, y_C and θ are used to describe the motion of the block during impact. x_C and y_C represent the linear displacements of the block at the center of gravity in the X and Y directions respectively. Their first order derivatives about time $\dot{x}_C$ and $\dot{y}_C$ represent the linear velocities of the block at the center of gravity in the X and Y directions respectively. θ and $\dot{\theta}$ represent the angular displacement and angular velocity of the block respectively. The subscripts "+" and "-" represent the value immediately after and before the impact respectively.

Applying the conservation of moment of momentum in the X and Y direction as well as about the center of gravity gives three equations:

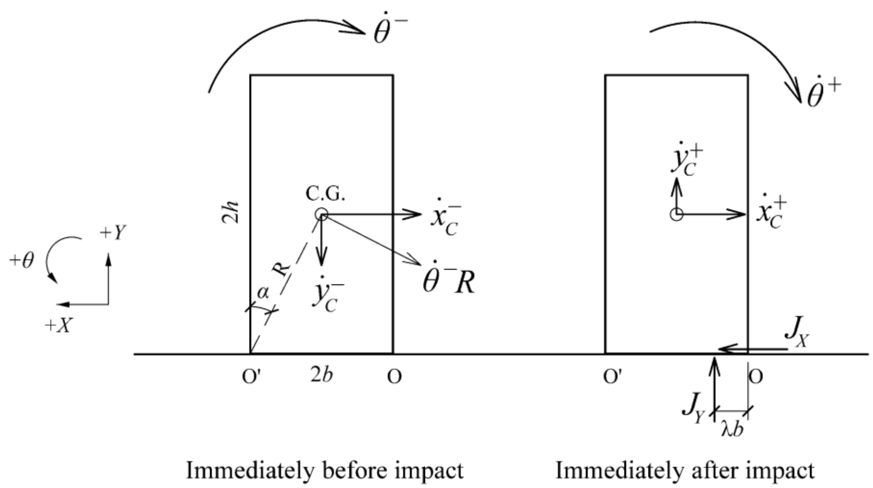

Figure 5.7 Diagram of Proposed Model in this Study

$$m\dot{x}_C{}^{+} - m\dot{x}_C{}^{-} = J_X \qquad \text{Eq. 5-6}$$

$$m\dot{y}_C{}^{+} - m\dot{y}_C{}^{-} = J_Y \qquad \text{Eq. 5-7}$$

$$I_C\dot{\theta}^{+} - I_C\dot{\theta}^{-} = -(b-\lambda b)J_Y + hJ_X \qquad \text{Eq. 5-8}$$

The relationship between the linear velocities in X and Y direction and the angular velocity immediately before the impact can be easily obtained as:

$$\dot{x}_C{}^{-} = -h\dot{\theta}^{-} \qquad \text{Eq. 5-9}$$

$$\dot{y}_C{}^{-} = -b\dot{\theta}^{-} \qquad \text{Eq. 5-10}$$

The linear coefficients of restitution in the X and Y direction are e_X and e_Y respectively. Based on the definition of linear coefficient of restitution by Newton (1687) and **Eqs. 5-9** and **5-10**, we obtain:

$$\dot{x}_C{}^{+} = e_X\dot{x}_C{}^{-} = e_X(-h\dot{\theta}^{-}) \qquad \text{Eq. 5-11}$$

$$\dot{y}_C{}^{+} = e_Y \dot{y}_C{}^{-} = e_Y(-b\dot{\theta}^{-}) \qquad \text{Eq. 5-12}$$

Substituting **Eqs. 5-11 and 5-12** into **Eqs. 5-6 and 5-7** gives:

$$J_X = mh(1-e_X)\dot{\theta}^{-} \qquad \text{Eq. 5-13}$$

$$J_Y = mb(1+e_Y)\dot{\theta}^{-} \qquad \text{Eq. 5-14}$$

Substituting **Eqs. 5-13 and 5-14** into **Eq. 5-8** and following the definition of rotational coefficient of restitution by Housner (1963) yields the proposed unified rotational CoR:

$$\sqrt{r} = e_\theta = \frac{\dot{\theta}^{+}}{\dot{\theta}^{-}} = 1-3\left[\sin^2\alpha(1-\lambda)(1+e_Y)-\cos^2\alpha(1-e_X)\right] \qquad \text{Eq. 5-15}$$

5.4 Discussion on the Unified CoR Expression

5.4.1 Special cases of the Unified CoR Expression

Eq. 5-15 is a function of four parameters α, λ, e_X and e_Y. α is related to the geometric shape of the rigid block and represents the slenderness. Smaller α represents larger slenderness. λ represents the distance between the position of vertical impulse resultant and the nearby bottom corner of the block. $\lambda = 0$ means these two points coincide with each other. $\lambda = 1$ means the vertical impulse resultant is applied at the center of the bottom edge of the block.

e_X and e_Y represent the kinetic energy loss of the block at the center gravity in the X and Y direction respectively. As it is assumed the block rests and rocks on a perfectly horizontal and smooth base, we can consider X and Y directions as horizontal and vertical directions or tangential and normal directions as well. Their graphic relationship with e_θ is illustrated in **Figure 5.8**.

If $e_\theta = e_X = e_Y$, this means the $\dot{x}_C{}^{+}$, $\dot{y}_C{}^{+}$ and $\dot{\theta}^{+}$ decrease with regard to $\dot{x}_C{}^{-}$, $\dot{y}_C{}^{-}$ and $\dot{\theta}^{-}$ in the same ratio. This relationship is illustrated in **Figure 5.9**. Therefore, the direction of $\dot{\theta}^{+}R$ is perpendicular to the line connecting the center of gravity and bottom corner O. This means the block physically rotates bout the point O.

When $\lambda = 0$, **Eq. 5-15** yields:

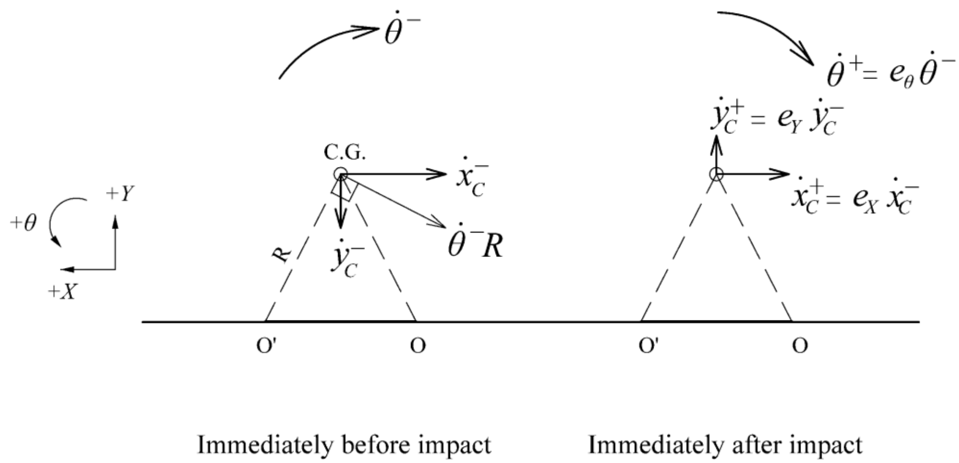

Figure 5.8 Diagram of e_X , e_Y and e_θ

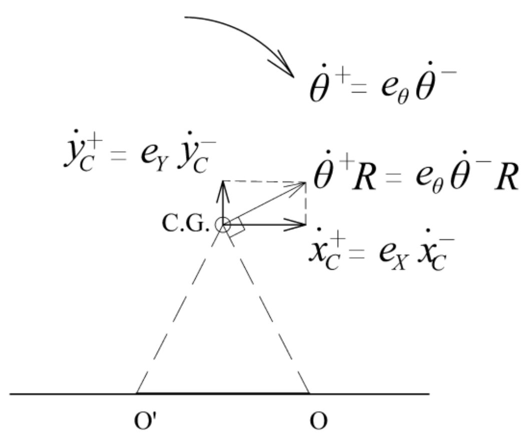

Figure 5.9 Graphic Relationship of $\dot{x}_C{}^+$, $\dot{y}_C{}^+$ when $e_\theta = e_X = e_Y$

$$\sqrt{r} = e_\theta = \frac{\dot{\theta}^+}{\dot{\theta}^-} = 1 - \frac{3}{2}\sin^2\alpha \qquad \text{Eq. 5-16}$$

Eq. 5-16 is the same with **Eq. 5-2**. Thus Housner's CoR expression is a special case of the unified CoR expression when $\lambda = 0$, $e_\theta = e_X = e_Y$.

If $e_\theta = e_X < e_Y$, this means the $\dot{x}_C{}^+$ and $\dot{\theta}^+$ decrease with regard to $\dot{x}_C{}^-$ and $\dot{\theta}^-$ in the same ratio. Meanwhile the $\dot{y}_C{}^+$ yields a value of $e_Y \dot{y}_C{}^-$ which is larger than $e_X \dot{y}_C{}^-$. This means the kinetic energy loss is less in the normal direction than in the tangential direction. The relationship is illustrated in **Figure 5.10**. The resultant of $\dot{x}_C{}^+$ and $\dot{y}_C{}^+$ yields an angle $\beta > 90^\circ$ with the line connecting the center of gravity and the bottom corner O. This case presents the scenario that the block bounces up from the base and rotates in the air about a virtual rotation center above the base.

Substituting $e_\theta = e_X < e_Y$ into **Eq. 5-15** yields:

$$\sqrt{r} = e_\theta = \frac{\dot{\theta}^+}{\dot{\theta}^-} = 1 - \frac{3\sin^2\alpha(1-\lambda)(1+e_Y)}{1+3\cos^2\alpha} \qquad \text{Eq. 5-17}$$

Eq. 5-17 presents the Lipscombe and Pellegrino (1993) as a special case of the unified CoR expression when $e_\theta = e_X < e_Y$.

If $e_\theta = e_X > e_Y$, this means $\dot{x}_C{}^+$ and $\dot{\theta}^+$ decrease with regard to $\dot{x}_C{}^-$ and $\dot{\theta}^-$ in the same ratio. Meanwhile $\dot{y}_C{}^+$ yields a value of $e_Y \dot{y}_C{}^-$ which is smaller than $e_X \dot{y}_C{}^-$. This means the kinetic energy loss is larger in the normal direction than in the tangential direction. The graphic relationship between $\dot{x}_C{}^+$ and $\dot{y}_C{}^+$ is presented in **Figure 5.11**. The resultant of $\dot{x}_C{}^+$ and $\dot{y}_C{}^+$ yields an angle $\beta < 90^\circ$ with the line connecting the

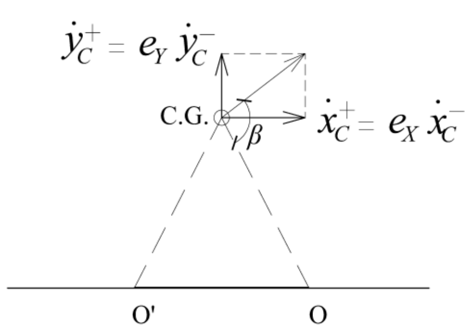

Figure 5.10 Graphic Relationship of $\dot{x}_C{}^+$, $\dot{y}_C{}^+$ when $e_\theta = e_X < e_Y$

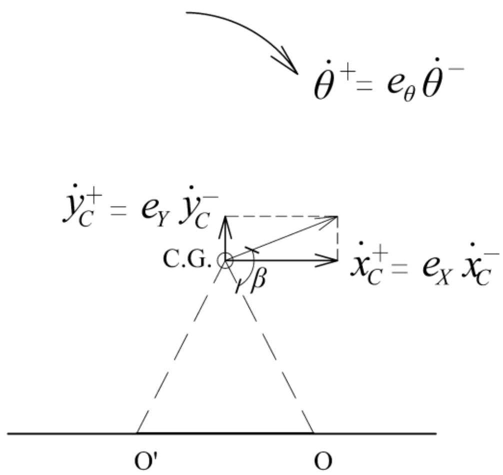

Figure 5.11 Graphic Relationship of $\dot{x}_C^+$, $\dot{y}_C^+$ when $e_\theta = e_X > e_Y$

center of gravity and the bottom corner O. This case presents the scenario that the block rotates about a virtual rotation center which is located some distance from the bottom corner O between the two bottom corners.

Substituting $e_\theta = e_X > e_Y$ into **Eq. 5-15** yields the same **Eq. 5-17** with last case. However, as e_Y is small, the unified CoR expression in this case gives a larger CoR value than the Housner's expression. This covers the proposed hypotheses in Kalliontzis et al. (2017), Chatzis et al. (2017) and Ther and Kollár (2017).

5.4.2 Parametric study on the e_X, e_Y and α

e_X and e_Y represent the coefficient of restitution of the block in the tangential direction and normal direction respectively. In the practice, they are related the impact material and impact velocity (Goldsmith 1960) rather than fit in any special cases just introduced. This section discusses the influences of e_X and e_Y on the unified expression e_θ values.

λ value can be obtained by assuming a triangular distribution of normal impulse on the impact surface (shown in **Figure 5.12**) as the impulse magnitude is positively proportional to the linear velocity of the block. The impulse at the rocking center O was zero, and the impulse reached maximum at the bottom corner O'. Therefore, the vertical impulse resultant located $0.667b$ (b is half breadth) from the bottom corner O'. It notes that the λ can be other value depends on the assumption on the impulse distribution shape.

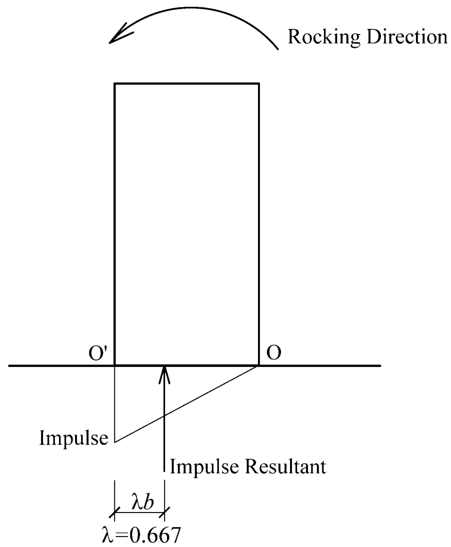

Figure 5.12 Location of Vertical Impulse Resultant

Assuming $\lambda = 0.667$ and the slenderness ratio $h/b = 3$, **Figure 5.13** is obtained using the CoR unified expression with variations of e_Y and e_X. As introduced in the Durda et al. (2011) research, the tangential coefficient of restitution e_X is very close to unity. Therefore e_X value is taken as 1.0, 0.95 and 0.90. The e_Y value is taken between 0.1 and 1.0 with increment of 0.05. The figure indicates that the unified expression value e_θ decreases with the increase of the normal coefficient of restitution e_Y under constant e_X, while e_θ decreases with the increase of the tangential coefficient of restitution e_X under constant e_Y. The spacing between the adjacent lines in the plot is equal as e_X increases from 0.90 to 0.95 then 1.0.

Assuming $\lambda = 0.667$ and the $e_X = 1.0$, **Figure 5.14** is obtained using the CoR unified expression with variations of e_Y and slenderness ratio h/b. h/b value is taken as 3.0, 4.5 and 6.0. e_Y value is taken between 0.1 and 1.0 with increment of 0.05. The plot presents that the unified expression value e_θ increases with the increase of the slenderness ratio h/b under constant e_Y. This indicates that slender piers have less kinetic energy loss during each impact than short piers do. Meanwhile, the spacing between the adjacent lines in the plot decreases as h/b increases from 3.0 to 0.45 then 6.0. e_θ approaches 1.0 as h/b keeps increase.

5.5 Application Example

The unified expression, Housner expression and Kalliontzis expression were compared using the geometric information and free rocking motion history of specimen #2. The

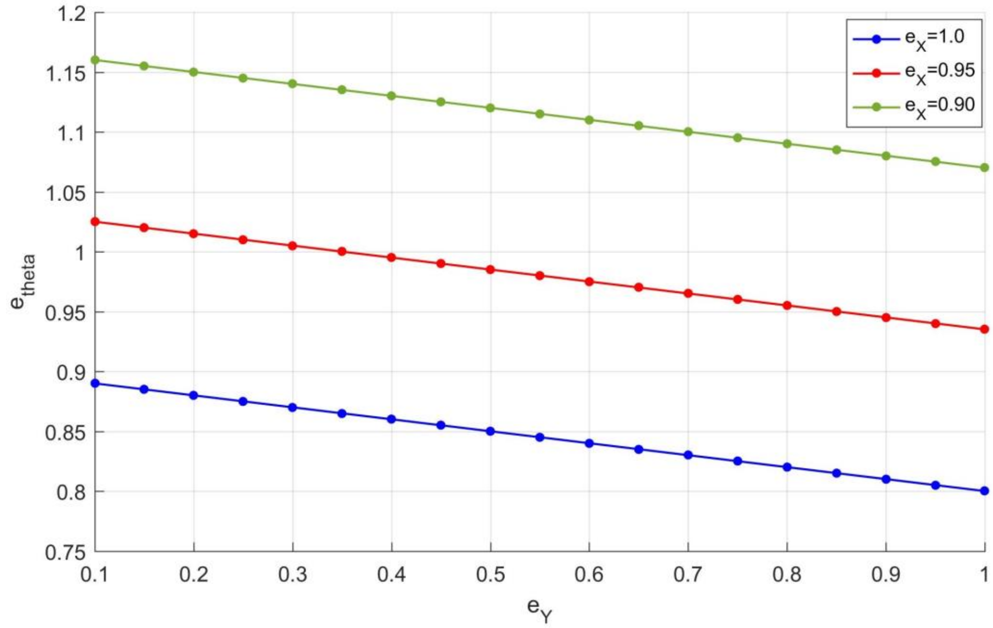

Figure 5.13 Parametric Study on e_X and e_Y

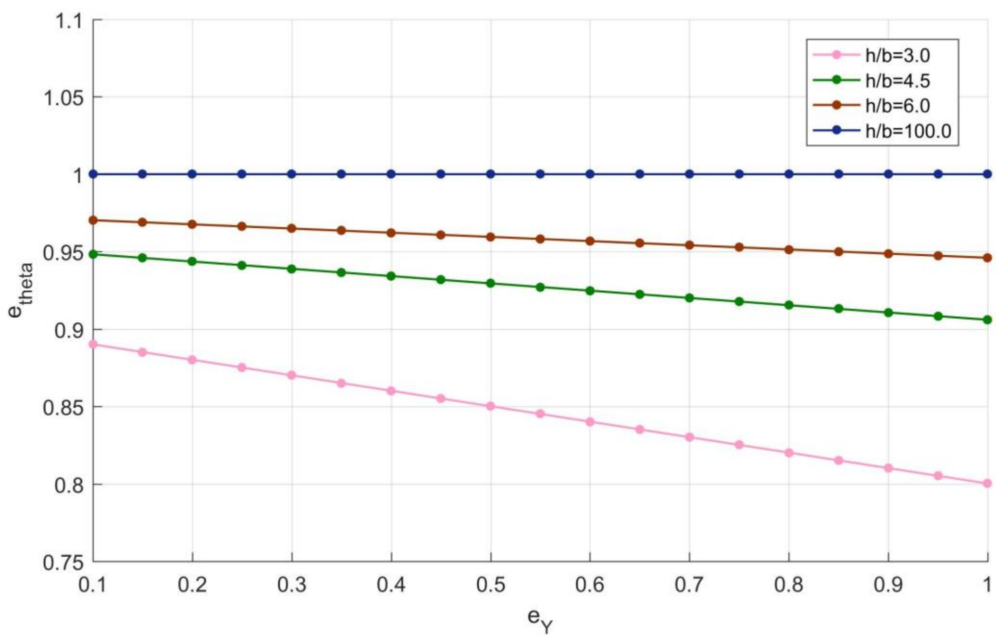

Figure 5.14 Parametric Study on h/b and e_Y

geometry of specimen #2 is shown in **Figure 5.15**.

The geometric information is listed as following: $2h = 6\ in.$ and $2b = 2.25\ in.$ Therefore, $\alpha = 0.359\ rad.$; $(\sin\alpha)^2 = 0.123$ and $(\cos\alpha)^2 = 0.877$. As discussed in Section 5.4.2, the vertical impulse resultant located $0.667b$ from the bottom corner O'.

The linear coefficient of restitution of the block at the center of gravity in the X and Y directions adopted 0.95 (Durda et al. 2011) and 0.80 (Imre et al. 2008, Durda et al. 2011) based on the recommendations for the normal and tangential impact properties between granite and aluminum in the literature.

Substituting the geometric information and other parameters into the unified expression (UE), Housner expression and Kalliontzis expression, they yield the following results:

$$e_{\theta\_Housner} = (1 - \frac{3}{2}\sin^2\alpha) = 0.815$$

$$e_{\theta\_Kalliontzis} = \left[\frac{4 - 3(\sin^2\alpha)(1+k^2)}{4 - 3(\sin^2\alpha)(1-k^2)}\right] = 0.899 \ \ (k = 0.72,\ \text{Kalliontzis et al. 2017})$$

$$e_{\theta\_UE} = 1 - 3\left[\sin^2\alpha(1-\lambda)(1+e_Y) - \cos^2\alpha(1-e_X)\right] = 0.910$$

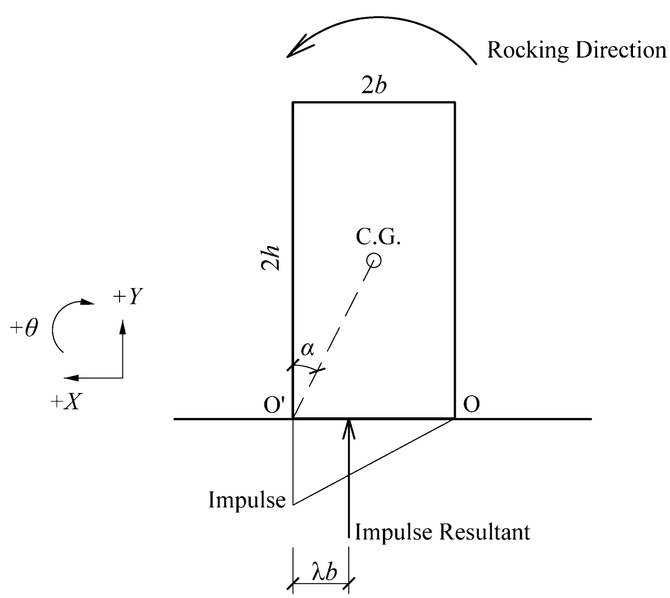

Figure 5.15 Geometric Information of Specimen #2

The results were substituted into governing equation of motion for rocking as shown in **Table 5.1**. A rocking cycle includes two rocking motions (motions 1 and 3) and two impact motions (motion 2 and 4). Then this rocking cycle repeats again and again until the tilting angle of the block approaches zero. The governing equations of motion for rocking motions were obtained using Newton Second Law and moment equilibrium about rocking center. The governing equation of motion for impact motions followed the definition of rotational coefficient of restitution $\dot{\theta}^{+} = e_{\theta}\dot{\theta}^{-}$. The equations of motion were solved using space-state method and realized using ODE 45 solver in MATLAB (Mathwork 2018).

The tilting angle time-history of specimen #2 was simulated using $e_{\theta\_Housner}$, $e_{\theta\_Kalliontzis}$ and e_{θ_UE} as the angular velocity reduction factor. These three time-history results are plotted and compared with the experimental results of this study in **Figure 5.16**. Both the results by Housner expression and Kalliontzis expression attenuate faster than the unified expression result and experimental data. The simulation result using unified expression reaches good agreement with the experimental data.

5.6 Conclusions

A unified rotational CoR expression is developed in this study after a comprehensive review of the models and hypotheses proposed by previous researchers. Three coordinates, x_C, y_C and θ, are used to describe the motion of the block during impact in order to consider the bouncing up scenario. Several conclusions were drawn as following:

1. The rotational CoR is related to four parameters α, λ, e_X and e_Y. They represent the geometric shape of the rigid block, the vertical impulse resultant location and the kinetic energy losses in the normal and tangential directions.

2. The parametric study indicated that the unified expression value e_{θ} decreases with the increase of the normal coefficient of restitution e_Y under constant e_X, while e_{θ} decreases with the increase of the tangential coefficient of restitution e_X under constant e_Y. Meanwhile, it presented that the unified expression value e_{θ} increases with the increase of the slenderness ratio h/b under constant e_Y. This indicates that slender piers have less kinetic energy loss during each impact than short piers do.

3. Specifically under certain conditions, the unified expression covers the models and expressions in Housner’s study and other proposed expressions. The simulation of rocking behavior using unified expression CoR value reached a good agreement with the experimental data.

Table 5.1 Governing Equation and Space-state Equations in a Rocking Cycle

Motion	Force diagram for each section	Governing equation of motion	Space-state equations
1	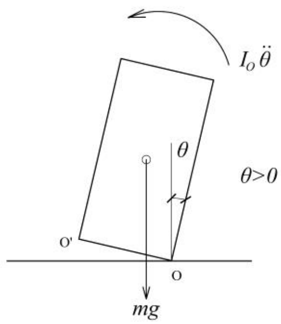	$I_O\ddot{\theta}+mgR\sin(\alpha-\theta)=0$	$\frac{dx_1}{dt}=-mgR\sin(\alpha-x_2)/I_O$ $\frac{dx_2}{dt}=x_1$ $(x_1=\frac{d\theta}{dt}=\dot{\theta},\ x_2=\theta)$ Initial value: $x_1=0,\ x_2=\theta_0$
2	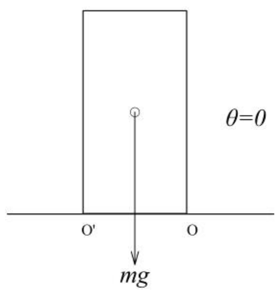	$\dot{\theta}^+=e_\theta\dot{\theta}^-$	$x_1=\dot{\theta}^+,\ x_2=0$
3	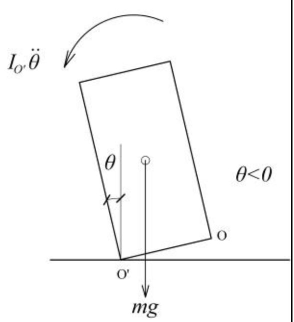	$I_O\ddot{\theta}-mgR\sin(\alpha-\theta)=0$	$\frac{dx_1}{dt}=mgR\sin(\alpha-x_2)/I_O$ $\frac{dx_2}{dt}=x_1$ $(x_1=\frac{d\theta}{dt}=\dot{\theta},\ x_2=\theta)$ Initial value: $x_1=\dot{\theta}^+,\ x_2=0$
4	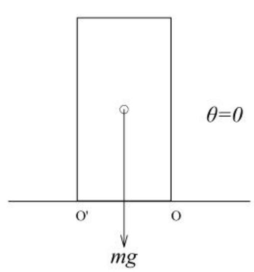	$\dot{\theta}^+=e_\theta\dot{\theta}^-$	$x_1=\dot{\theta}^+,\ x_2=0$

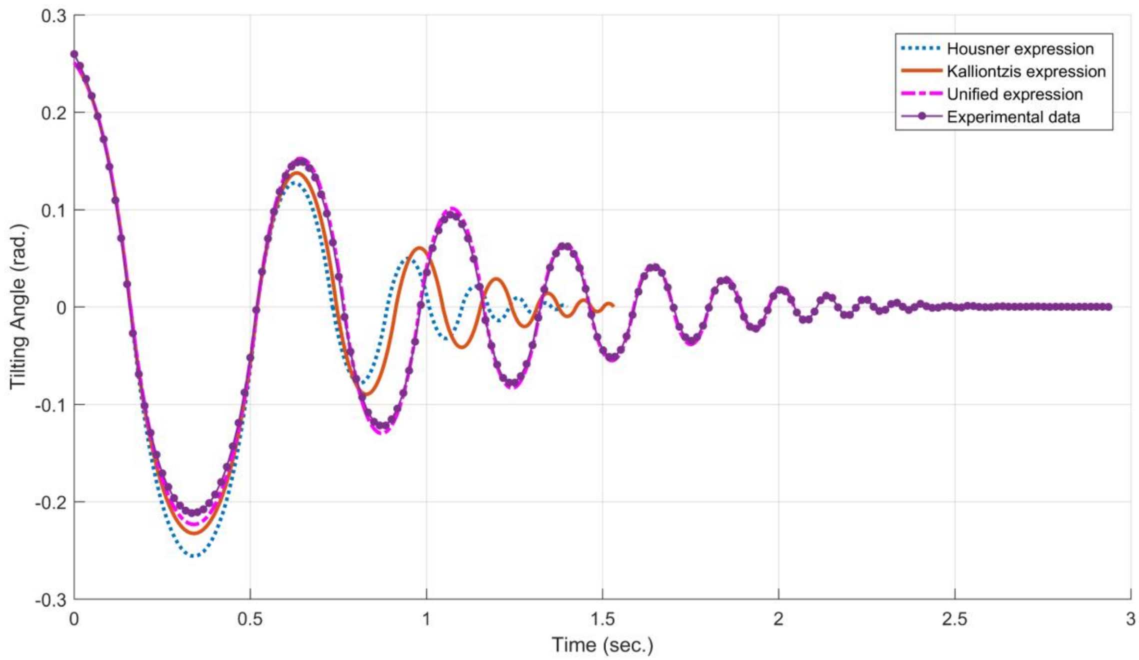

Figure 5.16 Comparison between Results of Different CoR Expressions and Experimental Data

Chapter 6:

Contributions of this Study

The contributions of this study were summarized as following:

1. 4315 seismic performance records of railroad bridges were collected and investigated. Totally five URM pier damage records and nine URC pier damage records were found. This is indicated that the URM and URC railroad bridge piers had superior performance in the past earthquakes.

2. Based on the observation on the URM and URC railroad bridge pier damages in the previous earthquakes, it is found that the behavior of this type of piers is prone to include sliding and rocking which are typical for rigid body motions. Other failure modes include: (1) integral displacement in horizontal or vertical directions or integral tilting; (2) coping stone failure, e.g., loosened, displaced, or torn; (3) anchorage failure between bearings and piers.

3. The track system was considered as a contributor to the superior performance of railroad bridges due to its restraining effect against horizontal movement of the superstructure during earthquakes. A numerical modelling scheme which takes into consideration of the nonlinear properties of the ballast and bearings as well as steel and concrete materials is proposed and validated by previous field full-scale testing. The model was used to obtain equivalent spring stiffness of the rail track system. Other findings included:

(1) For the open-deck girder bridge model, the secant stiffness of the bridge system increases with the increase of the lateral stiffness of substructure. The model with a higher pier stiffness has a smaller ultimate displacement. It is found that the failure of the bridge system is governed by the bearing capacity for a stiffer substructure and by the rail steel failure for a substructure with less lateral stiffness.

(2) For open-deck bridges the rotational stiffness of the substructure has little impact on the secant lateral stiffness of the bridge system. The stress of rail steel remains at a low level. The cause of ultimate state is the excessive bearing deformation.

(3) For ballast bridges, the secant stiffness of the bridge system increases when the lateral stiffness of substructure increases. Due to the existence of ballast between the rail track and bridge girder, the lateral displacement and tensile stress of the rail steel remain small. The bridge system reaches the ultimate state when the bearing reaches the lateral displacement capacity.

(4) For ballast bridge models, as the rotational stiffness of substructure decreases, the secant lateral stiffness of bridge structure system also decreases. Meanwhile the ultimate load and corresponding system lateral displacement at ultimate state increases. The bridge system reaches the ultimate due to the excessive lateral deformation of the bearing.

4. A small-scale shaking table experimental study was conducted, which investigates the dynamic response of prismatic rigid body specimens with a spring restraint on top. Several parameters are considered in the test matrix such as stiffness of restraint spring, height/breadth ratio, ground excitations and single-body or multi-body configuration. It is found that:

(1) The failure modes of the single-body specimens without horizontal restraint included sliding and rocking overturning. They were directly related to the slenderness ratio h/b and the weight of the specimen, and the maximum acceleration of the ground input. Specimens with smaller slenderness ratio or larger weight required larger maximum ground acceleration to have the failure occurred.

(2) For the rigid-body system, either amplitude or critical frequency of the ground shake input was not the only factor that triggers the failure. The failures were due to the critical acceleration of ground input that is generated by the combination of amplitude and frequency of the input.

(3) The benefit of the restraint effect on the dynamic behavior of the prismatic rigid body structures was confirmed in the shake table test.

5. A unified rotational coefficient of restitution expression was developed, which consider three coordinates to describe the motion of the rigid body and possible bouncing up scenario. It was found that the rotational coefficient of restitution is related four parameters: the geometric shape of the block h/b, the position of impulse resultant in normal direction λ and the kinetic energy losses in normal and tangential directions e_Y and e_X. The parametric study indicated that the unified expression value e_θ decreases with the increase of the normal coefficient of restitution e_Y under constant e_X, while e_θ decreases with the increase of the tangential coefficient of restitution e_X under constant e_Y. Meanwhile, it presented that the unified expression value e_θ increases with the increase of the slenderness ratio h/b under constant e_Y. This indicates that slender piers have less kinetic energy loss during each impact than short piers do. Under certain conditions, the unified expression covers the models and expressions in Housner's study and other proposed expressions. The simulation of rocking behavior using unified expression CoR value reached a good agreement with the experimental data.

References

AASHTO (1941). "*Standard Specifications for Highway Bridges.*" AASHTO (American Association of State Highway and Transportation Officials), Washington, DC.

AASHTO (1991). "*AASHTO Guide Specifications for Seismic Isolation Design.*" AASHTO (American Association of State Highway and Transportation Officials), Washington, DC.

AASHTO (2011). "*AASHTO Guide Specifications for LRFD Seismic Bridge Design.*" American Association of State Highway Transportation Officials (AASHTO), Washington, DC.

AASHTO (2017). "*AASHTO LRFD bridge design specifications, customary U.S. units.*" AASHTO (American Association of State Highway and Transportation Officials), Washington, DC.

Abé, M., and Shimamura, M. (2014). "Performance of Railway Bridges during the 2011 Tōhoku Earthquake." *Journal of Performance of Constructed Facilities*, 28(1), 13-23.

ACI. (2014). Building Code Requirements for Structural Concrete and Commentary. *ACI 318-14*, American Concrete Institute, Farmington Hills, MI.

ACI, Saiidi, M. S., Stroh, S., and Pantazopoulou, V. J. (2003). "Seismic analysis and design of concrete bridge systems." *ACI 341.2R-97-R03*, American Concrete Institute, Farmington Hills, MI.

ACI, Valluvan, R., and Sritharan, S. (2007). "Seismic evaluation and retrofit techniques for concrete bridges." *ACI 341.3R-07*, American Concrete Institute (ACI), Farmington Hills, MI.

America's Library (2015). "First U.S. Railway Chartered to Transport Freight and Passengers February 28, 1827 ", <http://www.americaslibrary.gov/jb/nation/jb_nation_train_1.html>.

Ancheta, T. D., Darragh, R. B., Stewart, J. P., Seyhan, E., Silva, W. J., Chiou, B. S.-J., Wooddell, K. E., Graves, R. W., Kottke, A. R., Boore, D. M., Kishida, T., and Donahue, J. L. (2014). "NGA-West2 Database." Earthquake Spectra, 30(3), 989-1005.

AREMA (1907). "*Manual for railway engineering.*" American Railway Engineering Maintenance-of-Way Association, Chicago, IL.

AREMA (2018). "*Manual for railway engineering.*" American Railway Engineering

Maintenance-of-Way Association, Lanham, MD.

ASCE, and FEMA (2000). "Prestandard and commentary for the seismic rehabilitation of buildings." *FEMA 356,* Federal Emergency Management Agency (FEMA), Washington, D.C.

ASTM A499 (2015). Standard Specification for Steel Bars and Shapes, Carbon Rolled from "T" Rails. *ASTM A499,* ASTM International, West Conshohocken, PA.

ASTM G115-10 (2018), Standard Guide for Measuring and Reporting Friction Coefficients. *ASTM G115-10*, ASTM International, West Conshohocken, PA

ATC (1983). "Seismic retrofitting guidelines for highway bridges." *FHWA/RD-83/007*, Applied Technology Council (ATC), Redwood City, Calif.

ATC MCEER Joint Venture, and NCHRP (2003). "Recommended LRFD guidelines for the seismic design of highway bridges." *MCEER/ATC-49*, Applied Technology Council (ATC); Multidisciplinary Center for Earthquake Resistant Engineering Research (MCEER), Redwood City, CA; Buffalo, N.Y.

Baker, I. O. (1909). *A treatise on masonry construction*, J. Wiley & Sons, New York.

Brown, D., and Cox, A.J. (2009). "Innovative uses of video analysis." *Phys. Teacher*, 47, 145–150.

Buckle, I. G., FHWA, and MCEER (2006). "Seismic retrofitting manual for highway structures." *FHWA-HRT-06-032,* Multidisciplinary Center for Earthquake Engineering Research (MCEER), Buffalo, NY.

Byers, W. G. (1996). "Railroad bridge behavior during past earthquakes." *Proc., 14th Structures Congress*, ASCE, UNITED ENGINEERING CENTER, 345 E 47TH ST, NEW YORK, NY 10017-2398, 175-182.

Byers, W. G. (2003). "Earthquake Damage to Railroads." <http://nisee.berkeley.edu/byers/browse.html>.

Byers, W. G. (2004). "Behavior of Railway Bridges and Other Railway Infrastructure in Three Strong to Great Earthquakes in 2001." *Transportation Research Record: Journal of the Transportation Research Board*, 1863(-1), 37-44.

Byers, W. G. (2004). "Railroad Lifeline Damage in Earthquakes." *Proc., 13th World Conference on Earthquake Engineering*. Vancouver, B.C., Canada.

Caccese, V., and Harris, H. G. (1990). "Earthquake Simulation Testing of Small-Scale

Reinforced Concrete Structures." *Structural Journal*, 87(1).

Chatzis, M. N., Espinosa, M. G., and Smyth, A. W. (2017). "Examining the Energy Loss in the Inverted Pendulum Model for Rocking Bodies." *Journal of Engineering Mechanics*, 143(5), 04017013.

Computers & Structures Inc. (2016). *CSI Analysis Reference Manual for SAP2000®, ETABS®, SAFE® and CSiBridge®*, Computer and Structures, Inc., Berkeley, CA.

Cook, S., Kennedy, D., and Cavaco, J. (2006). Seismic Screening Methodology for Railroad Bridges. *Proc.,* AREMA *2006 Annual Conference*. Louisville, KY.

Day, K., and Barkan, C. (2003). "Model for Evaluating Cost-Effectiveness of Retrofitting Railway Bridges for Seismic Resistance." *Transportation Research Record: Journal of the Transportation Research Board*, 1845(1), 203-212.

Derleth, C. (1907). *Design of a railway bridge pier*, Engineering News Pub. Co.

Doe, B. E., Uppal, A. S., Otter, D. E., and Oliva-Maal, D. (2001). "Seismic Resistance Tests on an Open-Deck Steel Bridge." *Technology Digest 01-007,* Association of American Railroads, Transportation Technology Center, Inc., Pueblo, Colorado, pp. 4.

Dong, R. G., Sankar, S., and Dukkipati, R. V. (1994). A Finite Element Model of Railway Track and its Application to the Wheel Flat Problem. *Proceedings of the Institution of Mechanical Engineers, Part F: Journal of Rail and Rapid Transit*, 208(1), pp. 61-72.

Durda, D. D., Movshovitz, N., Richardson, D. C., Asphaug, E., Morgan, A., Rawlings, A. R., and Vest, C. (2011). "Experimental determination of the coefficient of restitution for meter-scale granite spheres." *Icarus*, 211(1), 849-855.

Duryea, E., and ASCE (1907). *The Effects of the San Francisco Earthquake of April 18th, 1906, on Engineering Construction: Reports of a General Committee and of Six Special Committees of the San Francisco Association of Members of the American Society of Civil Engineers*, American Society of Civil Engineers.

Foutch, D. A., and Yun, S. Y. (2001). "Seismic Evaluation of a Steel Truss Railway Bridge." *KEERC-MAE Joint Seminar on Risk Mitigation for Regions of Moderate Seismicity*. University of Illinois at Urbana-Champaign.

Ganesh Babu, K., and Sujatha, C. (2010). Track Modulus Analysis of Railway Track System Using Finite Element Model. *Journal of Vibration and Control*, 16(10), pp.

1559-1574.

Giresini, L., and Sassu, M. (2017). "Horizontally restrained rocking blocks: evaluation of the role of boundary conditions with static and dynamic approaches." *Bulletin of Earthquake Engineering*, 15(1), 385-410.

Goldsmith, W. (1960). *Impact: the* theory *and physical behaviour of colliding solids*, E. Arnold, London.

Green, D. W., Winandy, J. E., and Kretschmann, D. E. (1999). Mechanical properties of wood. *Wood handbook:* wood *as an engineering material (General technical report FPL; GTR-113)*, USDA Forest Service, Forest Products Laboratory, Madison, WI. pp. 4.1-4.45.

Harris, H. G., and Sabnis, G. M. (1999). *Structural Modeling and Experimental Techniques*, CRC-Press.

Housner, G. W. (1963). "The behavior of inverted pendulum structures during earthquakes." *Bulletin of the Seismological Society of America*, 53(2), 403-417.

Imre, B., Räbsamen, S., and Springman, S. M. (2008). "A coefficient of restitution of rock materials." *Computers & Geosciences*, 34(4), 339-350.

International Correspondence Schools (1908). *Bridge piers and abutments*, International Textbook Company, the United States.

Kerr, A. D. (1980). An improved analysis for thermal track buckling. *International Journal of Non-Linear Mechanics*, 15(2), pp. 99-114.

Kalliontzis, D., Sritharan, S., and Schultz, A. (2016). "Improved Coefficient of Restitution Estimation for Free Rocking Members." *Journal of Structural Engineering*, 142(12), 06016002.

Ketchum, M. S. (1921). *Structural engineers' handbook: data for the design and construction of steel bridges and buildings*, McGraw-Hill Book Co., Inc., New York; London.

Lipscombe, P. R., and Pellegrino, S. (1993). "Free Rocking of Prismatic Blocks." *Journal of Engineering Mechanics*, 119(7), 1387-1410.

Mander, J. B., Priestley, M. J. N., and Park, R. (1988). Theoretical Stress-Strain Model for Confined Concrete. *Journal of Structural Engineering*, 114(8), pp. 1804-1826.

Maragakis, E., Douglas, B. M., Haque, S., and Sharma, V. (1996). Full-Scale Resonance

Tests of a Railway Bridge. *Proc., 14th Structures Congress*, American Society of Civil Engineers, New York, NY, pp. 183-190.

Maragakis, E., Douglas, B., Chen, Q., and Sandirasegaram, U. (1998). Full-Scale Tests of a Railway Bridge. *Transportation Research Record: Journal of the Transportation Research Board*, 1624(1), pp. 140-147.

Maragakis, E., Douglas, B., and Chen, Q. (2001). "Full-Scale Field Failure Tests of Railway Bridge." *Journal of Bridge Engineering*, 6(5), 356-362.

MATLAB Version 2018. *The Language of Technical Computing*. The Mathworks, Inc.: Natick, MA, 2018.

McCulloch, D. S., and Bonilla, M. G. (1970). *Effects of the earthquake of March 27, 1964, on the Alaska Railroad*, U.S. Governement Printing Office, Wanshington D.C.

Moreu, F., and LaFave, J. M. (2012). "Current research topics: Railroad bridges and structural engineering." *Newmark Structural Engineering Laboratory*. University of Illinois at Urbana-Champaign.

Newton, I. (1846). *Newton's Principia: the mathematical principles of natural philosophy*, First American edition, carefully revised and corrected / with a life of the author, by N. W. Chittenden. New-York: Daniel Adee, 1846.

Ni, Y. (2005). "The Revision of the Code for the Seismic Design of Railway Engineering and Its Influence on Railway Bridge Piers (in Chinese)." *Railway Standard Design*, 2005(11), 82-84.

NRA China (2009). "Code for Seismic Design of Railway Engineering (in Chinese)." *GB50111-2006 (2009 Edition)*, National Railway Administration (NRA) of the People's Republic of China, Beijing, China.

NRA China (2014). "Code for Design of High-speed Railway (in Chinese)." *TB10621-2014*, National Railway Administration (NRA) of the People's Republic of China, Beijing, China.

Nutt, R. V., Caltrans, and ATC (2000). "Improved seismic design criteria for California bridges: resource document." *ATC 32*, Applied Technology Council (ATC), Redwood City, Calif.

Otter, D. E., Uppal, A. S., and Joy, R. (1999a). "Seismic Resistance Tests on an Open-Deck Steel Bridge." *Technology Digest No. 99-028*, Association of American Railroads, Transportation Technology Center, Inc., Pueblo, Colorado.

Otter, D. E., Uppal, A. S., and Joy, R. (1999b). Measuring Seismic resistance on an open-deck steel bridge. *Railway Track and Structures* (Nov.), pp. 13-16.

Priestley, J. N., Seible, F., and Calvi, G. M. (1996). *Seismic Design and Retrofit of Bridges*, Wiley, New York, NY.

Prucz, Z., and Otter, D. E. (2002). "Railroad Bridge Performance in Past Earthquakes." *Proc., AREMA 2002 Annual Conference*.

Rodrigue, J.-P. (2015). "The Geography of Transport Systems." <https://people.hofstra.edu/geotrans/eng/ch3en/conc3en/usrail18402003.html>.

Sandirasegaram, U. (1997). "Full-scale Field Resonance Tests of a Railway Bridge." Master of Science in Civil Engineering, University of Nevada, Reno.

Sharma, V., Choros, J., Maragakis, E. M., and Byers, W. G. "Seismic Performance of Railway Bridges." *Proc., the Structures Congress XII '94*, 24-28.

Solomon, B. (2008). *North American railroad bridges*, Voyageur Press, St. Paul, MN.

Ther, T., and Kollár, L. P. (2017). "Refinement of Housner's model on rocking blocks." *Bulletin of Earthquake Engineering*, 15(5), 2305-2319.

Tyrrell, H. G. (1911). *History of bridge engineering*, The author, Chicago, IL.

U.S. Govt. Accountability Office (2007). "*Railroad bridges and tunnels federal role in providing safety oversight and freight infrastructure investment could be better targeted: report to congressional requesters.*" U.S. Govt. Accountability Office, Washington, D.C.

Uppal, A. S., Joy, R., and Otter, D. E. (2000). "Seismic Resistance Tests on an Open-Deck Steel Bridge." *Report No. R-939*, Association of American Railroads, Transportation Technology Center, Inc., Pueblo, Colorado, pp. 27.

Uppal, A. S., Otter, D. E., and Doe, B. E. (2001). "Longitudinal Resistance Test on an Open Deck Steel Bridge." *Report No. R-949*, Association of American Railroads, Transportation Technology Center, Inc., Pueblo, Colorado, pp. 45.

Appendix

Summary of Recorded Damages of URM and URC Railroad Bridge Piers in Past Earthquakes

Earthquake			Bridge			Structural Damages Description about Piers	Photos
Date	Identification	Magnitude	Identification	Pier Material	Pier No.		
1891-10-28	Mino-Owari, Japan	8.39	Kisogawa rairoad bridge	brick	No Detail	• Crack at arch in brick pier	
1895-10-31	Charleston, MO	6.60	Illinois Central Railroad Cairo Bridge over the Ohio River	stone	No Detail	• Cracking of joints in a bridge pier • Bands were probably installed as a repair or retrofit after the earthquake	

Earthquake			Bridge			Structural Damages Description about Piers	Photos
Date	**Identification**	**Magnitude**	**Identification**	**Pier Material**	**Pier No.**		
1897-06-12	Assam, India	8.50	Manshai Bridge, Eastern Bengal State Railway.	brick	No Detail	• No detail description	
1906-04-18	San Francisco, CA	8.25	Pajaro River Bridge	plain concrete	General	• The Pajaro River railroad bridge was damaged severely causing by crossing fault line. • Dislocated bridge supported by falsework.	

Earthquake			Bridge			Structural Damages Description about Piers	Photos
Date	**Identification**	**Magnitude**	**Identification**	**Pier Material**	**Pier No.**		
							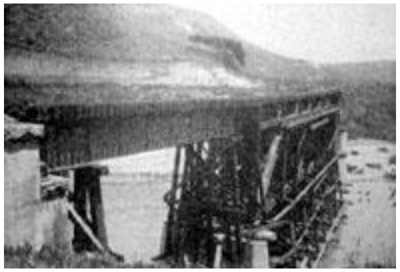
as above	as above	as above	as above	plain concrete	Pier 1 (East abutment)	• Wing-wall crack • Settlement	No Photo
as above	as above	as above	as above	plain concrete	Pier 2	• Coping stone displace	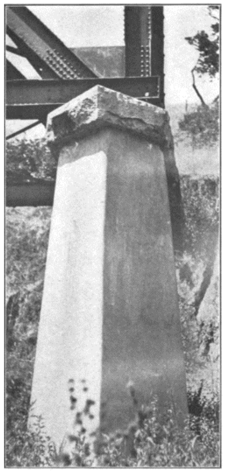

Earthquake			Bridge			Structural Damages Description about Piers	Photos
Date	**Identification**	**Magnitude**	**Identification**	**Pier Material**	**Pier No.**		
as above	as above	as above	as above	plain concrete	Pier 3	• Move horizontally • Settle and raise • Coping stone loosen • 2 horizontal cracks in pier (construction joint or "the line marking the end of day's work ")	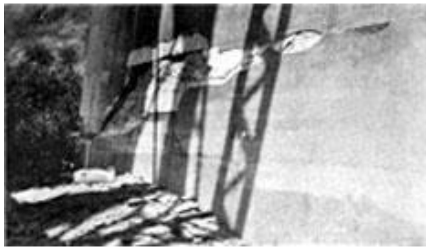
as above	as above	as above	as above	plain concrete	Pier 4	• Move horizontally • Twist slightly • Raise • 1 horizontal crack in pier (construction joint or "the line marking the end of day's work "), and move relatively between upper and lower portion	No Photo

Earthquake			Bridge			Structural Damages Description about Piers	Photos
Date	**Identification**	**Magnitude**	**Identification**	**Pier Material**	**Pier No.**		
as above	as above	as above	as above	plain concrete	Pier 5	• Move horizontally • Settle • Break along a horizontal line close to the ground surface, and move relatively between upper and lower portion • Coping stone (header) tore by the relative movement between substructure and pier	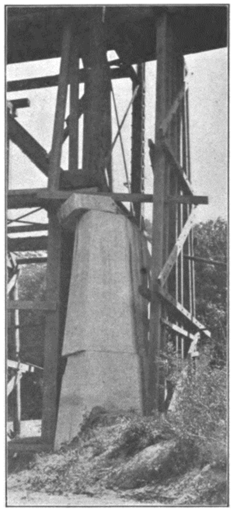
as above	as above	as above	as above	plain concrete	Pier 6 (West abutment)	• Move horizontally	

Earthquake			Bridge			Structural Damages Description about Piers	Photos
Date	**Identification**	**Magnitude**	**Identification**	**Pier Material**	**Pier No.**		
1925-06-29	Santa Barbara, CA	6.83	Dos Pueblos viaduct on Southern Pacific Railroad near Naples, California.	stone	West end	• The piers are shown as repaired after the shock. • The cracks between individual stones were packed with cement mortar and then the entire pier was encased in a 12-inch thick jacket of reinforced concrete.	
as above	as above	as above	as above	stone	No Detail	• Shear-off along a horizontal line, and move relatively between upper and lower portion • The pier was repaired by first driving wooden wedges into the crack, then packing it with cement mortar.	

Earthquake			Bridge			Structural Damages Description about Piers	Photos
Date	**Identification**	**Magnitude**	**Identification**	**Pier Material**	**Pier No.**		
						• The entire pier was encased in a 12-inch jacket of reinforced concrete.	
1948-06-28	Fukui, Japan	7.30	Kuzuryu River Bridge	plain concrete	General	• This was a single track bridge spanning the Kuzuryu River and located about 1500 ft. west of the Nakatsuno highway bridge. It consisted of 10 concrete piers supporting 11 spans, each consisting of 2 parallel plate girders on which the rail structure rested.	

Earthquake			Bridge			Structural Damages Description about Piers	Photos
Date	**Identification**	**Magnitude**	**Identification**	**Pier Material**	**Pier No.**		
as above	as above	as above	as above	plain concrete	Pier 7	• Braced by the felled girders, this pier was still standing in an inclined position. The prime cause of failure was the lack of continuity in the pier construction.	
as above	as above	as above	as above	plain concrete	No Detail	• Sheared-off pier top. The prime cause of failure was the lack of continuity in the pier construction	

Earthquake			Bridge			Structural Damages Description about Piers	Photos
Date	**Identification**	**Magnitude**	**Identification**	**Pier Material**	**Pier No.**		
as above	as above	as above	as above	plain concrete	Pier 2 from the south	• The top of the 2nd pier from the south sheared off cleanly and horizontally, the top portion being displaced to the southwest.	 

<table>
<tr><th colspan="3">Earthquake</th><th colspan="3">Bridge</th><th rowspan="2">Structural Damages Description about Piers</th><th rowspan="2">Photos</th></tr>
<tr><th>Date</th><th>Identification</th><th>Magnitude</th><th>Identification</th><th>Pier Material</th><th>Pier No.</th></tr>
<tr><td>as above</td><td>as above</td><td>as above</td><td>as above</td><td>plain concrete</td><td>N.C.</td><td>• The anchorage of the girders to the piers appeared stronger than in the other bridges that failed, but close inspection showed that the anchor rods were very small.
• The anchor bolts pulled out of the pier as the girders were displaced to the south.
• Failure was due to instability of pier foundations, lack of necessary pier reinforcement, and weak anchorages.</td><td></td></tr>
</table>

Earthquake			Bridge			Structural Damages Description about Piers	Photos
Date	Identification	Magnitude	Identification	Pier Material	Pier No.		
as above	as above	as above	Kanazu Bridge (over the Takeda River)	brick	Center	• The center pier failed by shearing off on a horizontal line.	
1960-05-22	Chile	9.50	Llanquihue railway bridge	concrete	Center	• Tilted • Looking west at center pier, showing bearing separation.	

Earthquake			Bridge			Structural Damages Description about Piers	Photos
Date	**Identification**	**Magnitude**	**Identification**	**Pier Material**	**Pier No.**		
							
1964-03-27	Prince William Sound, Alaska	9.24	Bridge 14.5	concrete	North end of No. 6 span	• Fixed end bearing lifted from pier at north end of 6th span of Bridge 14.5. Anchor bolt pulled free of concrete. In adjacent expansion bearing, nested rollers were driven to the extreme position.	

Earthquake			Bridge			Structural Damages Description about Piers	Photos
Date	**Identification**	**Magnitude**	**Identification**	**Pier Material**	**Pier No.**		
1976-07-28	Tangshan, China	8.00	Ji Channel Bridge	plain concrete	No Detail	• Bridges located on silty clay and silty-sandy clay, such as Ji Channel Bridge, suffered serious damage.	
as above	as above	as above	Dou River Bridge	plain concrete	No Detail	• Bridges located on silty clay and silty-sandy clay, such as the Dou River Bridge, suffered serious damage. • The top of the piers sheared off horizontally, the top portion tilted and braced by superstructure.	

Earthquake			Bridge			Structural Damages Description about Piers	Photos
Date	**Identification**	**Magnitude**	**Identification**	**Pier Material**	**Pier No.**		
1978-06-12	Miyagiken-oki, Japan	7.70	Eaigawa Bridge	plain concrete	No Detail	• Constructed in 1941, the Eaigawa Bridge was a deck girder bridge separated for each line of a double track. • An oval pier supported by a well foundation was cut at the concrete construction joint, and was dislocated as much as 30 cm. in an orthogonal direction, causing a large track deformation.	

Earthquake			Bridge			Structural Damages Description about Piers	Photos
Date	**Identification**	**Magnitude**	**Identification**	**Pier Material**	**Pier No.**		
1989-10-17	Loma Prieta, CA	7.10	Bridge 119.67	concrete pier with stones cap	Pier 3	• Shift between the cap stones and concrete stem; • tipped 6 inches to the west	
1991-04-22	Costa Rica	7.60	Rio Matina Rail Bridge	concrete	N.C.	• The location of the pier with respect to the old connection on the girder shows horizontal displacement of 1.17 meters and settlement of 0.12 m.	

Earthquake			Bridge			Structural Damages Description about Piers	Photos
Date	**Identification**	**Magnitude**	**Identification**	**Pier Material**	**Pier No.**		
2011-3-11	Tohoku, Japan	9.0	unknown bridge on Tohoku-Shinkansen railway line	brick	center	• Cracking along bed joint of masonry piers	

Vita

Qiang Gui was born in Tianjin, China on July 26, 1981. He received his B.S. degree in Environmental Engineering from Tianjin University in July 2003 and M.S. degree in Structural Engineering from Tianjin University in August 2008. He worked as a structural (bridge) engineer and Civil IT engineer for SUN Engineering Consultants International for six years.

Mr. Gui is currently pursuing a PhD degree in Structural Engineering from the University of Tennessee, Knoxville. He is actively applying for a research staff position or a faculty position related to seismic evaluation, concrete structure modelling and additive manufacturing for civil engineering in the university institute.